MICROSTRUCTURAL, CORROSION AND MECHANICAL CHARACTERIZATION OF FRICTION-STIR WELDED JOINTS BETWEEN ALUMINUM AND MAGNESIUM ALLOYS

by

Qingli Ding

Advisor: Brajendra Mishra

A Dissertation

Submitted to the Faculty of the

WORCESTER POLYTECHNIC INSTITUTE

In partial fulfillment of the requirements for the

Degree of Doctor of Philosophy

in

Materials Science and Engineering

April 2023

COMMITTEE APPROVAL

APPROVED by:

Prof. Brajendra Mishra, MTE Program Director, Mechanical & Materials Engineering, WPI

Prof. Adam C. Powell, Mechanical & Materials Engineering, WPI

Prof. Richard Sisson, Mechanical & Materials Engineering, WPI

Prof. Yu Zhong, Mechanical & Materials Engineering, WPI

Dr. Hrishikesh Das, Pacific Northwest National Laboratory

ABSTRACT

Friction Stir Welding (FSW) of Aluminum-Magnesium (Al-Mg) alloys has garnered increasing attention due to its wide-ranging applications in the automotive and aerospace industries. The microstructural, corrosion, and mechanical properties of FSW Al-Mg welds under selected conditions are critical factors that must be well-investigated to ensure their durability and performance.

In this study, electrochemical tests, including Open Circuit Potential (OCP), Linear Polarization Resistance (LPR), Potentiodynamic Polarization Scan (PD), and Electrochemical Impedance Spectroscopy (EIS), have been used to analyze the corrosion resistance of these welds, along with weight loss measurements through cyclic corrosion testing (CCT) and surface evolution via SEM over an 8-week period. Mechanical properties are evaluated through microindentation, nanoindentation, fatigue, and lap-shear tests. The results of the electrochemical tests reveal that the corrosion properties of the center weld zone differ from those of the two base alloys. Indentation tests indicate that the weld zone behaves differently from the base alloys. Surprisingly, the lap shear strength did not decrease significantly even after 8 weeks of cyclic corrosion testing, indicating that the joint prevented any ingress of the electrolyte. Fatigue testing showed that applying an adhesive between the Al and Mg joint improved the fatigue life to some extent, although the corrosion resistance reduced due to the discontinuous bonding of the adhesive layer. Overall, these findings highlight the importance of investigating the corrosion and mechanical properties of FSW Al-Mg welds and provide valuable insights for future modeling works.

Key words: Friction stir lap weld, Corrosion, Light weight alloys, Dissimilar joining, Intermetallic compound, Interfacial bonding strength, Fatigue testing.

ACKNOWLEDGEMENTS

The author would like to acknowledge and thank Prof. Brajendra Mishra, Prof. Adam Powell, Dr. Piyush Upadhyay, Dr. Hrishikesh Das, Tim Skszek from Pacific Northwest National Laboratory (PNNL), Dr. Donovan N Leonard from Oak Ridge National Laboratories (ORNL) and Dr. Kubra Karayagiz for the contributed support throughout this research project. I would not have been able to pursue my Ph.D. without the collaboration from this team.

I would like to express my heartfelt gratitude to my PhD advisor, Prof. Brajendra Mishra, for his unwavering support, guidance, and encouragement throughout my doctoral studies. His mentorship and insights have been invaluable to my academic, personal and career growth, and I feel privileged to have had the opportunity to work with him.

I would also like to thank the members of my committee, Prof. Richard Sisson, Prof. Adam Powell, Prof. Yu Zhong, and Dr. Hrishikesh Das for their valuable guidance and great suggestions on my Ph.D. proposal. I am deeply appreciative of this collaborative opportunity that Prof. Adam Powell has provided. I am thankful for the valuable chance to work with him and participate in this project.

Thanks goes to the MTE department and MPI faculty and staff, Maureen Plunkett and Shelly Wood. I also would like to thank the lab manager Mike Collins, Boquan Li and Joel Harris for all their help in learning to use the machining and characterization equipment. Many thanks go to Dr. Bryer Sausa, Prof. Diana Lados and Prof. Anthony Spangenberger for the helps on nanoindentation testing and fatigue testing. And I must thank members of my research group and my friends from MTE for the great academic atmosphere and precious friendship, both past and present: Akanksha Gupta, Hyunsoo Jin, Himanshu Tanvar, Manish Sinha, Chaitanya Ruhatiya, Jason Porter, Hyunju Lee, Mark Strauss, Aditiya Moudgal, Mahya Shahabi, etc.

Lastly, I want to thank my family members: my parents, Rui Ding and Wenjuan Gao, my brother Yuansen Ding, for always backing me up during my education life. Finally, to my boyfriend, Chenyu Wu, thanks for the constant support while I worked towards this goal.

Table of Contents

List of Figures

List of Tables

Chapter 1: Introduction

Introduction of lightweight materials for Sustainable Transportation

The growing need for lighter structural automotive components is becoming increasingly important as the automotive industry seeks to reduce energy consumption and environmental pollution associated with transportation. Lightweight materials refer to materials that have a low density while maintaining high strength, stiffness, and durability. These materials have become increasingly important in various industries, including aerospace, automotive, and construction, due to their ability to reduce weight, fuel consumption, and emissions, as shown in **Figure 1** where there is the challenge of fuel economy target need with the demand of producing light weight materials all over the world [1]. Lighter components can result in improved fuel economy, as reducing the weight of the vehicle. leads to a reduction in energy consumption [2]. Magnesium (Mg) alloys and Aluminum (Al) alloys are particularly attractive for use in the automotive industry due to their high strength-to-weight ratio. The use of aluminum has been particularly popular in the automotive industry, with aluminum body panels and structural components becoming increasingly common. Mg is the lightest of all structural metals, approximately 75% lighter than steel and 33% lighter than Al alloys, making them an attractive alternative to traditional materials [3]. Magnesium is also increasingly being used in the automotive industry, particularly in the manufacture of cast components such as engine blocks, transmission cases, and suspension components.

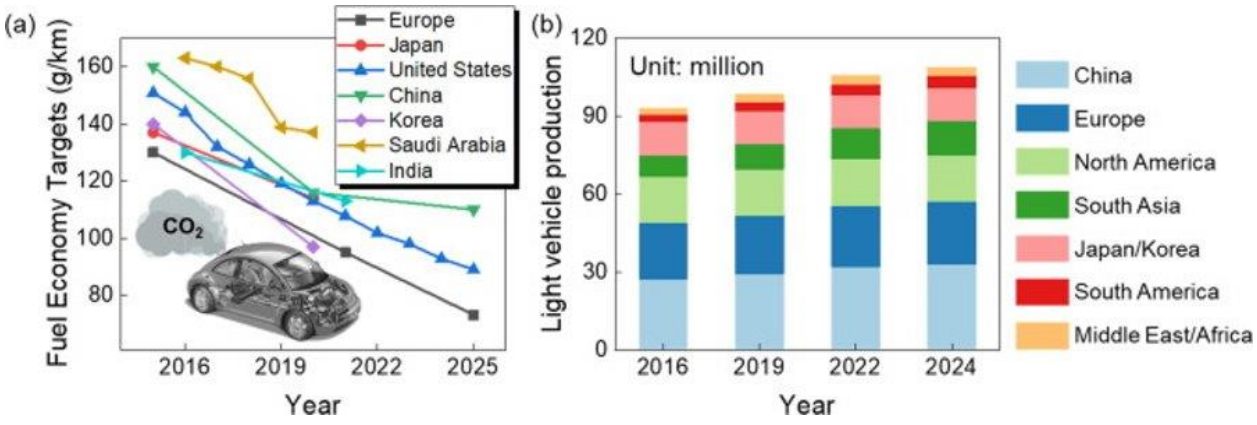

Figure 1 (a) Fuel economy targets; (b) Increased need for light vehicle production.

Additionally, Al alloys are known for their high corrosion and creep resistance, while Mg alloys are noted for their high damping capacity [4]. The use of Al-Mg dissimilar alloy joints in place of traditional steel components can result in significant weight reductions. By reducing the weight of the vehicle, fuel economy can be improved, which can have a positive impact on energy consumption [5]. Therefore, the use of lightweight materials such as Al and Mg alloys in the automotive industry is becoming increasingly important, as it can help reduce the overall weight of vehicles and improve fuel economy. The use of these materials can also contribute to a more sustainable and environmentally friendly transportation system [6].

Introduction of friction stir welding (FSW)

Friction stir welding (FSW) is a solid-state joining process that was invented and patented by Wayne Thomas at The Welding Institute (TWI-Cambridge, UK) in 1991 [7-10]. This process is widely used in various industries, as shown in **Figure 2** [11], including aerospace, automotive, shipbuilding, and railway, for joining materials that are difficult to weld using conventional fusion welding techniques [12]. The basic principle of FSW is simple and straightforward, FSW uses a non-consumable tool, which is rotated and plunged into the workpiece to generate frictional heat due to the interaction of tool shoulder and workpiece that softens the material and causes it to flow plastically. The tool then traverses along the joint, forcing the softened material to mix and bond together. Unlike conventional fusion welding, FSW does not involve melting the material, making it possible to join dissimilar materials with different melting points and physical properties. **Table 1** by **Mishra et al** [12] listed the benefits of FSW process over fusion welding. A tool shoulder with a larger diameter can effectively confine the hot material, preventing it from flowing out and forming flash, which could result in material loss and defective welding.

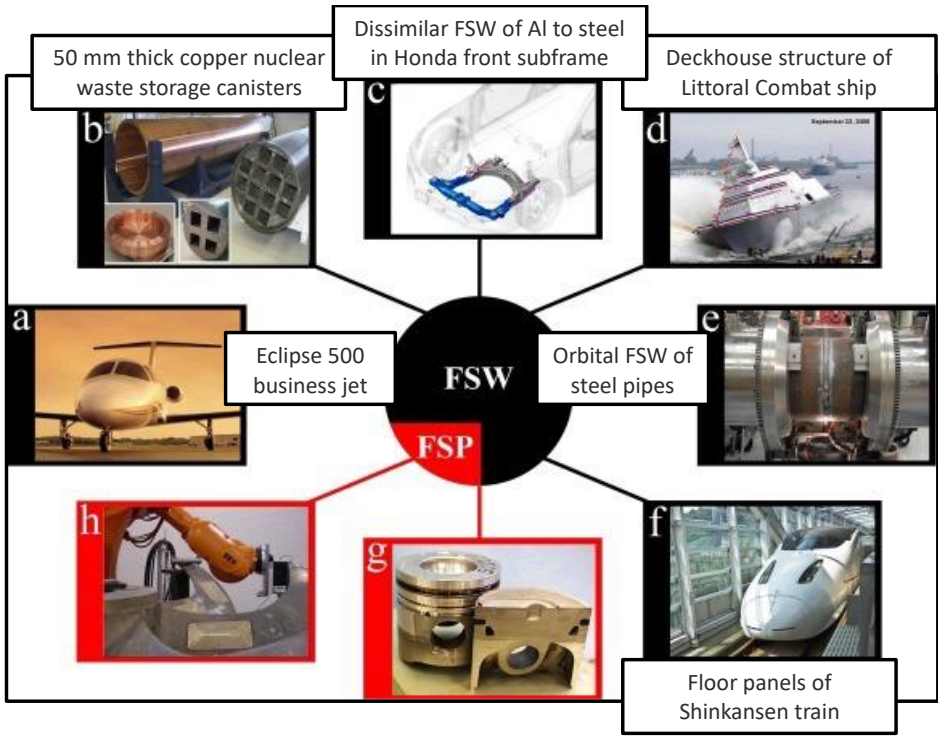

Figure 2 Examples of the industrial application of friction stir welding and processing.

Table 1 Key Benefits of FSW Process Over Conventional Fusion Welding Techniques.

Advantages		**Disadvantages**
Metallurgical	**Process Related**	
No melting	No shielding gas	Huge process forces—special clamping required
No solidification cracking	No filler material	
No gas porosities	No harmful emissions	Exit hole at the end of the weld
No loss of alloying element	No work (arc) hazard	
Low distortion	Low workpiece cleaning	
Weld all aluminum alloys	No post weld milling required	
Excellent repeatability		
Non consumable tool		

There are several approaches that have been successfully adopted such as mechanical joining technique, self-pierce riveting [13], fusion welding process, laser welding [14] and solid-state welding such as friction stir welding (FSW), ultrasonic spot welding, and conventional friction stir

spot welding (FSSW) [15]. Usually, traditional welding joints such as fusion welding between magnesium and aluminum tend to be problematic because of the issues of bonding welds with different high-temperature flow characterizations as well as their heterogeneity [4] which results in distortion, defects, voids and brittle intermetallic compounds at the interfaces between the two alloys [16]. However, with an optimized welding equipment geometry, rotation and speed, good microstructure stability, high tensile strength and ductility, better intermixing can be achieved between the Friction stir welding (FSW) Al-Mg joints [17]. Over the past ten years, dissimilar FSW joints of aluminum-magnesium alloys have been widely reported with a wide range of processing conditions and alloys [18-20].

FSW has successfully been demonstrated in the solid-state joining process as one of the mechanical interlocking methods that applied on the sample boundaries during the welding process [3]. The low heat produced by this process, reduces the probability of residual stress, intermetallic layers, chemical reactions, and distortions between welded materials [19, 21]. These factors make it a preferred welding process, when compared to fusion welding. However, despite solid-state welding process such as FSW or diffusion bonding (DB) can reduce the formation of intermetallic compounds (IMCs) by processing at a lower temperature, it is still impossible to fully avoid the existence of brittle Al-Mg IMCs [22] which play a very important role on both the corrosion reaction and mechanical activities. This study aims to understand the corrosion as well as the mechanical behavior of the FSW joints between 6022Al and ZEK100 Mg that will be applied as a component on the future light weight door hem design from Magna International Inc.

In this project, it is intended to understand the property of this FSW specimen from three dimensions: (1) Microstructural characterization; (2) Corrosion behavior and (3) Mechanical properties. The first set of investigation looks at the corrosion rate of the sample of Al-Mg welds through the following tests: Electrochemical test and component weight-loss at different cathode to anode area ratio; Next set of investigation follows physical properties of the welded alloy: hardness, lap-shear strength, and fatigue values. The overall work is described in the flowchart shows in **Schematic 1**.

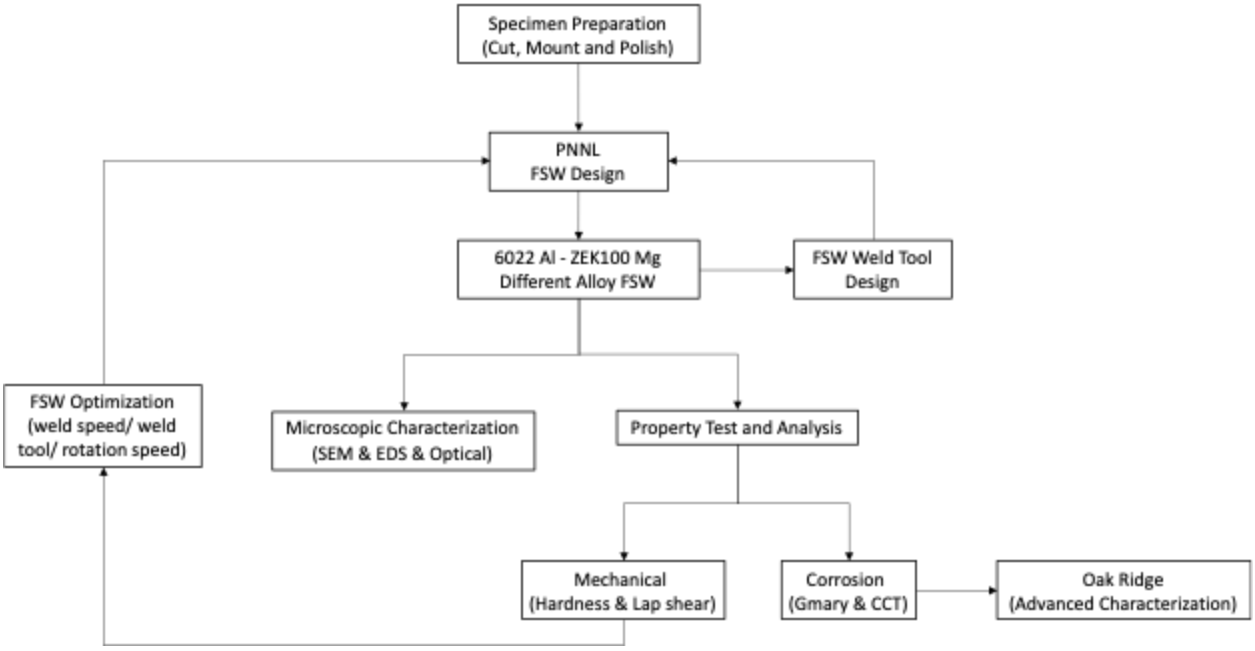

Schematic 1. Flowchart of the project description and the task distribution between WPI, PNNL and ORNL.

Chapter 2: Literature Review

1. Microstructural Review

Dong et al. [23] investigated the microstructure, microhardness and corrosion susceptibility of FSW 6xxx Al-Mg-Si-Cu aluminum alloy, which is considered as having high strength and good corrosion resistance. However, thermomechanical processing could add susceptibility to localized corrosion, such as pitting and intergranular corrosion (IGC), which is a type of micro galvanic between grain boundary precipitates and the surrounding matrix aluminum. It was found that base alloy behaves differently to the joint area on corrosion resistance as well as the hardness mapping. Base material has higher corrosion susceptibility than the weld region. Microstructural analyses are showing that base material mostly has intergranular corrosion because of the continuous cathodic precipitates – Si and Q phase (lath-shaped particles $Al_4Cu_2Mg_8Si_7$ phase) along the grain boundaries (**Figure 3**). The coarsening of intergranular precipitates and Q' phase within grain in heat affected zone (HAZ) could reduce the intergranular corrosion but increase pitting corrosion. The significant decreased intergranular corrosion in thermo-mechanical affected zone (TMAZ) and nugget zone (NZ) is due to the dissolution of precipitates, and the coarsening effect also results in the softening of welded region in **Figure 4**.

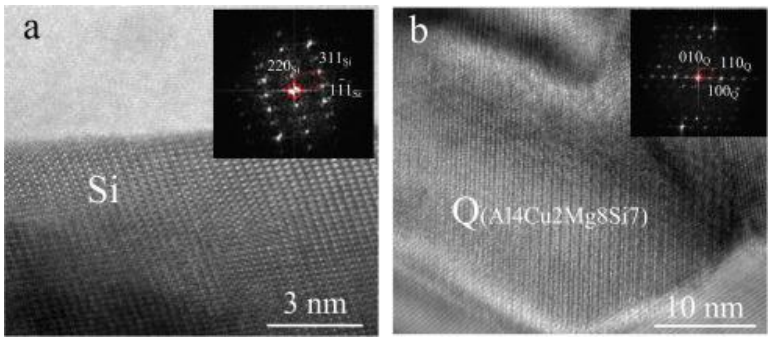

Figure 3 (a) Si and (b) Q phase along the grain boundaries.

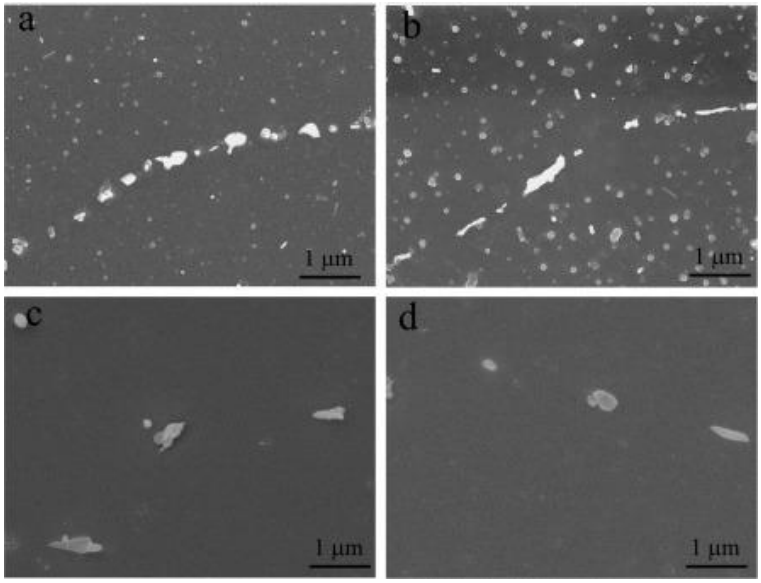

Figure 4 FE-SEM microstructure of the (a) BM, (b) HAZ, (c) NZ and (d) TMAZ.

Similarly, **Nandan et al.** [24] introduced the microstructure and properties of different friction-stir welded alloys. In this paper, the author indicates that for age hardened aluminum alloys, the heat generated from welding process could change the microstructure of the material. The effect was caused by softening and coarsening of the precipitates. There is also some re-precipitation may occur during the cooling process. And the overall result is a minimum hardness value in weld zone and the surrounding heated affected zone, due to dissolution and re-precipitation (**Figure 5**). There are also Al_2Cu precipitation microstructure variations among different regions of FSW AA2219 alloys, as shown in **Figure 6**. TEM pictures are showing that the formation of coarse precipitation among grain boundaries in weld zone **(b)** and heat affected zone **(c)** which is being considered as common detrimental features in the microstructure aspect.

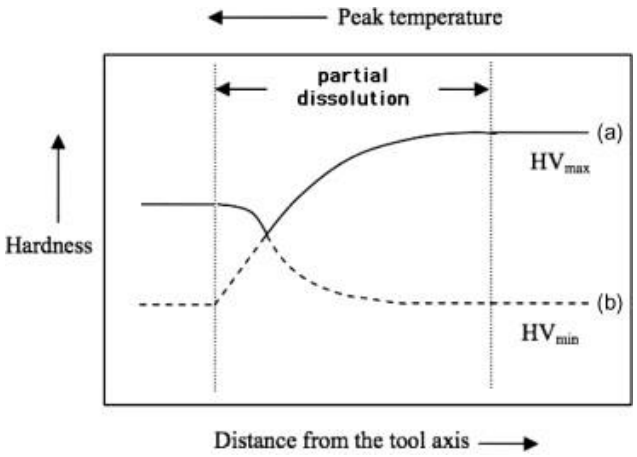

Figure 5 Dissolution (a) and re-precipitation (b) in age-hardenable aluminum alloys [25].

It should be clarified that not all the aluminum alloys are precipitation hardened. For 2xxx cast aluminum alloys, the hardness is more depended on the grain size such as Al-Si casting alloy. For magnesium alloys, the main reason of using FSW technique is to reduce the non-toxic fumes which can help to minimize the solute loss from evaporation or segregation during welding process. Thus, FSW can give a better homogeneous distribution of solutes. It is also reported that FSW can also heal porosities from the casting process to some extent. For the hardness variations, casting Mg alloys appear to be consistent with grain size distribution according to Hall-Petch relationship. Nugget zone and TMAZ tends to have finer grains by recrystallization and can be even finer when the heat is less (or weld speed is higher).

Beygi et al. [26] reviewed the alloying elements effect on the formation of intermetallic during friction stir welding process between Al and steel. And it is reported that the alloying element Si in 6xxx Al could retard the growth of IMCs. Alloying elements Ni and Cr in stainless steel have higher ability to lower the thickness of IMCs because they could retard the diffusion. Other explanation indicated that IMCs can be toughened through solid solution strengthening and the grains of IMCs could be refined to make its thickness lower. It's known that IMC has impact on fracture properties, but the influence is higher on butt welds compared to lap welds.

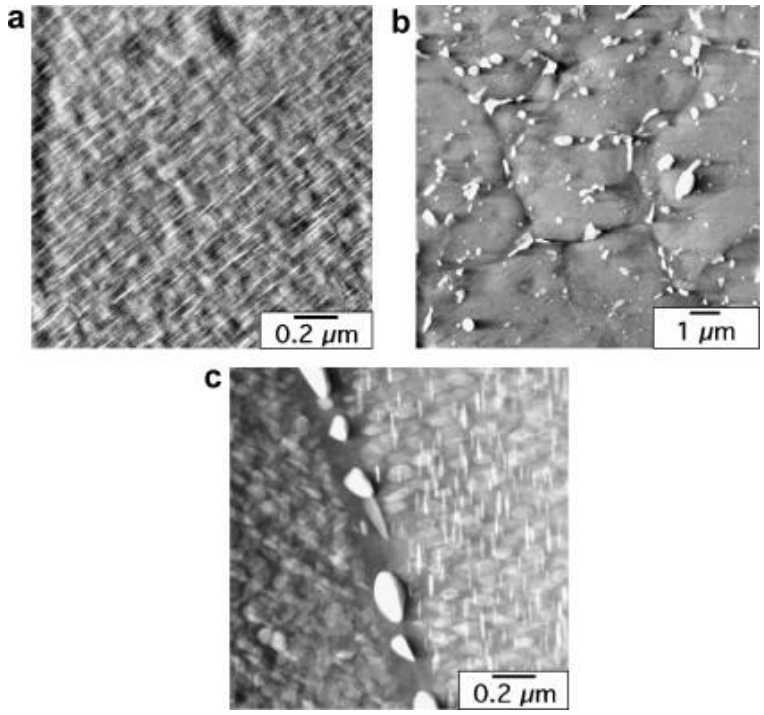

Figure 6 TEM photos show microstructure variations across FSW-AA2219 aluminum alloy. (a)Parent alloy in the precipitation hardened condition; (b) weld zone; (c) heat-affected zone.

2. Corrosion Review

Montemor et al. [27] reviewed the corrosion issues in joining lightweight materials. Aluminum and magnesium alloys are very common type of lightweight structural materials because of their good weight to strength ratio. Because of such advantage, they are widely used in transportation, automotive, aeronautic industry, etc. Therefore, their corrosion property is very crucial to be investigated. Magnesium alloys are usually covered by a protective surface oxide film or hydroxide. However, when O_2 and H_2O exits, its oxide film is not protective enough anymore so that Mg can dissolve and release hydrogen at the same time. Mg also has relatively negative potential, it becomes even more negative in aggressive solution such as when Cl^- exits, there will be local corrosion attack happens if there are local differences in composition and microstructure which could build up some local galvanic corrosion cells. Aluminum and its alloys are considered have higher protective oxide thin film and can keep materials passivated most of the time. However, these films are also fragile when there are aggressive ions exist such as chlorides. When the local

protective film dissolves, it can trigger a pitting attack which related to local pH, alloy composition and aggressive species. There are generally three joining methods: mechanical joining by mechanical force, adhesive bonding by chemical force, welding through physical force under certain temperature and press which can also divided into fusion and non-fusion bonding. Different joining methods can affect the electrochemical activities of the material which will in turn influence its corrosion resistance. Corrosion is usually determined by nature of the joint material, environmental composition, and the mechanical stress such as stress cracking corrosion.

Lin et al. [28] analyzed corrosion properties of FSW 6N01 Al and AZ31B Mg joint on each region of the weld which includes base alloy of 6N01, AZ31B, and stirred zone samples. It was found that after FSW, there are $Al_{12}Mg_{17}$ and Al_3Mg_2 intermetallic phases formed. The precipitants Mg_2Si, Al-Si-Mn-Fe in Al and Al-Mn, Al-Mn-Fe exist in Mg were also found in the weld zone. However, they became much smaller because of the softening effect and plastic deformation during welding process which can crush the precipitates into smaller sizes. Electrochemical tests including potentiodynamic polarization, and EIS at OCP on distinct region indicate the same trend on corrosion rate, which is SZ > BM-AZ31B > BM-6N01. Immersion into salt solution tests revealed that the oxidation film on 6N01 has better protection than oxidation film on AZ31B. And there is evidence of micro-galvanic corrosion from the precipitants. When corrosion processed some time, pH value will arise induced by water reduction at cathodic particles and then the oxidation film on Al alloy will be dissolved and 6N01 Al will start to be corroded.

3. Mechanical Review

Mohammadi et al. [29] reported that by utilizing FSW (Friction Stir Welding) in lap joint welding between magnesium and aluminum, the tensile strength and ductility were enhanced, with the upper part of the stir zone displaying intermixing that increases with tool rotation speed. And when the rotation and travel speeds were increased, the joints showed greater tensile strength and ductility. This was because more intermetallic compounds formed at 1400 mm/min, resulting in the weld material having a higher strength than the softer and more ductile base materials at the interface of magnesium and aluminum. a mechanical interlocking mechanism was found to result in superior tensile properties and higher ductility, as long as the welds were free from any porosity or cracks. Microhardness measurements revealed that the formation of intermetallic compounds could result in higher hardness values. Fractography analysis of the Al and Mg alloy sides indicated the presence of cleavage cracks and protuberances, suggesting evidence of brittle fracture. This indicates that the cracks and failures may have originated from the intermetallic in the Al/Mg reaction layer.

Li et al. [30] has reviewed that the fatigue life of FSW joints can be affected by the welding parameters, test conditions, stress ratio, residual stress, and weld defects. Different process parameters can lead to differences in fatigue crack growth factor. The fatigue performance of FSW joints is mainly affected by the rotation speed and welding speed of the stirring tool. The best fatigue performance for 6061 aluminum alloy was achieved with a tool rotation speed of 1000 rpm and tool travel speed of 80 mm/min and the tool tilt angle between 2～5° can produce a high-quality joint with better fatigue life. The fatigue crack growth rate increased with the stress ratio, as it is clearly shown in **Figure 7**. Many research works [31-33] have reported that the test environment, such as corrosive environment contains NaCl, could also increase the crack factor range. The fatigue life of a material is also influenced by welding residual stress, which affects the stress ratio. As the stress ratio increases, the crack growth rate also increases, but the influence of residual stress decreases. To determine the effect of different residual stress fields on crack growth rate, the residual stress intensity factors can be compared. This is particularly useful when dealing with materials of the same thickness. And it's suggested that residual stress can be reduced or removed by various methods, such as heat treatment aging, shot peening, ultrasonic shock

strengthening, and vibration aging. Welding defect is another key factor affecting the fatigue life. Because the initiation of fatigue cracks is a critical step in the fatigue process and is responsible for approximately 90% of the total life of a component or material. Generally, in high cycle stress life analysis, testing is needed for different materials at various stress amplitudes and mean stress combinations. In low cycle fatigue analysis, where plasticity is dominant, significant work such as assessing dissimilar material joints will be needed in the future.

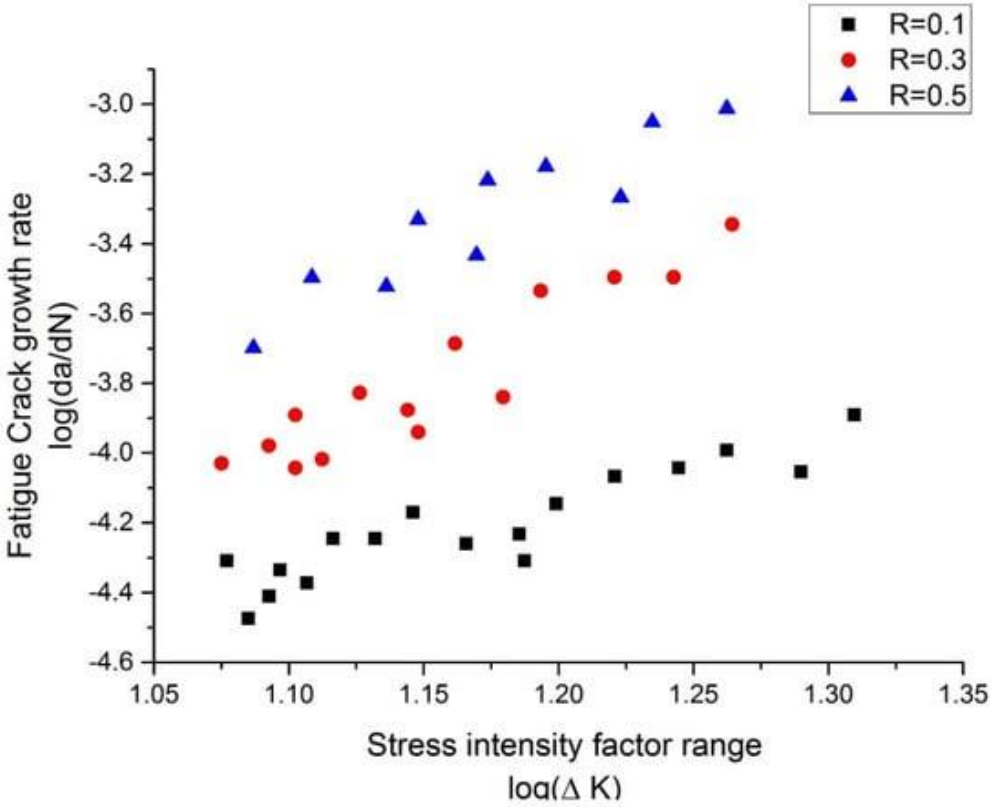

Figure 7 Effect of different stress ratios on crack growth rate.

Chapter 3: Methodology and Result Discussion

1. Material Information and Composition

6xxx Al belongs to the wrought aluminum alloys which contains magnesium (Mg) and silicon (Si) as the major alloying elements. Precipitation hardening by phase Mg_2Si is happening during aging. Al-Mg-Si alloys can be heat treated, solution treatment followed by aging could dramatically improve the yield strength, but the ductility can be decreased because of the Si segregation occurred at the grain boundary. Adding Cr and Mn could help to refine the grain size by depressing the recrystallization. The mechanical properties of 6022 Al could be found in Table 2 (Source: EduPack database).

Table 2 Mechanical properties of 6022 Al

Young's modulus	9.76 - 10.3	10^6 psi
Specific stiffness	25 – 26.3	MN.m/kg
Yield strength (elastic limit)	19.6 – 21.6	Ksi
Tensile strength	33.1 – 36.5	Ksi
Specific strength	50.1 – 55.5	kN.m/kg
Elongation	24.7 – 28.7	% Strain
Tangent modulus	91.1	Ksi
Compressive strength	19.6 – 21.6	Ksi
Flexural modulus	9.76 – 10.3	10^6 psi
Flexural strength (modulus of rupture)	19.6 – 21.6	Ksi
Shear modulus	3.9 – 4.1	10^6 psi
Bulk modulus	9.57 – 10.1	10^6 psi
Poisson's ratio	0.32 – 0.34	
Hardness - Vikers	63 - 66	HV
Elastic stored energy (springs)	1.6 – 1.95	Ft.lb/in^3
Fatigue strength at 10^7 cycles	16.5 – 19.9	Ksi
Fatigue strength model (stress amplitude) (stress ratio = -1)	15.9 – 20.7	Ksi

ZK Mg is a kind of Wrought Magnesium-Zinc-Zirconium-Alloys which is heat treatable and has high strength, that is commonly used in aerospace and automotive applications. Wrought magnesium alloys are manufactured in forms of rolled sheets and plates, rods and tubes, extruded bars, and forged shapes. Added Zn is for increasing the strength and Zr for refining the grain the size. Table 3 lists the mechanical properties of ZEK100 Mg [34].

Table 3 Tensile properties of ZEK100 Mg (strain rate of 10^{-2} s^{-1} at room temperature)

	σ_{YS} (MPa)	σ_{UTS} (MPa)	Elongation (%)	n	σ_{UTS}/σ_{YS}
ZEK100 Mg	225	300	13.3	0.18	1.33

The automotive 6022 Al alloy and ZEK100 Mg alloy sheets used in this study were provided by Magna International Inc, USA. The chemical compositions of samples were determined by Spark ICP-OES are shown in **Table 4.** The lap joint friction stir welded Mg-Al joints were fabricated and offered in the as-welded condition from Pacific Northwest National Laboratory. A single scrolled shoulder with a tri-flute pin **(Figure 8a)** was selected to prepare a series of lap joints. **Figure 8(b)** shows the overall appearance of Al-Mg lap-shear joins with 1.27 mm thick 6022 Al sheet on top and 1.2 mm thick ZEK100 Mg sheet at bottom. The linear welding process was carried under a constant power input of 2.3 kW, 0.9 m/min welding speed and 3.5 kN axial force. This tri-flute pin with scrolled shoulder produces higher surface roughness, fewer defects, smaller hook feature, and greater joint strength than other shapes of the welding tool which has been reported in PNNL [16].

Table 4 Chemical composition of AA 6022 Al and ZEK100 Mg (wt.%) by XRF

Element	Al	Mg	Si	Zn	Zr	Cr	Mn	Fe	Cu
6022 Al	98.35	0.61	0.79	/	/	0.03	0.06	0.11	0.04
ZEK Mg	0.06	98.06	0.004	1.44	0.36	/	0.04	0.01	0.02

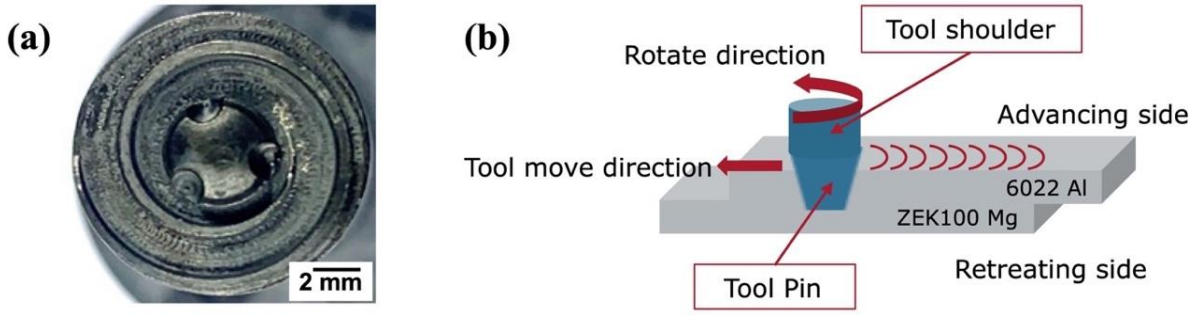

Figure 8 (a) Image of the tri-flute pin with scrolled shoulder; (b) Schematic of friction stir lap welding (FSLW) Al-Mg joint.

2. Microstructural Characterization

It is known that different welding parameters in FSLW process will provide significant effect on the phases type and distributions [35]. In this project, under the optimized weld process which was selected by PNNL, the following unique phases/IMCs from FSLW will be characterized and tested to understand their corrosion behavior. Simplimet 4000 compression mounting system from Buehler, Inc was used to mount FSW Al-Mg joints. The mounted FSW samples have been polished to remove the mechanical scratches and subsequently cleaned with ethanol in an ultrasonic bath. A Tegramin-20 grinder-polisher from Struers Inc. was used to polish the specimen and achieve a mirror finish with a 0.05 µm colloidal silica suspension as the last polishing step. Before metallographic analysis, 6022 Al was etched by keller's reagent: 25 mL methanol, 25 mL HCl, 25 mL HNO_3 and 1 drop HF. Whereas, ZEK100 Mg was etched with 10 mL acidic acid, 10 mL DI water and 4.2 g picric acid in 100 mL ethanol. The scanning electron microscope (SEM) images as well as the energy dispersive spectroscopy (EDS) were obtained from the JEOL JSM-7000F SEM. Optical micrographs (OM) were obtained with a Nikon Epiphot 200 Binocular INVERTED Microscope.

2.1 Grain size and distribution

For the etched Al-Mg samples, when it was observed from diverse views, it can be easily found out that the grain structure, grain size and the phase distribution are very different at various location. **Figure 9** shows the Optical Microscopic (OM) pictures of etched 6022 Al from top view, where **Figure 9(a)** is the advancing side has the same direction between welding direction and tool rotation direction; and **Figure 9(b)** is the retreating side which has the opposite direction which creates more voids and bonding gaps than the advancing side. Therefore, it will be interesting to investigate the corrosion behavior of the advancing and retreating side in the future.

Another interesting finding from the cross-sectional view on the friction-stir welded 6022 Al is the grain structure distribution (**Figure 10)**. It can be obviously observed that weld zone (WZ) has the finest grain size and most recrystallization process resulted from the high strain and thermal energies, surrounding thermal mechanical heat affected zone (TMAZ) has highly elongated grain structure, heat affected zone (HAZ) refers to the region where the grains have no plastic deformation and the size of grain will depend on the amount of thermal energy from the welding process [36]. **Figure 11** and **Figure 12** provide detailed optical microscopy images of the grain structure of etched 6022 Al, captured from a cross-sectional perspective at different zones respectively. For ZEK100 Mg, it also behaves similar grain distribution **(Figure 13)** that center weld region has finest grain and surrounding base metal has larger and coarse grains. Therefore, it will be interesting to investigate if these different grain structure will have different corrosion resistance.

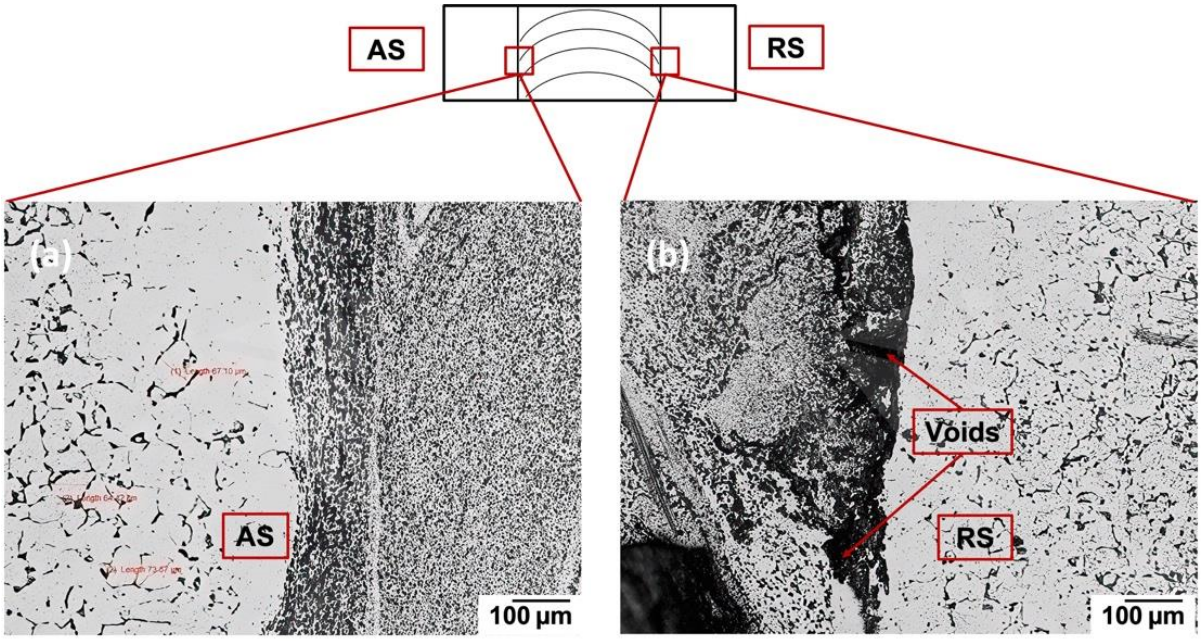

Figure 9 Optical Microscopic pictures of etched 6022 Al from the top perspective. (a) Advancing side and (b) Retreating side.

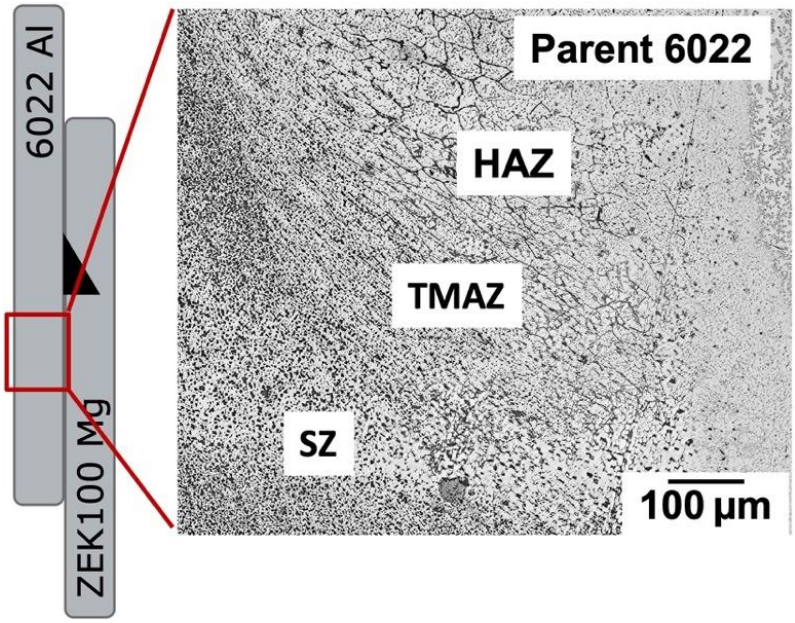

Figure 10 Confocal Microscopic pictures of etched 6022 Al from cross-sectional perspective. Under magnification at (a) ×10 and (b) ×20.

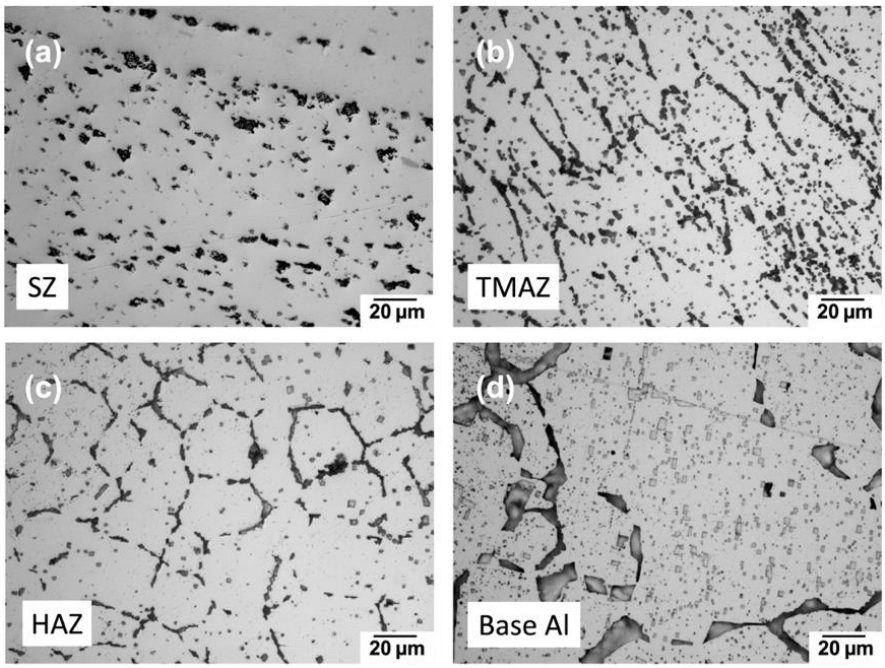

Figure 11 Optical microscopic pictures of a grain structure on etched 6022 Al from a cross-sectional perspective: (a) Stirred zone; (b) thermomechanical affected zone; (c) heat-affected zone; (d) base 6022 Al.

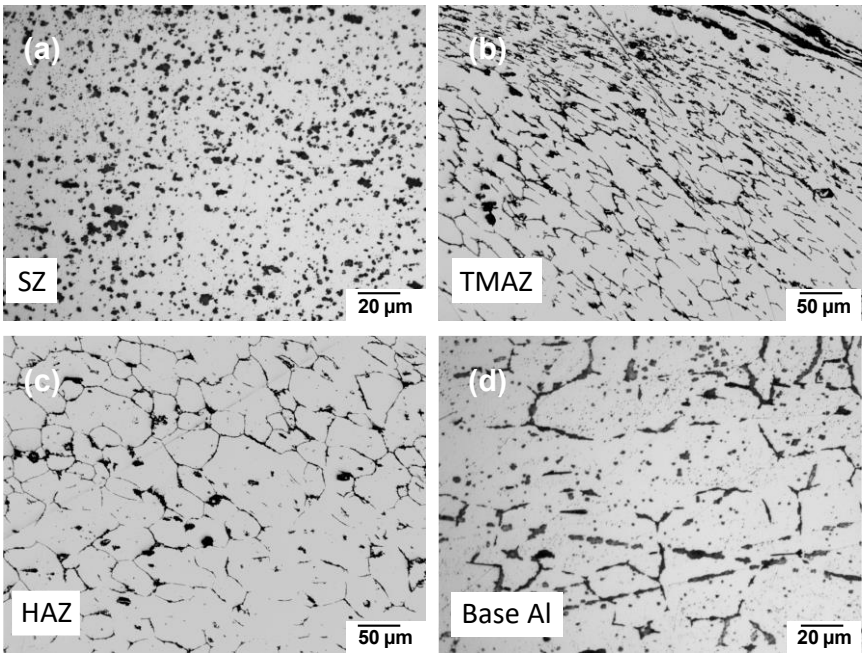

Figure 12 Optical microscopic pictures of a grain structure on etched 6022 Al from a cross-sectional perspective: (a) Stirred zone; (b) thermomechanical affected zone; (c) heat-affected zone; (d) base 6022 Al.

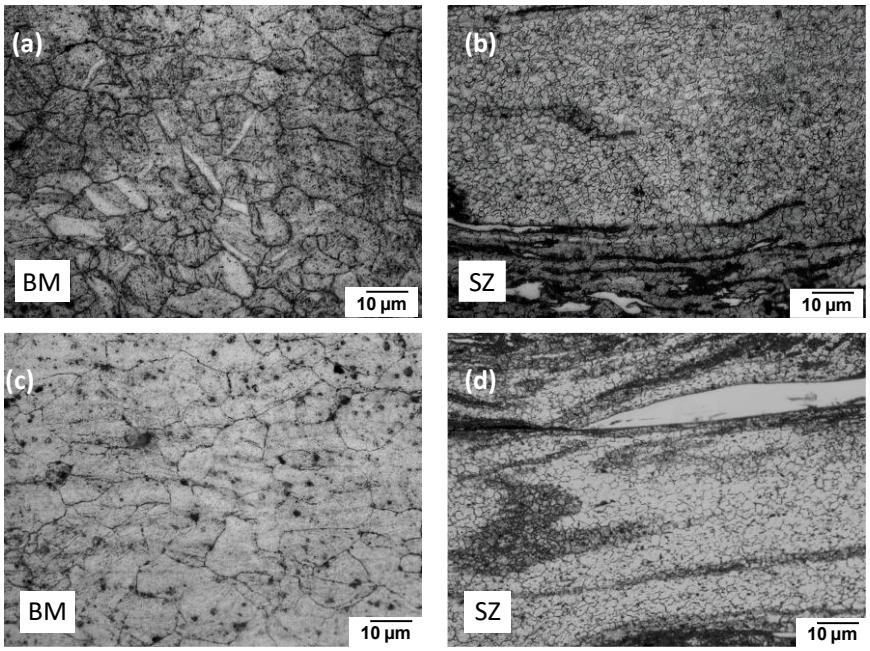

Figure 13 Optical Microscopic pictures of grain structure on etched ZEK100 Mg from cross-sectional perspective. (a) Base alloy; (b) Weld zone.

2.2 Intermetallic Characterization

It is widely reported that there are usually two types of commonly observed intermetallic layers: The Al side has been identified as β-Al_3Mg_2 and the Mg side as a eutectic consisting of γ-$Al_{12}Mg_{17}$ and the Mg-rich phase [37, 38], it could also be found from the Al-Mg binary phase diagram in **Figure 14(a)**. Determining the type of IMCs can happen between 6022 Al and ZEK100 Mg and can make a comparison with the FSW joint. CALPHAD data was used to fit a single Gibbs free energy function representing the system, pure Al Mg binary system with four local minima corresponding to Al-fcc, β-Al_3Mg_2, γ-$Al_{12}Mg_{17}$, Mg-hcp phases. The Gibbs free energy plot is shown in **Figure 14(b)**.

A diffusion-bonded Al-Mg weld was made under 390 °C and 2 h. As a result, two layers of IMCs: $Al_{12}Mg_{17}$ at the Mg side (IMC width ~25 µm) and Al_3Mg_2 at the Al side (IMC width ~65 µm) were observed and characterized by SEM micrograph, as shown in Figure 15(a). The EDS elemental mapping spectra of Mg and Al is shown in Figure 15(b) and Figure 15(c), respectively.

Table 5 lists the EDS line scan results, identifying the two distinct intermetallic layers with their atomic weight percentage. By contrast, the FSW weld at the interfacial bonding region between 6022 Al and ZEK100 Mg in **Figure 16(a)** shows a formless division of the intermetallic layers due to the mechanical intermixing effect. Therefore, selected regions numbered with green boxes were performed using quantitative EDS mapping, and the results for β-Al_3Mg_2 and γ-$Al_{12}Mg_{17}$ IMCs are listed in **Table 6**, which match the XRD results in **Figure 16(b)**.

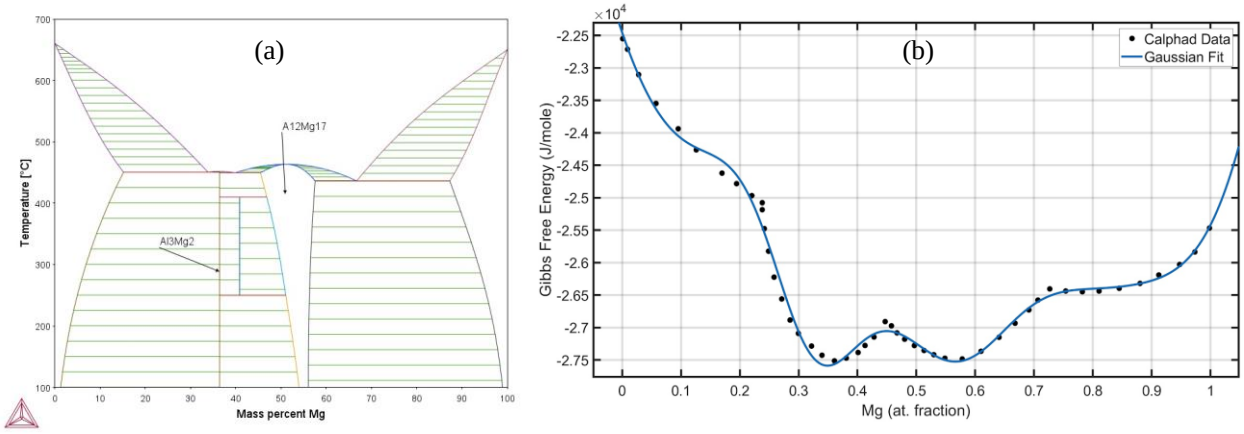

Figure 14 (a) Al-Mg Phase Diagram; (b) Fitted Gibbs free energy function for the Al-Mg system used in the diffusion bonding model.

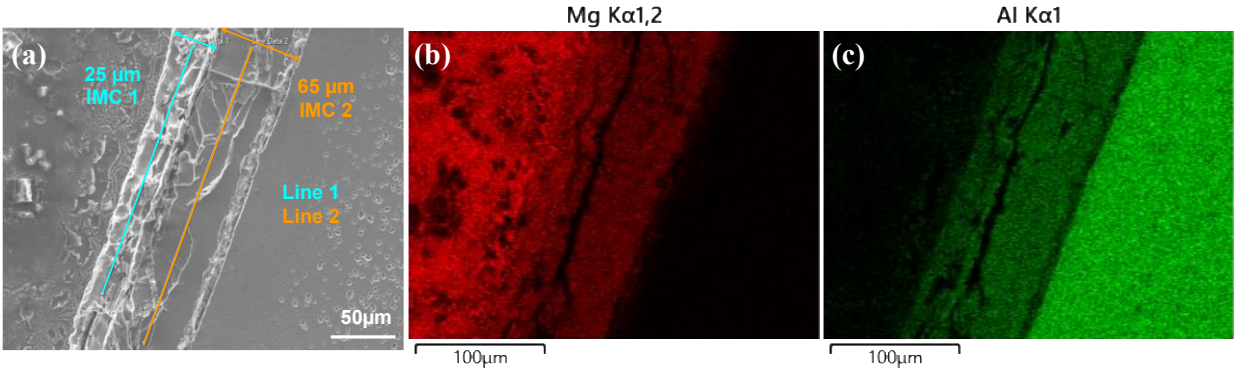

*Figure 15 SEM **(a)** and the respective EDS Mg **(b),** Al **(c)** pictures of diffusion bonded Al-Mg weld which shows clear two intermetallic zones.*

Table 5 Index of EDS Line-Scan results

Line Scan	Al wt%	Mg wt%	IMCs
Line 1	45.1	38.8	$Al_{12}Mg_{17}$
Line 2	57.6	34.2	Al_3Mg_2

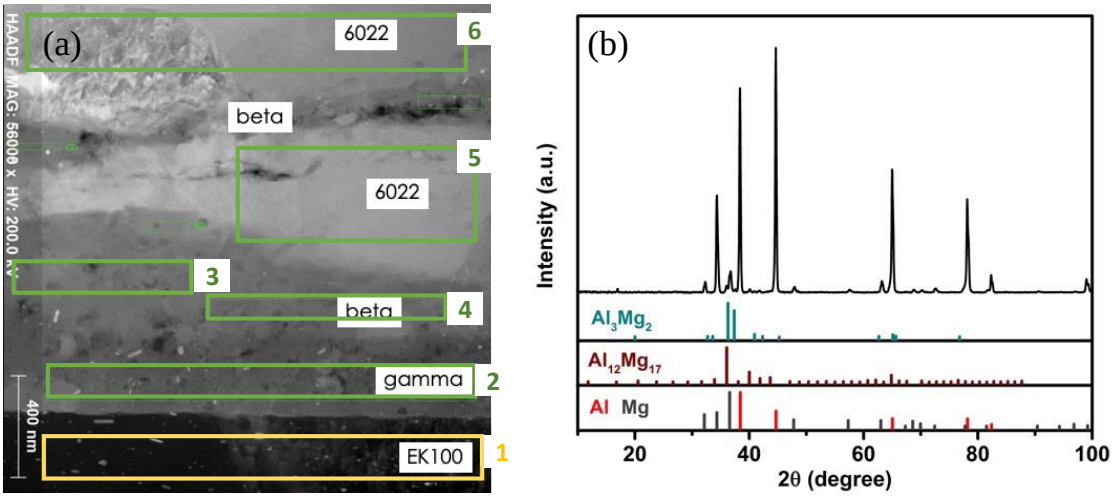

Figure 16 (a) STEM ZC micrograph of the interfacial layer between FSW 6022 Al and ZEK100 Mg; (b) XRD analysis that shows evidence of IMCs.

Table 6 Index of quantitative EDS results.

Region	**Al at%**	**Mg at%**	**Phase Detected**
1	1	96	ZEK100 Mg
2	36	57	γ-$Al_{12}Mg_{17}$
3	57	39	β-Al_3Mg_2
4	57	39	β-Al_3Mg_2
5	93	4	6022 Al
6	95	3	6022 Al

2.3 Secondary Phase Particles

The presence and distribution of these secondary phases can affect the mechanical properties of the alloy, including its strength, ductility, and corrosion resistance. Therefore, understanding the nature and distribution of secondary phases in 6022 Al and ZEK100 Mg alloy is important for optimizing its properties and performance in various applications. For example, **Figure 17** and **Figure 18** list a common type of secondary phase particles in 6022 Al and ZEK100 Mg respectively. As mentioned, the presence of Mg/Si phase could help to increase the precipitation hardening and improve the strength for 6022 Al, however, the segregation of Si particles along the grain boundary could also decrease the ductility of the alloy. The exist of Zn can help to increase the strength and REE element in this case – Nd could improve the grain growth to form finer and equiaxed grains.

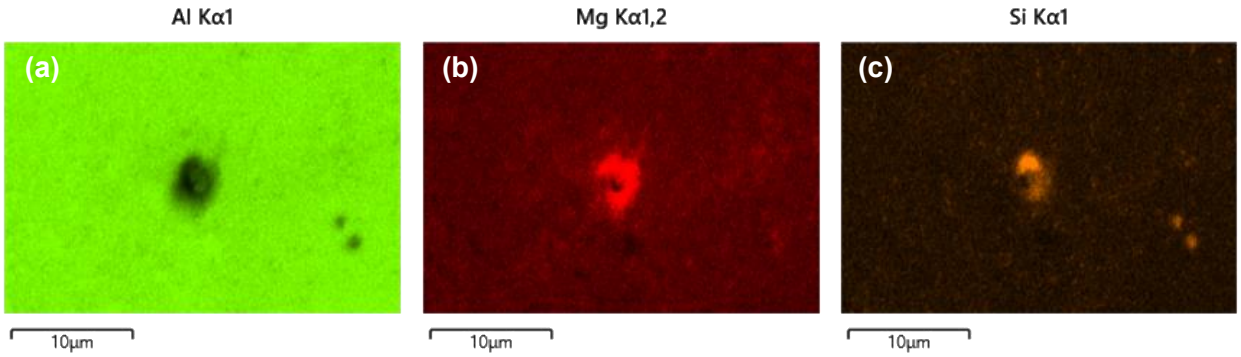

Figure 17 Mg/Si phase from 6022 Al alloy

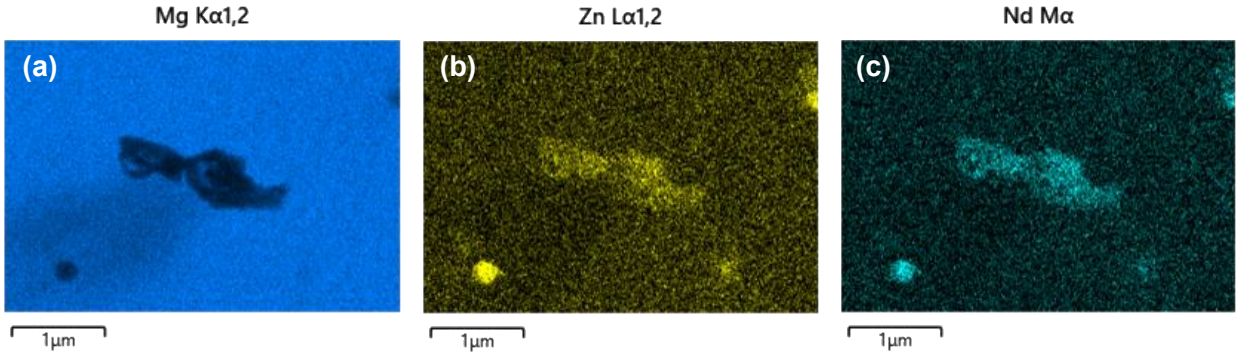

Figure 18 Zn/Nd phase from ZEK100 Mg alloy

It has been reported by Oak Ridge National Laboratory from **Figure 19** that there is micro galvanic corrosion happened between secondary phases and matrix Al alloy from the dynamic recrystallization zone (DMX) during the 0.1M NaCl solution immersion tests. For example, **Figure 20** shows 6022 Al being immersed into 3.5 wt% after 1h also backed up this phenomenon that Fe/Si 2nd phase has higher corrosion potential and served as a cathode while Al matrix having lower corrosion potential will become an anode which could be corroded or dissolved to form a localized micro galvanic corrosion, where the pits could be observed from the SE SEM micrograph in **Figure 20**.

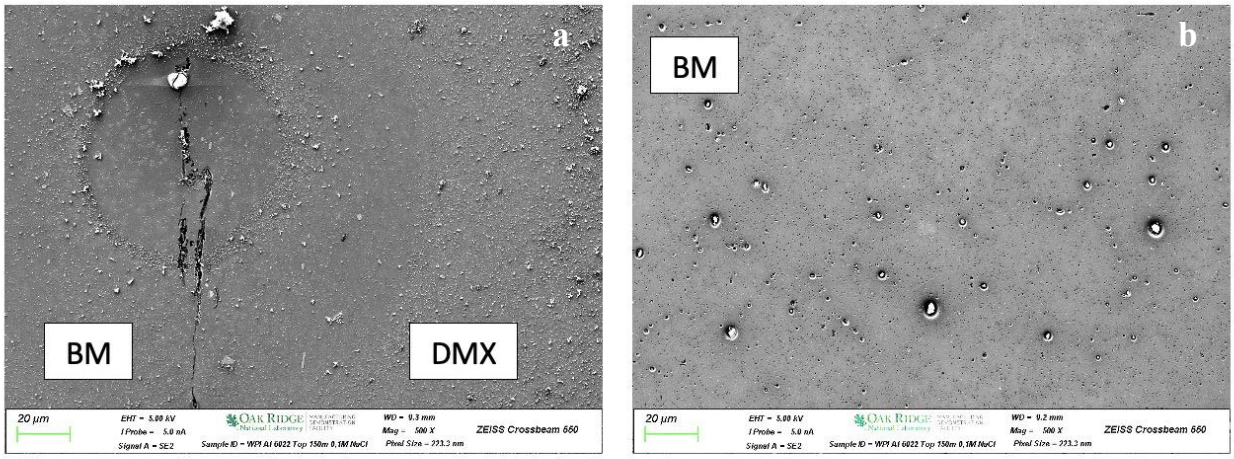

Figure 19 (a) Dynamic recrystallization region of 6022 Al; (b) Fe/Si rich 2nd phase.

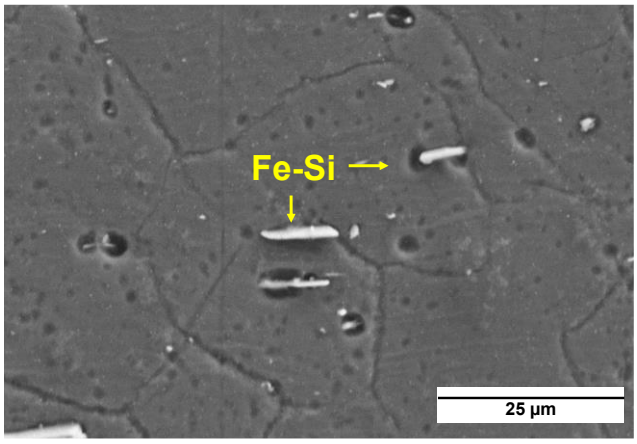

Figure 20 Evidence of Micro-galvanic between Fe/Si secondary phase and 6022 Al matrix.

According to the STEM BF image of the Al-Mg interfacial layer in **Figure 21A** where left side is 6022 Al and right side is ZEK100 Mg, which is under much higher magnification on nanoscale (by Oak Ridge). It can be observed that the middle interfacial layer region contains much smaller grain size (50~150 nm) compared to base Al and base Mg, which could have different behavior on corrosion and mechanical from the corresponding parent alloy beside.

Figure 21B and **Figure 21C** are the X-ray mapping of the region from **Figure 21A**. **Figure 21C** revealed how Al (blue) and Mg (green) distributed at the interfacial region where Mg has a clearer boundary line and a gradient signal away from ZEK100 Mg side. The Mg contrast disappears and reappears around 600 nm above the Mg substrate, which could be evidence of two distinguishing strctures formed during the intermixing process. It also exhibits the distribution of element O (red) in this interfacial region.

Figure 21B excludes element O and Al and focuses on the contrast of element Si (purple) which seems abundant at both 6022 Al side and interfacial region but stopped on ZEK100 Mg area. This image revealed that the intermixing layer or diffusion process mainly happened from Mg towards Al, and makes the interface occurred on Al side, since 6022 Al contains higher content of Si while ZEK100 Mg does not which can be found from **Table 4**. This also could explain that Mg shows a gradient.

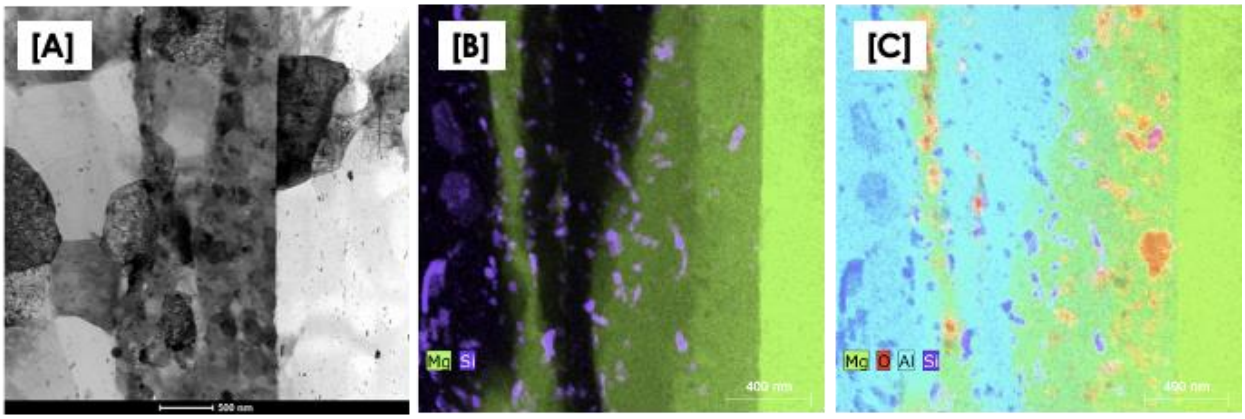

Figure 21 ***(A)*** *STEM BF of the interfacial layer between FSW Al (left) and Mg (right) alloy sheet (scale bar: 500nm);* ***(B)*** *X-ray map of Mg and Si in region* ***(A)****, (scale bar: 400nm);* ***(C)*** *X-ray map of Mg, O, Al, and Si in region* ***(A)****, (scale bar: 400nm).*

3. Experimental Methodologies

3.1 Introduction to the electrochemical methods

The electrochemical studies of the samples were performed by Gamry 600 potentiostat shown in **Figure 22(a)**. And the Paracell kit (**Figure 22(b)**) which designed for the flat specimen was applied where graphite rod act as counter electrode, Ag/AgCl (with saturated KCl electrolyte) as the reference electrode and the sample as working electrode. Prior to start the experiment, the samples were polished up to 1200 µm sized emery paper to remove the native oxide, contaminants and scratches from the surface thereafter washed with acetone. The open circuit potential (OCP), linear polarization resistance (LPR) and potentiodynamic polarization (PD) were conducted to study the corrosion resistance properties of the samples in 3.5 wt.% NaCl solution. The area of the samples was 3.14 cm^2 and it was fixed for each sample. The PD was conducted at 0.1667 mV/s according to ASTM G-59 standard. All the experiments were performed at 25 (±2) ^oC.

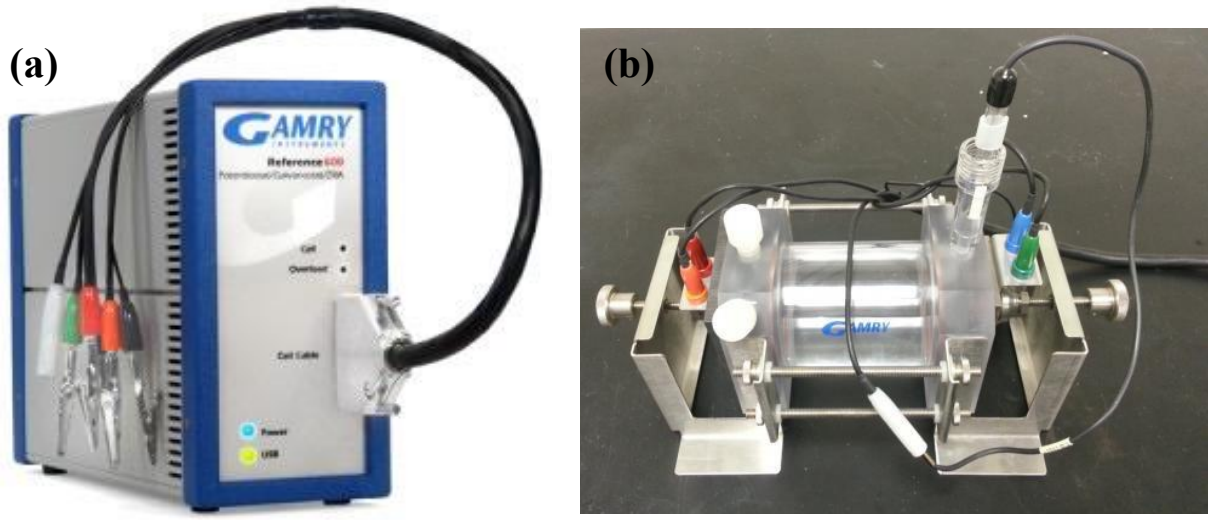

Figure 22 (a) Gamry 600 Potentiostat; (b) The ParaCell™ Electrochemical Cell Kit.

3.1.1 Open Circuit Potential (OCP)

Open Circuit Potential (OCP) is a measure of the electrochemical potential of a metal or metal electrode in a corrosion system. It represents the potential difference between the metal and a reference electrode under open circuit conditions, where there is no current flow between the metal and reference electrode. An electrochemical potentiostat is used to measure the OCP of the sample by applying a constant potential to the reference electrode and measuring the potential difference between the reference electrode and the working electrode. The OCP of a metal can provide information about the potential at which corrosion will occur and can also be used to monitor the progress of corrosion [39]. The OCP of a metal can change as a result of various factors, including the presence of corrosion products, changes in the chemical composition of the metal surface, and changes in the environment surrounding the metal. The OCP is a useful tool for corrosion engineers, as it provides a way to monitor corrosion and to predict the potential for corrosion to occur in a given system.

An applied voltage that is positive of OCP will accelerate oxidation (corrosion) reaction whereas the applied voltage with negative OCP will accelerate the reduction reaction. The terms "OCP" and "E_{corr}" (corrosion potential) can often be used interchangeably. OCP is the starting point of almost all electrochemical corrosion experiment. The OCP data is recorded and analyzed to determine the corrosion behavior of the material. The stability of the OCP, its variation with time, and its shift in response to changes in environmental conditions. Usually, a stable OCP value indicates that the corrosion system has reached a "steady state" and the experiment can now begin. This process may take from a few minutes to a few days. In this case, all the OCP were taking for 3600 seconds.

3.1.2 Polarization Resistance Measurement

Polarization resistance or Linear Polarization Resistance (LPR) refers to the measure of the electrical resistance of a material to an applied potential (voltage) in an electrochemical cell. It is a measurement of the rate at which the reaction at the electrode surface (such as corrosion) occurs and can be used to characterize the corrosion behavior of a material. It is a rapid, non-destructive

testing technique often used in material corrosion research [40]. The smaller the polarization resistance, the more active the material is in corroding and vice versa. A material with high polarization resistance is more resistant to corrosion. In this study, the potential is measured with no current, owing to the polarized material which is usually on the order of ±10 mV relative to its open circuit potential. An induced current could be generated between the working electrode and the counter electrode when the potential of working electrode has been changed. The polarization resistance of the material can be obtained by taking the slope of the potential and current curve. The study by Bonhoeffer and Jena [41] showed that the slope of the polarization curve at corrosion potential is related to corrosion rate of the test samples. Then this slope was defined as polarization resistance R_P based on:

$$R_P = dE/dI \text{ (at } E_{corr})$$

In 1957, polarization resistance was used to calculate the corrosion rate of the material using the Stern-Geary [42] equation:

$$R_P = \Delta E/\Delta i = ß_a ß_c/2.3\ i_{corr}\ (ß_a + ß_c)$$

Where R_P is the slope of the origin of the polarization resistance graph in ohms or ohm-cm^2; i_{corr} is the corrosion current in ampere or ampere/cm^2; $ß_a$, $ß_c$ are the Tafel constant of the Tafel curve in Volts/decade of current [43].

3.1.3 Potentiodynamic Polarization Scan

Potentiodynamic Polarization is a type of electrochemical corrosion test that involves applying a linear voltage sweep to a sample immersed in an electrolyte solution and measuring the resulting current response. The objective of this test is to determine the corrosion behavior of the sample under different applied potentials. Polarization curves are a widely used electrochemical technique to determine the corrosion current density and instantaneous corrosion rate. This is done by extrapolating the cathodic and anodic polarization branches using the Tafel equation [44, 45]. During the test, the potential is swept from an initial value (usually close to the open circuit potential) to a final value, and the resulting current is recorded [46]. From the recorded data, parameters such as corrosion current density, corrosion potential, and polarization resistance can be calculated and used to evaluate the sample's corrosion behavior [47]. Potentiodynamic

polarization is a valuable tool for understanding the mechanisms of corrosion and for comparing the corrosion resistance of different materials [39].

Under Potentiodynamic Scan mode, the potential drives the reaction at the anode or cathode. It is a suitable method to get the information of corrosion potential, current density, passivation onset, oxide film destruction and repassivation susceptibility, etc. [48]. During the potentiodynamic measurements, potential-current curves were automatically recorded by varying the electrode potential from −0.5 to −1.5 V (vs. OCP) at a scan rate of 0.1667 mV/s according to the ASTM G-59 standard.

3.1.4 Electrochemical Impedance Spectroscopy (EIS)

Electrochemical Impedance Spectroscopy (EIS) is a powerful analytical tool used to characterize the corrosion behavior of materials [49-51]. It is a non-destructive technique that measures the impedance of an electrochemical system at various frequencies [52, 53]. The impedance information is then used to obtain a detailed understanding of the corrosion process and to determine the corrosion rate of the material. EIS is based on the principle that the impedance of an electrochemical system is influenced by various physical and chemical processes occurring at the electrode-electrolyte interface. These processes include charge transfer resistance, film resistance, double-layer capacitance, and electrolyte resistance, etc. EIS provides information on the stability and behavior of the corrosion protection systems [54, 55]. Adding an alternating current (AC) signal, of an electrochemical system over a range of frequencies. By analyzing the impedance data as a function of frequency, EIS provides information about the complex electrochemical processes occurring within the system. It is widely used in both academic and industrial research settings, and it has contributed to significant advances in areas such as corrosion science, battery technology, and electrochemical sensing, among others [55].

It is well established that FSW alters the microstructure of the alloy and affects its corrosion resistance. In this study, EIS was also utilized to access the overall electrochemical behavior of the parent alloy and welding area of both 6022 Al and ZEK100 Mg after FSW. To achieve this, Gamry Reference 600 potentiostat with paracell kit consisting of three electrodes was employed,

The EIS spectra were acquired with a sinusoidal perturbation of 10 mV (rms) in the frequency range of 10 kHz to 50 mHz. All the electrochemical tests were carried out in a naturally 3.5% NaCl solution at room temperature.

3.2 Cyclic Corrosion Test (CCT)

The weight loss method is regarded by certain researchers as the "gold standard" of corrosion testing, and it is distinguished for its simplicity [56]. The weight loss is then determined by calculating the difference in weight of the specimen before and after the removal of the corrosion products [57]. In this project, Surface Vehicle Standard-Laboratory Cyclic Corrosion Test method (Figure 23) was selected to create an accelerated corrosion environment for the bimetallic bonds in a cyclic corrosion testing chamber (Figure 24). The Surface Vehicle Standard Laboratory Cyclic Corrosion Test method (SAEJ 2334 [58]) was selected to create an accelerated corrosion environment for the bimetallic joints, which involves 6 hours of humidity mode at 60 °C, 15 minutes of salt spray at room temperature with a salt solution containing 0.5 wt.% of NaCl, 0.1 wt.% of $CaCl_2$ and 0.075 wt.% of $NaHCO_3$ (pH = 7.7), and then 17.45 hours of a dry process at 50 °C as a daily repetition. Eight weeks of repeated loops were conducted in CCT to determine the weight loss of samples due to corrosion. All the samples were polished with the grit 1200 emery paper, cleaned in an ultrasonic bath with ethanol, and dried in air before analysis. Each week after the corrosion exposure, specimens were washed with a solution containing 15 wt.% CrO_3 in an ultrasonic bath for five to ten minutes to completely remove the corrosion products from the sample surface to get an accurate weight loss measurement.

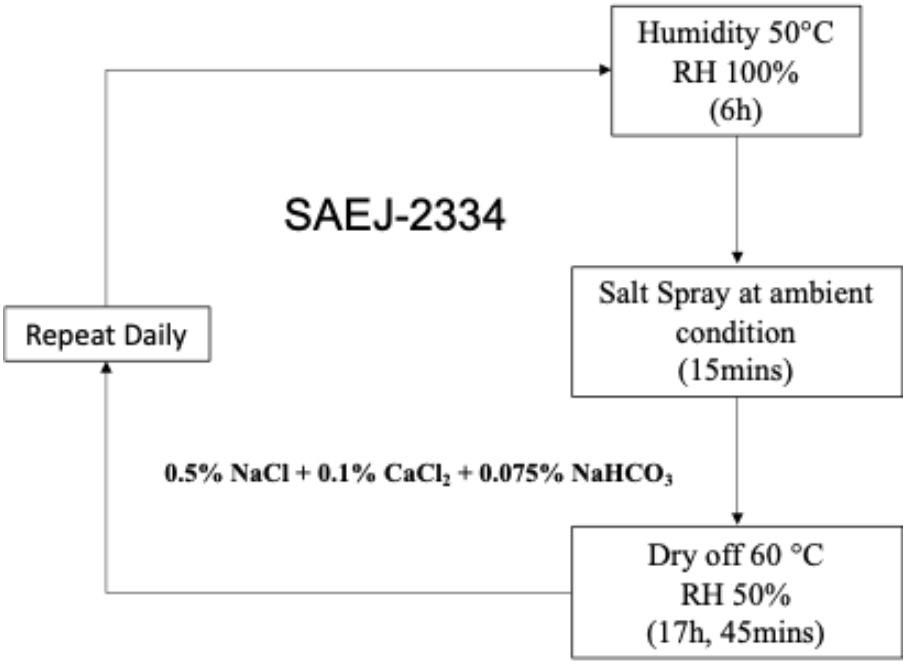

Figure 23 SAE J2334 standard cyclic corrosion test schematic representation [58].

Figure 24 Cyclic corrosion testing chamber.

3.3 Zero resistance ammeter (ZRA) method

The galvanic coupling experiment was carried out in accordance with ASTM-G71 Standard Guide for Conducting and Evaluating Galvanic Corrosion Tests in Electrolytes [59], as shown in **Figure 25**. Anode and cathode materials are immersed into the electrolyte, applied voltage is fixed and the current value vs. time is recorded. Two sets of the examinations were carried out: One is based on the applied voltage effect and the other one dives into studying the distance effect between the two alloys.

In common engineering practice, corrosion rate (r) often expresses in the form of penetration per unit time (mpy and mm/year), and the corrosion rate can be calculated by substituting i_{corr}, current density, measured from Zero resistance ammeter (ZRA). The corrosion rate in solutions can be calculated by [60]:

$$r = 0.129 \frac{ai}{nD} \quad \text{(in mpy)}$$

where, r is corrosion rate in mils (0.001 inches) per year, a is the atomic weight, i is the current density in $\mu A/cm^2$, n is the number of equivalents exchanged and D is the density in g/cm^3.

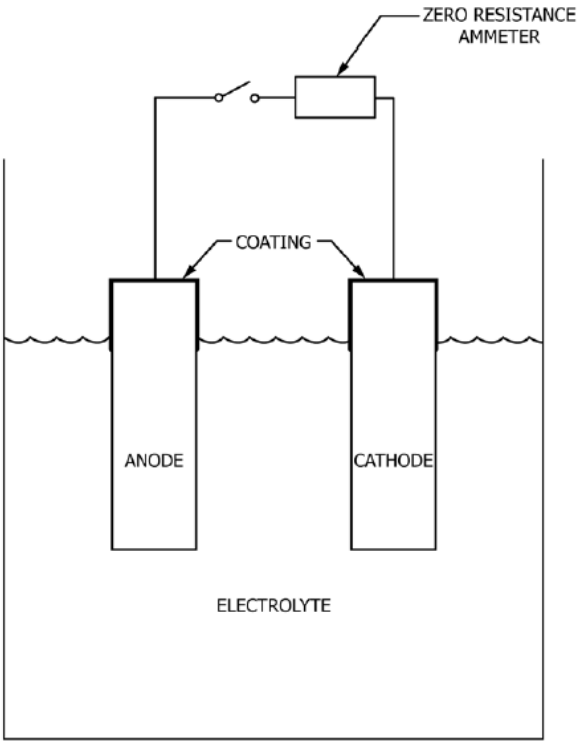

Figure 25 ASTM G71 galvanic corrosion standard schematic diagram.

3.4 Mechanical Testing

3.4.1 Lap-shear Tensile Test

Lap-shear strength of the FSW joints mainly focuses on the bonding strength, especially on the interlocking hook region before and after corrosion. The lap shear strength of samples before and after corrosion was tested with an Instron 5500 tensile tester with a strain rate of 0.762 mm/min.

3.4.2 Microindentation Hardness Test

The Buehler Wilson VH3300 automatic Vickers/Knoop hardness tester was used to get the hardness distribution on the cross-section surface of the Al-Mg welds. As shown in **Figure 26**, the specimen has 6022 Al on top and ZEK100 Mg at the bottom. Each side has 3 rows and 31 columns, the averaged data of each 3 rows will be taken to ensure the reliability. The various values of

hardness will be applied in MATLAB to divide each region of the FSW zone. The indent spacing was 0.4 mm vertically and 0.8 mm horizontally. In this experiment, a Vickers indent with HV 0.3 was applied.

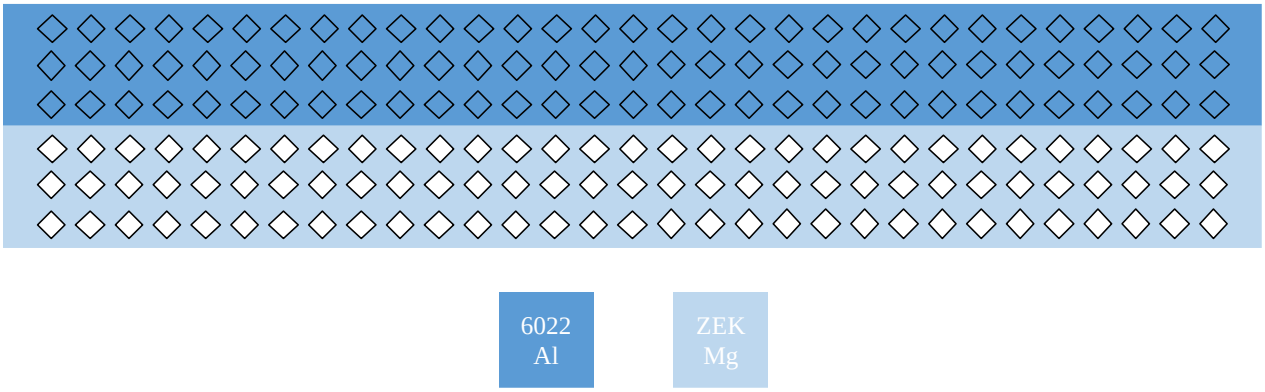

Figure 26 Schematic Microindentation experimental design.

3.4.3 Flat-Punch Nanoindentation for True Stress-Strain Curves

Theory: The true stress-strain curves (σ-ε) of each FSW regions on the micromechanical scale were obtained by a KLA's patented technique with a flat-punch nanoindentation system. The true stress-strain data were analyzed and calculated with a novel developed patent by Hay [61] after fitting the coefficients K and n in Hollomon power law which is defined as:

$$\sigma = K\varepsilon^{n}$$

Where the true strain ε is defined by scaling the indentation depth $\varepsilon = (\frac{2}{\pi})(\frac{h}{a})$. And the true stress is defined by scaling the mean pressure as $\sigma = \zeta P_m$ where ζ is calculated based on the degree of plasticity S^*, which is a stiffness ratio established through hundreds of the finite element simulations of the indentation process over a wide range of materials with various work hardening rates, yield strengths and moduli of elasticity to ensure the versatility.

Experimental Method: A quasi-dynamic loading method was selected with the KLA iMicro Pro Nanoindenter which has a 90° diamond flat-punch tip with a flat and circular apex system approximately 10 μm in diameter. Each FSW region processed 20 indents to get the best fit of parameter *K* and *n*. The indent spacing was 75 μm vertically and 85 μm horizontally.

3.4.4 Fatigue Testing

It is known that the fatigue failure of FSW welds is a gradual process that involves the accumulation of damage over time. This type of failure can occur even when the cyclic stress is below the static strength limit and does not happen abruptly. In fact, it may take a considerable amount of time to occur. The fatigue behavior of FSW joints can be complex and depend on many factors, such as the specific welding parameters, the alloy being welded, the location of the joint, residual stress and the weld defects [30].

In this study, high cycle fatigue tests on FSW specimens with and without adhesive were prepared into a dog bone specimen according to the testing standard ASTM E466-21, example can be found from Su et al. [62] on the lap shear fatigue testing (**Figure 27**). These tests applied minimum to maximum force ratio R=0.1±0.2 and frequency of 20 Hz, targeting lifetime at 10^4, 10^5 and 10^6. **Figure 28** shows the specimens cut by electrical discharge machining (EDM) from FSW samples produced at PNNL.

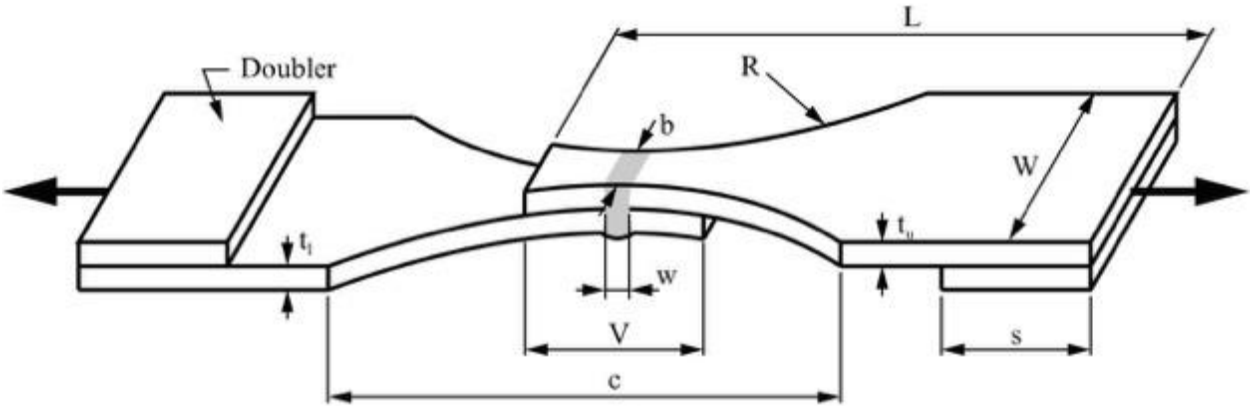

Figure 27 EDM cut Al-Mg lap welds Dog bone geometry design for fatigue testing from Su et al. [62].

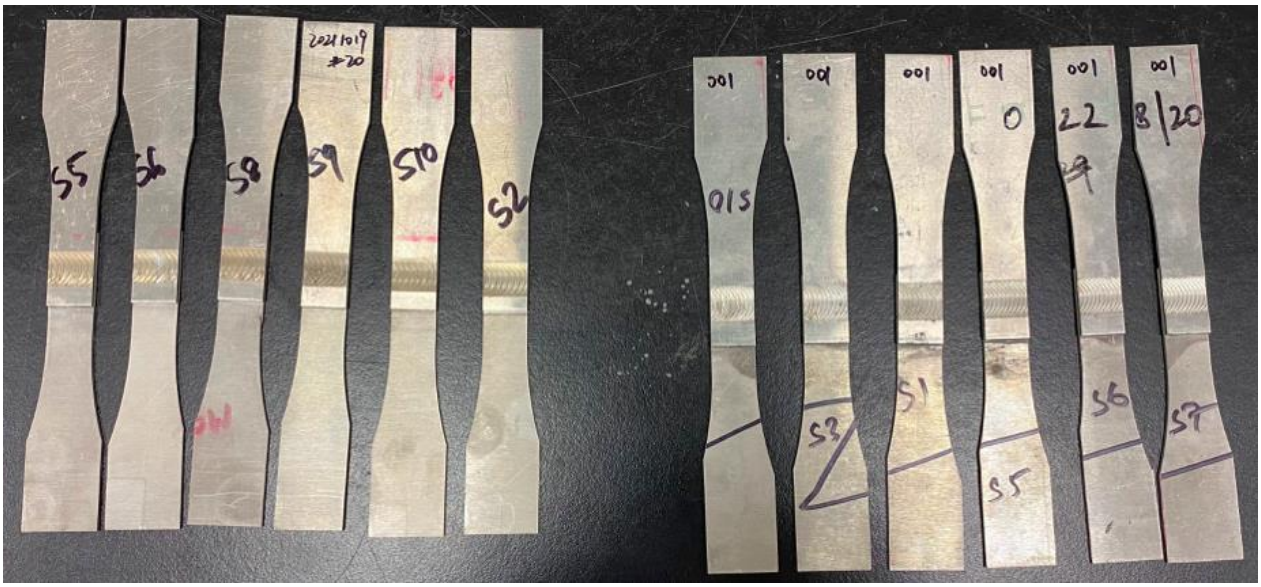

Figure 28 Specimens cut by EDM for fatigue testing. (Left: FSW, Right: Adhesive-FSW).

4. Results and Discussion

4.1 Electrochemical Experiments

4.1.1 Open Circuit Potential Test

In the 3.5 wt.% NaCl solution, the open circuit potential (OCP) values of the 6022 Al and ZEK100 Mg alloys were measured for 3600 s, as shown in **Figure 29**. The OCP of the 6022 Al alloy was found to be higher than that of the ZEK100 Mg alloy, indicating increased corrosion activity as Mg is more galvanically active than Al and is the most active of all engineering materials. During the first 600 s of immersion, the OCP of the 6022 Al alloy shifted from −0.76 V to approximately −0.69 V vs. Ag/AgCl and stabilized at around −0.70 V for the remaining time. Similarly, the OCP of ZEK100 Mg alloy increased from −1.48 V to −1.44 V after 600 s and stabilized at around −1.43 V. The initial rising behavior in OCP for both alloys is attributed to the formation of a passive film on the surface during the immersion time. However, due to the intermixing process by stir welding, it is observed that the weld zones (WZ) of 6022 Al and ZEK100 Mg have very close OCP values, and they are more adjacent to ZEK100 Mg. This indicates that during the FSW process, the

overlapping region of the top Al alloy could be mixed with the bottom Mg alloy to form a layer where they could have quite similar electrochemical behaviors.

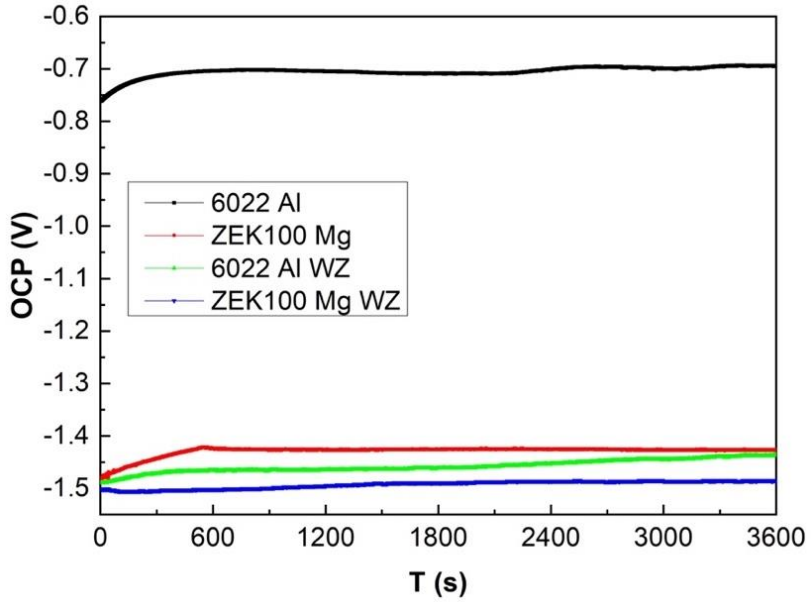

Figure 29 OCP plot for 6022 Al, ZEK100 Mg and their weld zone respectively.

4.1.2 Polarization Resistance Test

The LPR results of the samples are shown in Figure 30. The potential and current of 6022 Al alloy is lower compared to ZEK100 Mg alloy. The Mg alloy exhibited 32.26 mpy (0.16 g/m^2/h) while Al shows 1.08 mpy (0.0084 g/m^2/h) using Stern-Geary equation, which can be compared with the weight loss experiments later. This result suggested that Mg alloy is much more susceptible to corrosion in NaCl solution.

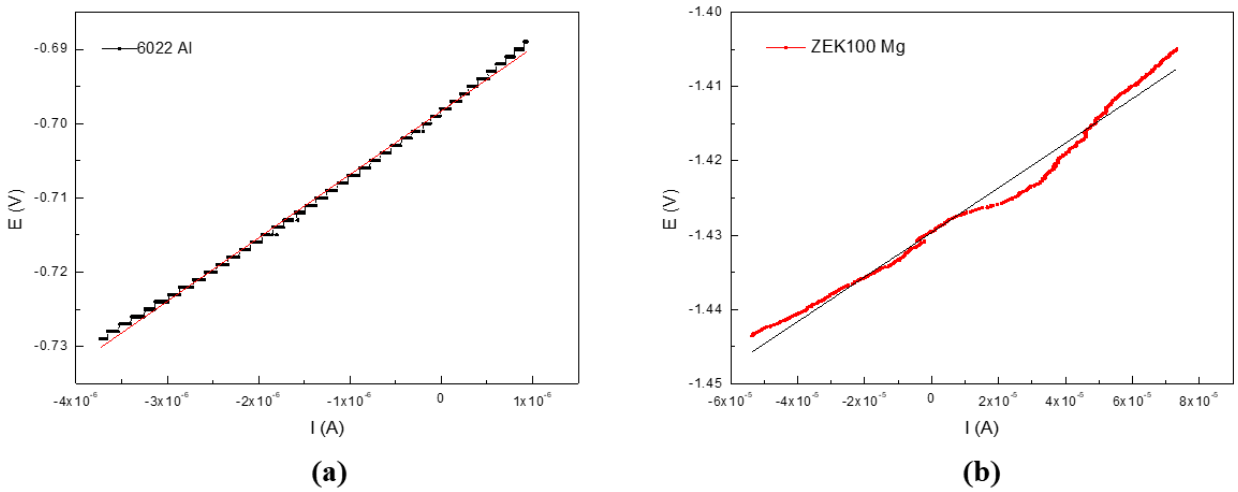

Figure 30 Polarization Resistance plot for (a) 6022 Al (b) ZEK100 Mg.

4.1.3 Potentiodynamic Scan

Figure 31 illustrates the potentiodynamic scan of 6022 Al, ZEK100 Mg, and their corresponding weld zones. The current density (i_{corr}) of 6022 Al alloy is lower than that of ZEK100 Mg alloy, while the two weld zone materials exhibit the highest current density. The anodic current density of ZEK100 Mg alloy increases significantly from the corrosion potential, whereas the Al alloy displays the trans-passive region around −0.55 to 0.50 V vs. Ag/AgCl, suggesting the formation of part of a passive film during anodic scanning. The higher cathodic current density of Mg alloy is due to the presence of Mg, which makes oxygen reduction dominant. The E_{corr} and i_{corr} in these different regions are calculated by fitting potentiodynamic polarization plots in the Tafel regions. **Table 4** summarizes the electrochemical parameters of these two base alloys and their welding area. The E_{corr} value is in the order of BM-ZEK Mg < Mg WZ ≅ Al WZ < BM-6022 Al, which is consistent with the OCP test results in **Figure 29.** In contrast, the materials from the welding region exhibit a higher current density than the base metal, which may contribute to the mixing of two distinct materials and result in a higher galvanic corrosion rate in these areas.

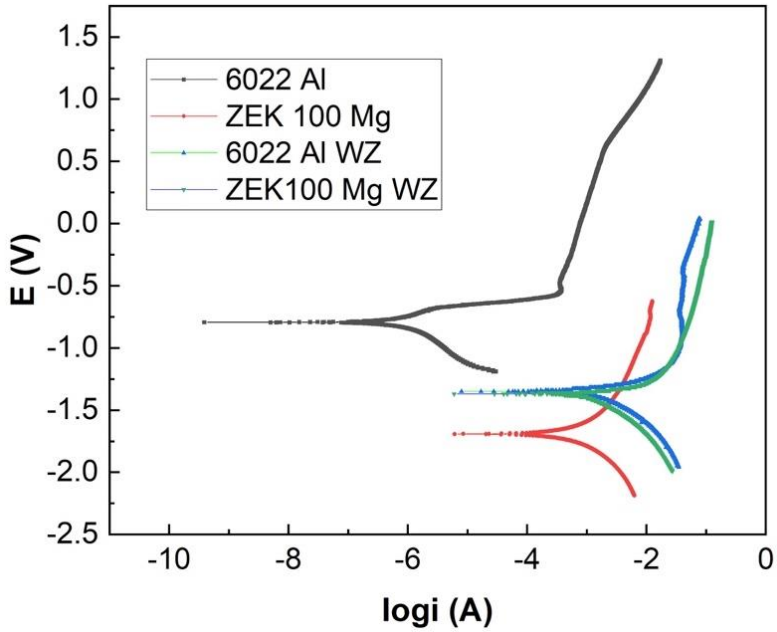

Figure 31 Potentiodynamic plots on 6022 Al, ZEK100 Mg and their weld zone respectively.

4.1.4 Electrochemical Impedance Spectroscopy (EIS)

Upon fitting on the Nyquist plots, it can be discerned that ZEK100 Mg exhibits two semicircles (**Figure 32**), while 6022 Al presents a single semicircle with a Warburg line at low frequency (**Figure 33**), indicative of the presence of two interfaces, between the electrode and electrolyte, that could undergo electrochemical reactions, governed by charge transfer control. Conversely, for 6022 Al, high frequency reveals charge transfer control on the electrode interface, whereas low frequency reflects mass transfer control.

This finding provides evidence that upon immersion in a 3.5% NaCl solution, the as-polished ZEK100 Mg rapidly forms its corroded film, $Mg(OH)_2$, which results in the formation of two distinct electrochemical systems -- between electrolyte with Mg base alloy and between electrolyte with $Mg(OH)_2$ film. Whereas the as-polished 6022 Al only has a single electrochemical system, could be suggested that limited time for the passivation Al oxide film to grow.

Equivalent circuit was modeled on ZVIEW with the fitted parameters listed in Table 7 and Table 8 for ZEK100 Mg and 6022 Al respectively. From the resistance value it can be found that Al and Mg has similar R_s value which is the resistance of the electrolyte, as expected. However, 6022 Al has much higher charge transfer resistance than ZEK100 Mg, which can be read both by a larger radius of the semicircle and the R_{ct} value from the tables. This result again backed up the conclusion that Mg alloys will corrode faster than Al alloys under the same electrolyte.

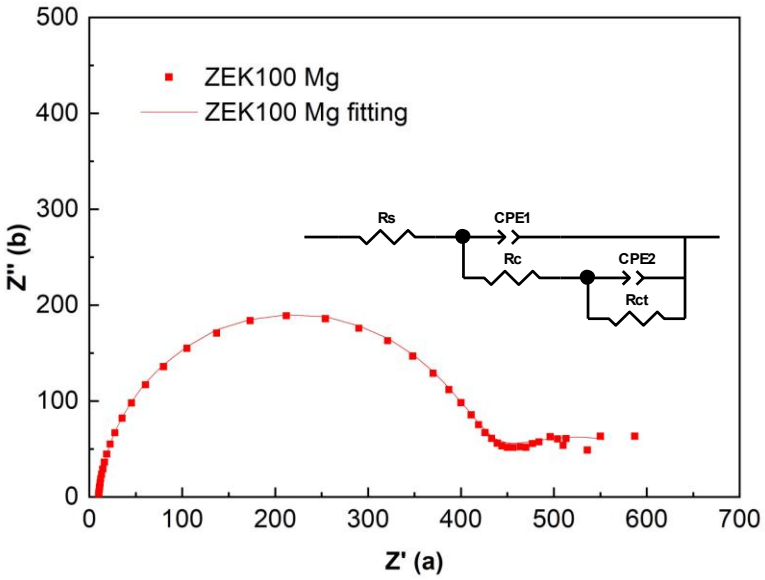

Figure 32 EIS plot on ZEK100 Mg with its equivalent circuit.

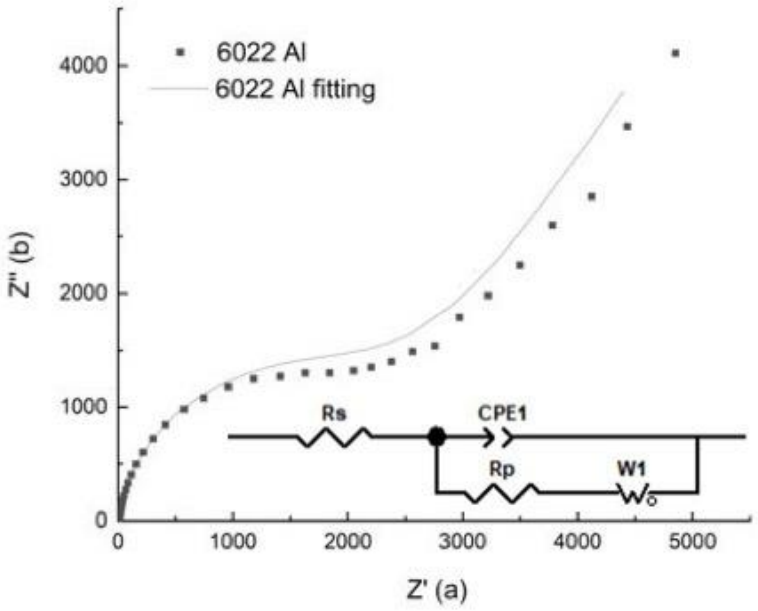

Figure 33 EIS plot on 6022 Al with its equivalent circuit.

Table 7 Parameters of the equivalent circuit model on ZEK100 Mg.

Element	Value	Error	Unit
R_s	9.833	1.16E-01	ohm
R_{ct}	233.2	75.7	ohm
R_c	408.4	11.19	ohm
CPE2-T	7.42E-03	1.06E-03	S*s^a
CPE2-P	5.93E-01	8.79E-02	
CPE1-T	2.50E-05	1.34E-06	S*s^a
CPE1-P	9.35E-01	7.78E-03	

Table 8 Parameters of the equivalent circuit model on 6022 Al.

Element	Value	Error	Unit
R_s	9.46	8.41E-02	ohm
CPE	5.57E-05	1.08E-06	S*s^a
Alpha	0.94	3.34E-03	
W	4.69E-04	1.10E-05	S*s^(1/2)
R_{ct}	2.14E+03	52.94	ohm

However, on the overlapping welding zone, it is interesting to find that both Mg WZ (**Figure 34**) and Al WZ (**Figure 35**) have two semicircles with even smaller radius, having very different electrochemical property with their parent alloy [63]. And it can be suggested that the formation of the intermetallic layers at these regions could build the other reactive system which also has distinct corrosion properties with the two base alloys. From the radius as well as the R_{ct} value which can be read from **Table 9**. And from **Table 10** it can be suggested that intermetallic layers have lower charge transfer resistance compared to the base alloy detected by electrochemical impedance spectroscopy.

Another different behavior on weld zone materials is that both Mg WZ and Al WZ are showing negative impedance values under low frequency. Usually at low frequencies, the impedance of an electrochemical system is primarily determined by the double layer capacitance and the diffusion of charged species in the electrolyte. As the frequency decreases, the time required for charged species to diffuse across the electrolyte increases, leading to a decrease in the impedance value. However, the negative impedance observed at low frequencies can be attributed to several factors, including the presence of redox couples, adsorption of species onto the electrode surface, or the formation of surface films. In this study, the mostly likely phenomenon is the formation of IMC species onto the electrode surface can lead to a negative capacitance effect, this can occur when the formed IMC layer that has a different charge polarity compared to the underlying electrode surface [63].

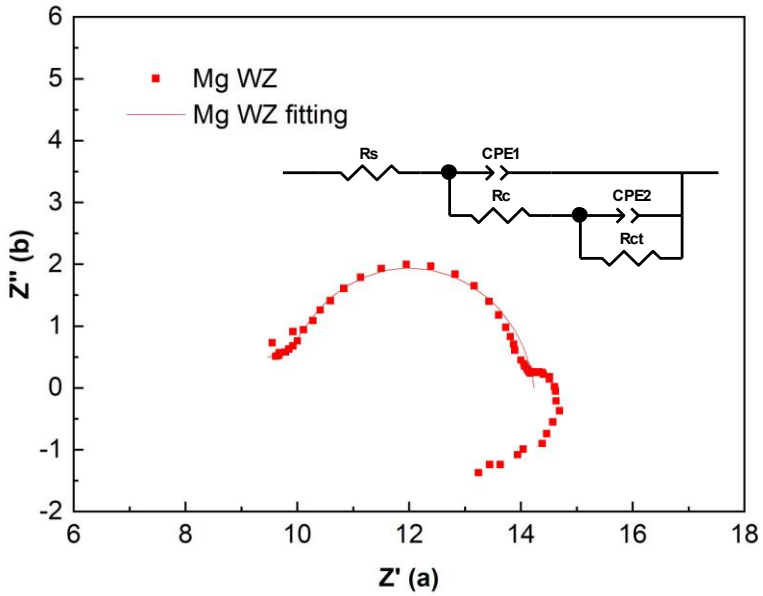

Figure 34 EIS plot on ZEK100 Mg WZ with its equivalent circuit.

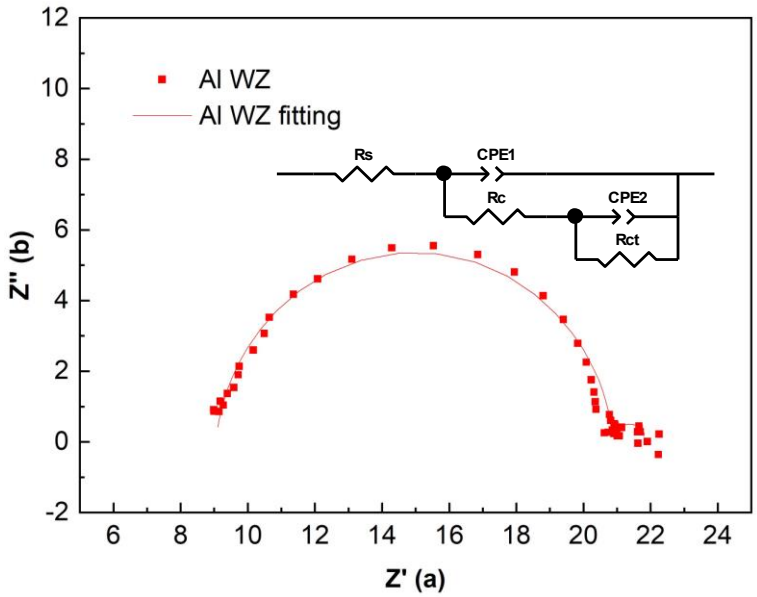

Figure 35 EIS plot on 6022 Al WZ with its equivalent circuit.

Table 9 Parameters of the equivalent circuit model on ZEK100 Mg WZ.

Element	Value	Error	Unit
R_s	8.63	4.87	ohm
R_{ct}	4.28	0.79	ohm
R_c	1.40	5.47	ohm
CPE2-T	3.39E-04	3.61E-04	S*s^a
CPE2-P	0.91	0.15	
CPE1-T	1.55E-05	1.34E-06	S*s^a
CPE1-P	0.93	2.01	

Table 10 Parameters of the equivalent circuit model on 6022 Al WZ.

Element	Value	Error	Unit
R_s	9.05	0.12	ohm
R_{ct}	0.98	0.48	ohm
R_c	11.84	0.23	ohm
CPE2-T	0.69	0.42	S*s^a
CPE2-P	1.00	0.44	
CPE1-T	7.50E-05	1.25E-05	S*s^a
CPE1-P	0.94	0.02	

4.2 Cyclic Corrosion Test

4.2.1 Weight loss measurement

As mentioned, every 2 weeks after the corrosion exposure, all the specimens were washed with a solution containing 15% CrO_3 in deionized water for 5 minutes to remove the corrosion products

from the sample surface to get the accurate weight loss. Both galvanic corrosion on the Mg and Al boundary as well as the oxidation reaction on Mg and Al each side will take place in the corrosion chamber simultaneously. In this work, the assumption is given that the mass loss is mainly based on Mg side since the anode shall be corroded most severely in galvanic corrosion.

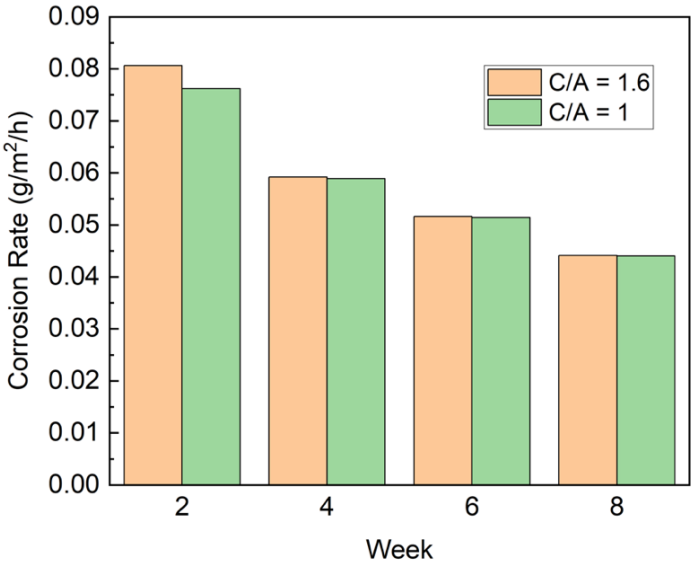

Figure 36 Corrosion rate vs. cathode: anode ratio index.

Figure 36 represents the corrosion rate for two groups of FSW samples with different cathode to anode ratios, tested for eight weeks. The results showed that larger cathode areas were associated with a higher corrosion rate than smaller cathodes in most of the groups. This result matches the reported conclusion of the area effect in galvanic corrosion: for a given bimetallic corrosion system, a larger cathode or smaller anode means having a higher current density on the anode and therefore a greater corrosion rate [64]. It is reported at the initial corrosion stage it will form a thin $Mg(OH)_2$ film [65] based on equation (2), (3) and (4) during corrosion, however, when Cl^- exists, this film is easily attacked and penetrated by Cl ions and then formed a porous structure as shown in **Figure 37(a)** (corroded for 1 week in corrosion chamber). The initial pitting corrosion was usually caused by aggressive anions corresponds to a critical potential where the adsorption capacity of chloride ions is stronger than that of oxygen atoms or water molecules [66, 67]. And the aggressive anions can propagate into the tiny pores and make the breakdown potential even more negative.

$$\text{Anodic: } Mg \rightarrow Mg^{2+} + 2e^{-} \quad (2)$$

$$\text{Cathodic: } O_2 + 2H_2O + 4e^{-} \rightarrow 4OH^{-} \quad (3)$$

$$Mg^{2+} + 2H_2O \rightarrow Mg(OH)_2 + 2OH^{-} \quad (4)$$

With continued corrosion under cyclic conditions, the film can thicken, and cracks will appear. Within the cracks, water vapor condenses, and corrosive gases will be absorbed. These cracks provide a diffusion path for corrosive ions into the matrix, forming severe local corrosion at the early stage. Another result that can be observed from **Figure 36** is the gradually decreased corrosion rate occurs biweekly. Magnesium corrosion products, for example, brucite from Equation (4) and XRD result in **Figure 37(b)**, are likely to have a 'repassivation' effect, which could decelerate the corrosion rate before the film was attacked by the aggressive ions.

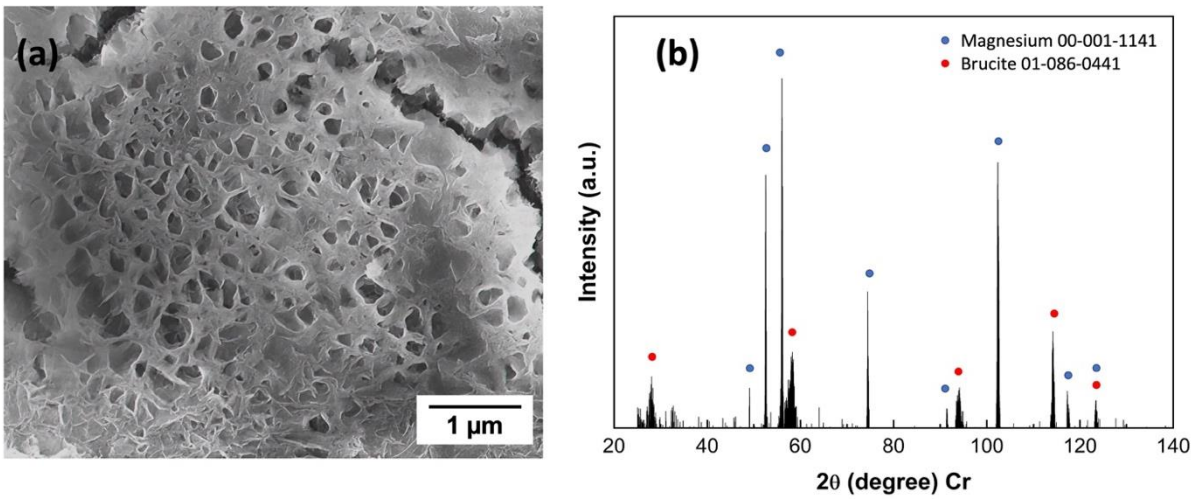

Figure 37 (a) SEM images on ZEK100 Mg side of micro-pits within grains after 1 week; (b) XRD result of the corrosion product on Mg.

To understand the mechanism of corrosion attack on the ZEK100 Mg side, another FSW specimen was prepared and immersed into 0.1 M NaCl salt solution for 1 h by Oak Ridge. **Figure 38** is the

cross-sectional view of the X-ray element mappings from the FIB-lifted corrosion filament on ZEK100 Mg. Directly below the filament, the elements of Mg, Cl, O, Zn, and Zr highlight specific details on the oxide material in the filament region. Interestingly, the filament has a gradient of oxygen, a higher oxygen content at the base, and it decreases as it moves toward the upper surface. However, Mg shows an opposite gradient behavior compared to O, which indicates the adsorption behavior of O and the consumption of Mg. It is also interesting to note that Cl ions accumulate only in the base of the filament, which backs up the explanation that Cl ions can be small enough and easily penetrate through the corroded portion into the basement of the materials and lead to degradation of the materials.

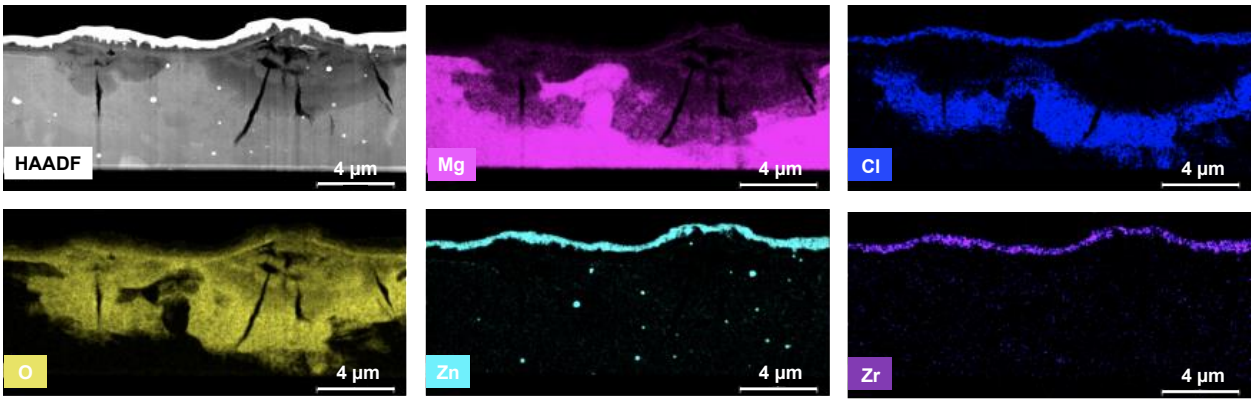

Figure 38 STEM/EDS of the FIB lamella and corresponding X-ray maps displaying the spatial location of Mg, Cl, O, Zn, and Zr in the corrosion product of ZEK100 Mg.

4.2.2 Morphology evaluation

SEM images are analyzed every week after the cyclic corrosion tests begins. The mounted FSW samples have been polished to remove the mechanical scratches and subsequently cleaned with ethanol in an ultrasonic bath. **Figure 39 (a-c)** clearly showed that the pits were initiated and developed severely towards Mg side. **Figure 39 (d-i)** provided evidence that under such corrosion exposure environment, there could be a large crack developed on the alloy boundary which will cause the danger of mechanical failure. The SEM images gathered each week will provide a valuable database for modelling to predict further pit development, which is critical for the

material's damage tolerance [68]. It is interesting to observe that corrosion has mostly occurred around the hook region. This could be explained by (1) Hook region has a higher chance of developing crevices, which could lead to the development of crevice corrosion; (2) Hook region has relatively larger cathode area which could accelerate the galvanic corrosion. (Note: For the program setting issue, these results obtained under more aggressive cyclic conditions where samples were kept on salt spray mode for 1 hour instead of 15 minutes).

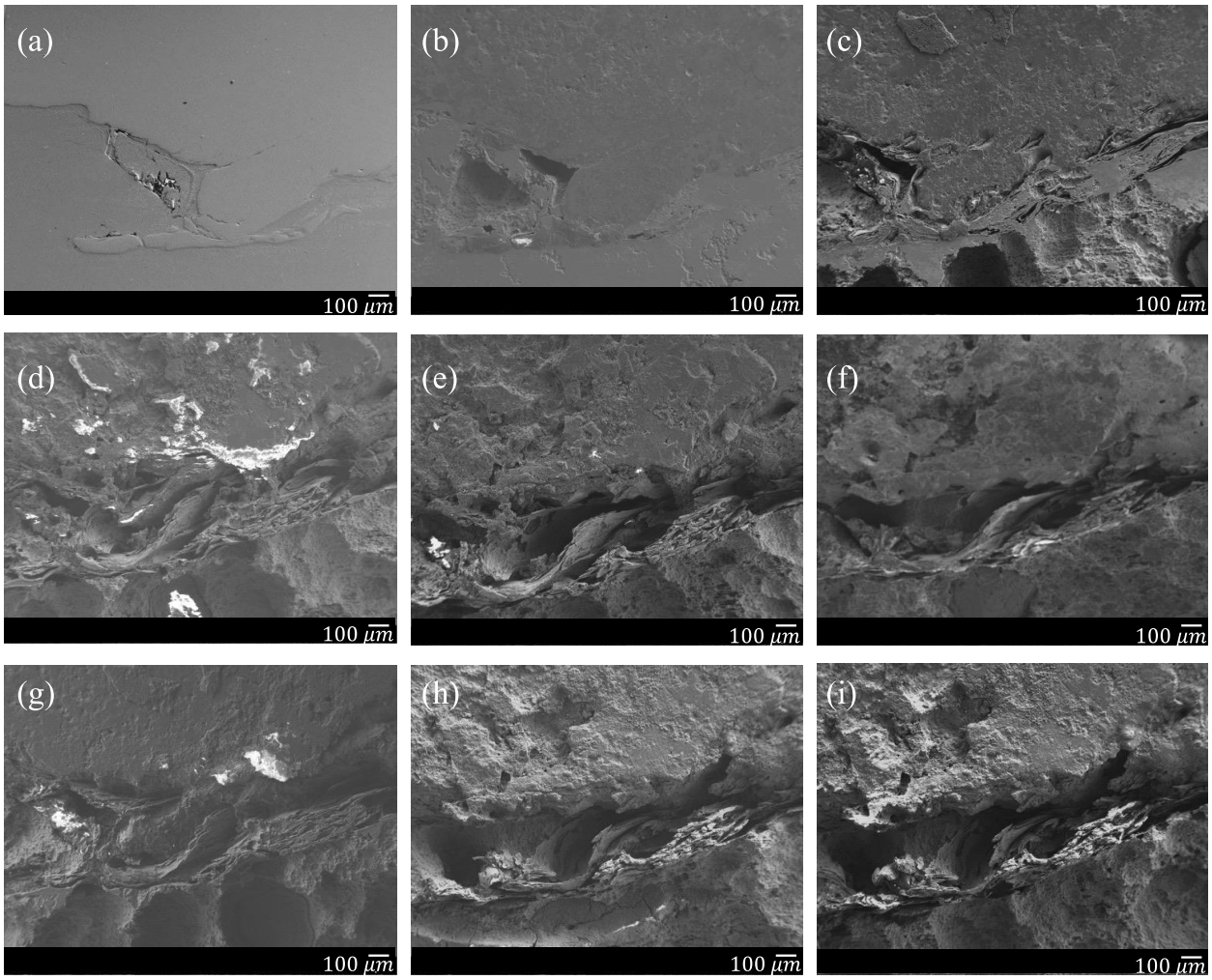

*Figure 39 SEM SE images from one of the mounted samples **(a)** before of CCT and under more aggressive condition for 1-8 weeks **(b-i)** respectively.*

4.3 Galvanic Corrosion Test

4.3.1 Applied voltage effect

In the first set of experiment the corrosion rates have been calculated at 0.5 V and 1 V applied voltages to the anode, respectively in **Figure 40**.

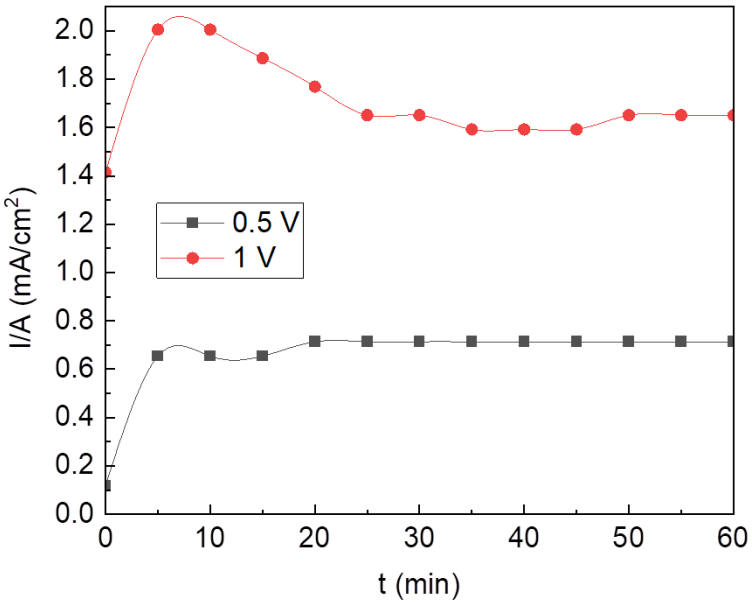

Figure 40 Current density vs time under 0.5 V and 1 V applied potential.

By taking the averaged value of the current density and using the equation mentioned in section 2.2, the corrosion rate can be calculated as follows:

0.5 V: Corrosion Rate = 0.129 × (0.654 × 1000) × 24/2/1.738 = 582.50 mpy
1 V: Corrosion Rate = 0.129 × (1.7 × 1000) × 24/2/1.738 = 1514.15 mpy

The result indicates that higher voltage potential is applied on an anode could significantly increase the corrosion rate in a galvanic corrosion system.

4.3.2 Anode to Cathode distance effect

During the next experiment, the cathode and anode were moved closer to each other, and the same applied voltage (0.5 V) was used to test the effect of distance on galvanic corrosion rate. In **Figure 41**, the full distance represents the diameter of the beaker about 8 cm, whereas the half distance represents the radius which is around 4 cm.

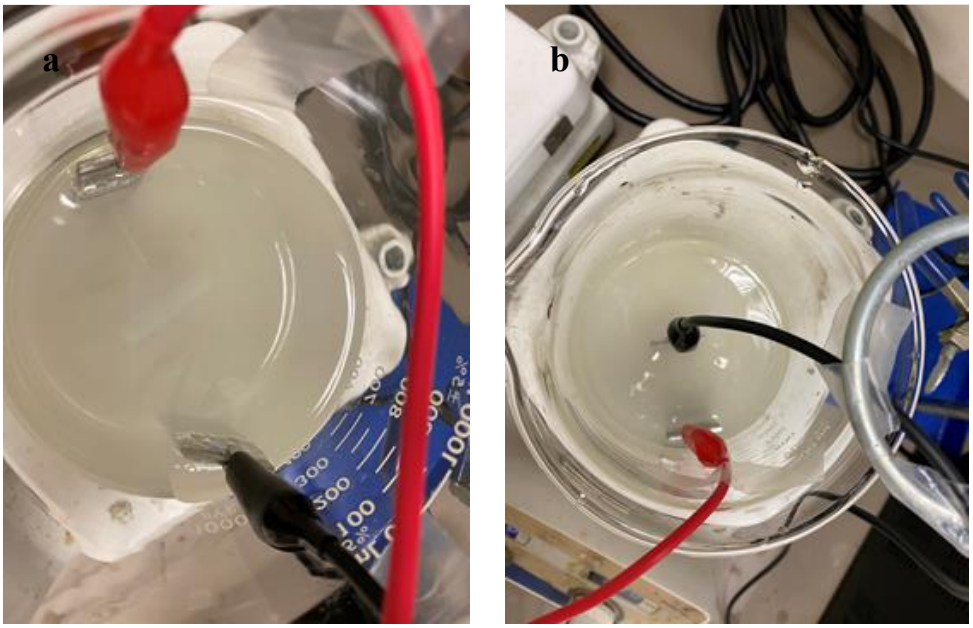

*Figure 41 Corrosion testing apparatus showing **(a)** 8 cm and **(b)** 4 cm width spacing between the electrodes.*

Similarly, after taking the averaged value of the current density the corrosion rate was calculated using the same method:

Full: Corrosion Rate = 0.129 × (1 × 1000) × 24/2/1.738 = 890.68 mpy

Half: Corrosion Rate = 0.129 × (1.29 × 1000) × 24/2/1.738 = 1148.96 mpy

The results of this experiment demonstrate that as the two electrodes approach one another, the rate of corrosion accelerates. This phenomenon can be attributed to the fact that galvanic corrosion

is a form of localized corrosion that is confined to the contact area between dissimilar metals. The corrosion rate diminishes significantly with increasing distance from the point of contact, even by only a few centimeters. This effect is more pronounced when the conducting electrolyte is of poor quality [69]. These findings highlight the importance of maintaining a considerable distance between dissimilar alloys in order to mitigate the rate of galvanic corrosion.

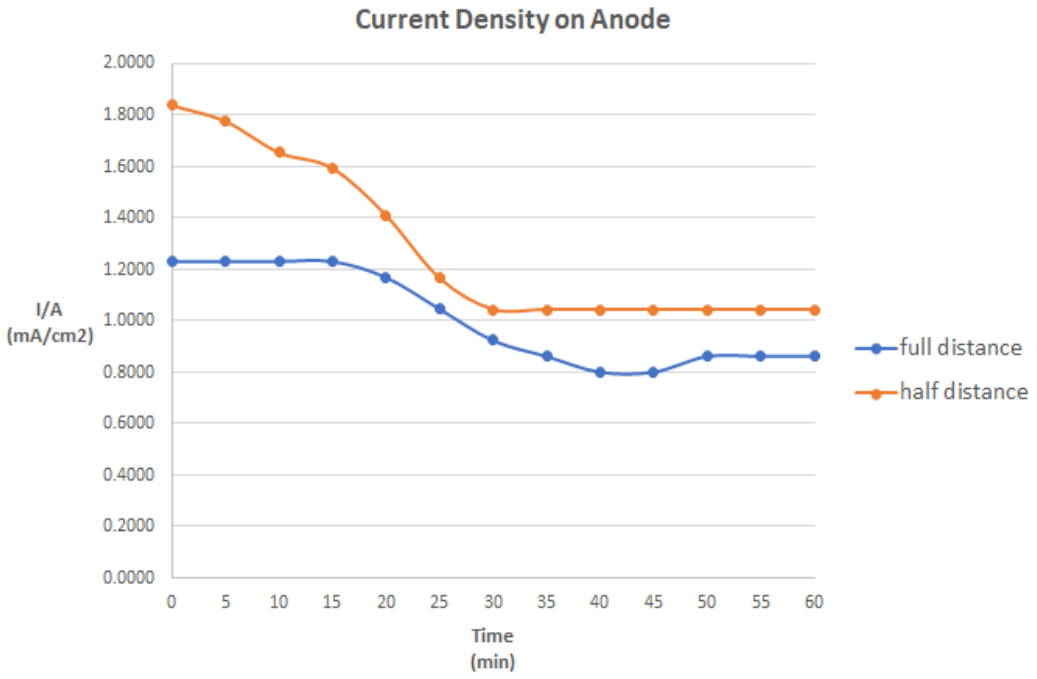

Figure 42 Distance effect on the Current density vs. time.

4.3.3 Pit depth measurement

The pit depth after galvanic corrosion under different conditions is measured in Oak Ridge by a Keyence VR3000, non-contact high accuracy wide-area 3D measurement system to help understand how quantitative depth measurements are acquired from corrosion pits. In this case, 9 pits were selected on 0.5 V (Figure 43a) and 1 V (Figure 43c) on Mg corroded specimen and the Histogram of quantitative pit depths values were provided in Figure 43(b) and Figure 43(d) respectively. Area 1 is the reference plane from which the height difference was determined for pits 2-10. It can be concluded from the averaged value that 1 V Mg specimen has the pit depth

nearly double of the 0.5 V one. Similar test was also conducted on cathode 6022 Al, and from the averaged number which shows in Table 11 we could see a very similar pit depth value on 0.5 V and 1 V sample.

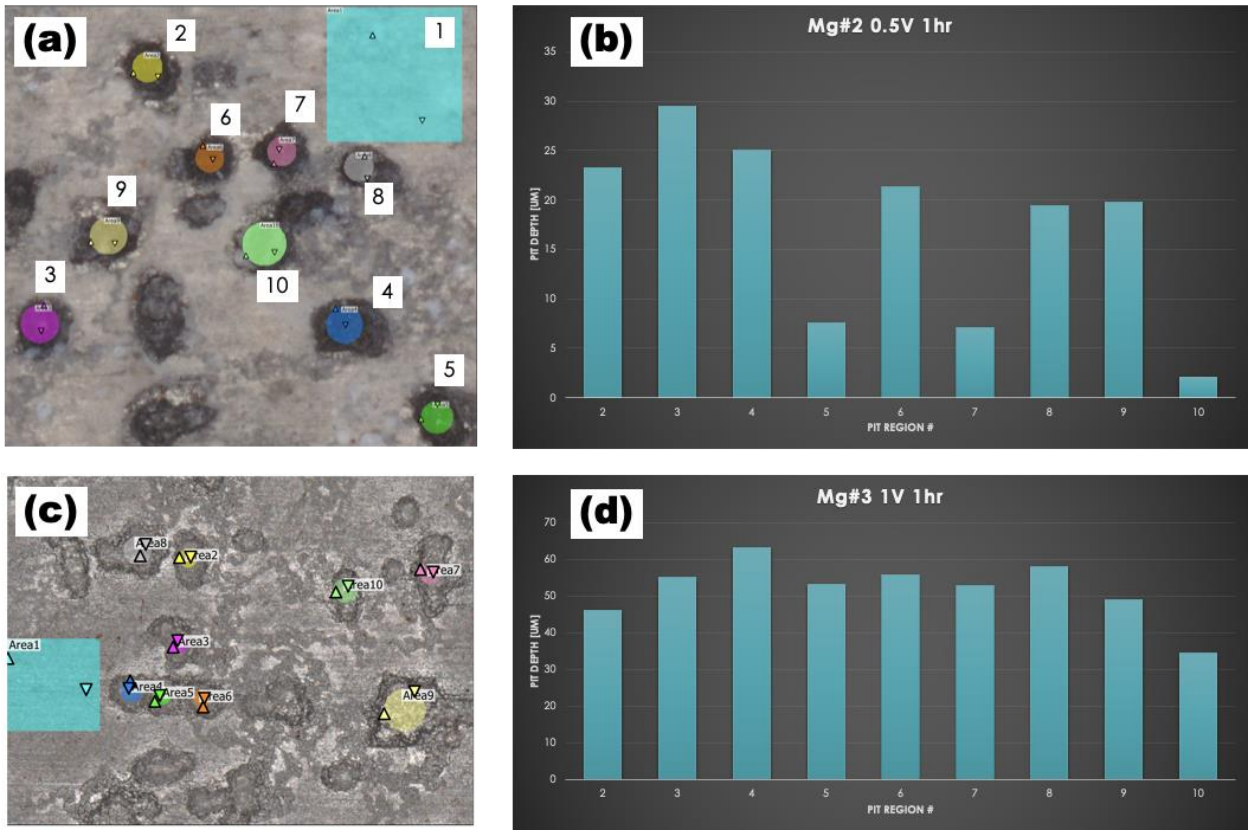

Figure 43 ***(a)*** *Manual selection of pit area on sample Mg at 0.5 V.* ***(b)*** *Histogram of quantitative pit depths measured from* ***(a)****.* ***(c)*** *Sample Mg at 1 V reference area (blue square) and pit areas 2-10.* ***(d)*** *Histogram of quantitative pit depths measured from* ***(c)****.*

Table 11 Al Pit Depth (μm)

Area #	0.5V	1V
2	2.2	0.9
3	2.1	2.5
4	1.1	1.2
5	1.9	1.1
6	1.8	2.6
7	1.2	0.3
8		2.0
9		0.8
Avg.	1.5	1.4
Std Dev	0.4	0.8

4.3 Mechanical Properties

4.3.1 Lap-Shear Tensile Tests

The peak strength of 6 groups of specimens was plotted in **Figure 44** and the averaged peak strength value were summarized in **Table 12**. It is very interesting to find out that the bond strength between Al and Mg was not reduced too much after eight weeks of corrosion, which means the corrosion media could not significantly affect the weld region as well as the bonding strength. This conclusion can also be supported by SEM/EDS Large Area Mapping from **Figure 45.** where there is not much oxidation amount (color in green) compared to the surrounding region.

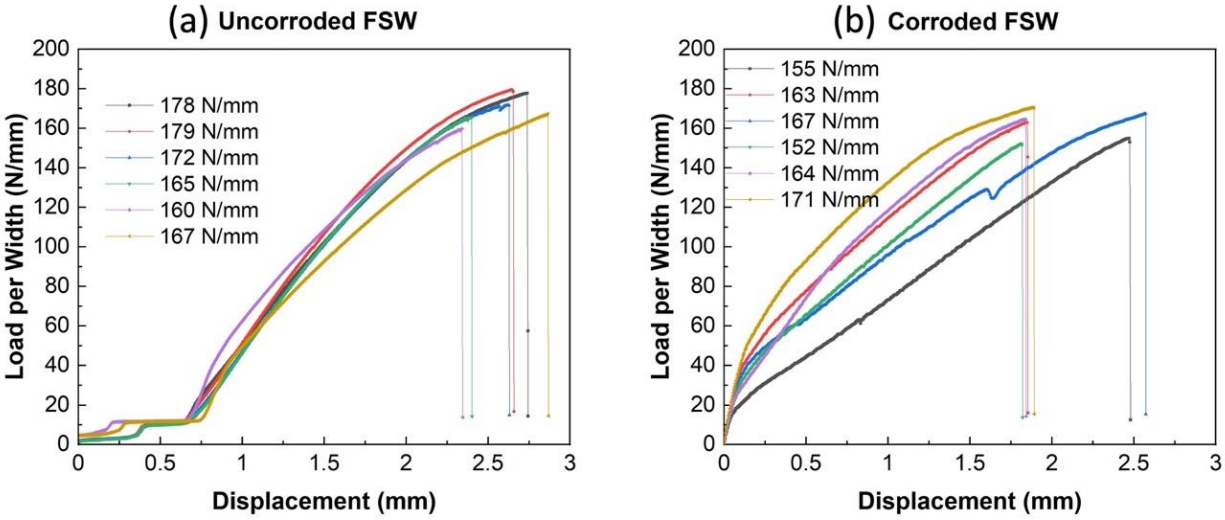

*Figure 44 Load-displacement curves of the FSW specimen: **(a)** Uncorroded; **(b)** corroded after eight weeks.*

Table 12 Summary of load-extension strength

	1	2	3	4	5	6	Average
fresh	178	179	172	165	160	167	**170**
8 weeks	155	163	167	152	164	171	**162**

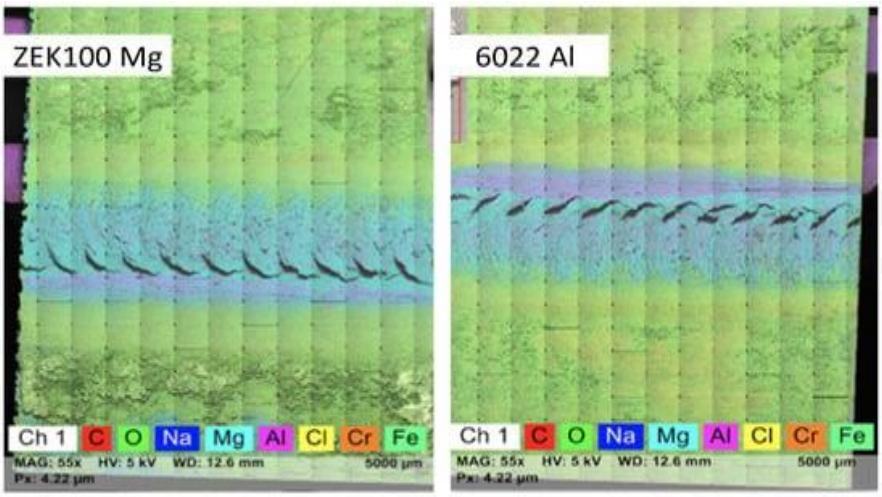

Figure 45 SEM/EDS LAM of 8 weeks corroded FSW Mg (left) Al (right) fractured weld.

4.3.2 Microindentation hardness tests

Figure 46(a) shows the averaged value of hardness distribution map obtained by microindentation tests. Different zones (e.g. nugget, HAZ, hardened, base) were roughly identified through MATLAB plotting in **Figure 46(b)**.

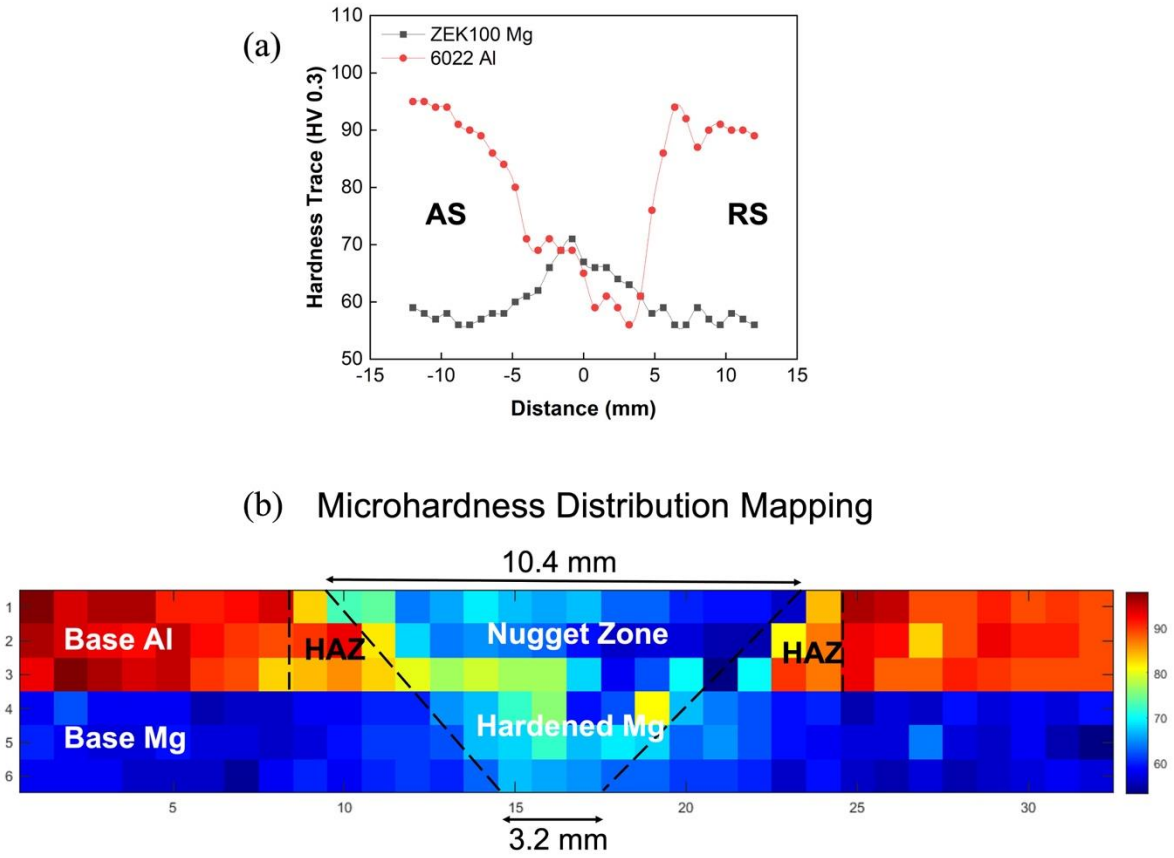

Figure 46 ***(a)*** *Hardness locations and values across the weld cross section sample;* ***(b)*** *Division of each FSLW zone through hardness distribution.*

This test plot encompasses base metal, HAZ (assumed) and weld zone. Cáceres [15] has reported that the hardness of castings is lower at the center due to a coarser microstructure of solidification and higher porosity concentration. The data reveals that hardness values for Al drop between points 66 and 150, which is around 9.0-9.8 mm from the top Al alloy. 6022 Al as a precipitation hardened aluminum alloy on the top side was showing a soften zone around the weld center, and it's suggested that its hardness profile is strongly depended on the hardened precipitation distribution

instead of grain size. This softening effect in the central weld zone is caused by dissolution and coarsening of the number of hardened precipitations [12]. This kind of grain refinement occurred in the top Al sheet because of the high temperature and plastic deformation. However, bottom ZEK100 Mg sheet on the other hand does not affect a lot by mechanical softening as well as dynamic recrystallization, will be more rely on the intermetallic as well as the grain size distribution according to Hall-Petch relationship. **Figure 47** indicates the change of grain size of bottom Mg from left to right: **(a)** base alloy contains amorphous and coarse grain size; **(b)** weld zone due to the heat effect and recrystallization would have the finest grains (~1 μm), therefore behaves the highest hardness.

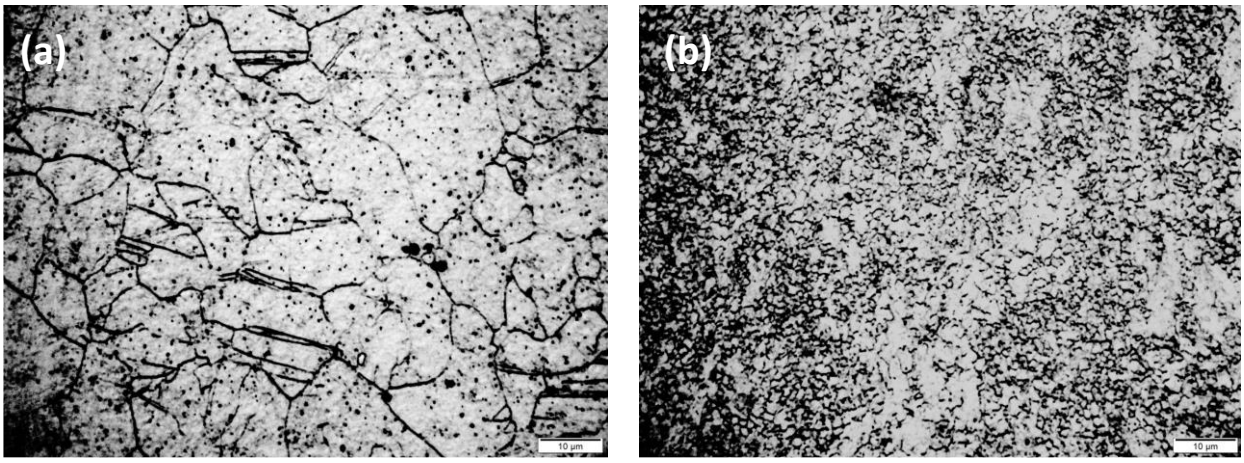

Figure 47 ZEK100 Mg after etching. ***(a)*** *Base metal;* ***(b)*** *Weld zone.*

4.3.3 Flat-Punch Nanoindentation for True Stress-Strain Curves

Indentation testing was performed to establish the stress-strain curves on corresponding zones according to the region divided from **Figure 46(b).** The true stress-strain curves on each region of the FSW specimen was showing a similar tendency compared to their hardness value. In comparison to base Al, Al Nuggets and Al HAZ exhibit lower strength, while hardened Mg exhibits higher stress than base Mg in **Figure 48.**

The interfacial regions of γ-$Al_{12}Mg_{17}$ and β-Al_3Mg_2 IMCs were analyzed using nanomechanical mapping, clustering analysis, and feature deconvolution techniques. The severely plastically deformed edge of the nugget zone was analyzed using a KLA Instruments iMicro nanoindenter, which allowed for the capturing of mechanical properties micrographs and large datasets with high-resolution positioning at a rate of 1 indent per second. A target load of 0.6 mN was applied, and a 100 um by 100 um regions with 10,000 nanoindentation data points was captured, as shown in Figure 49. The mechanical property map was imposed to scale upon a digital micrograph of the region prior to indentation testing. K-means clustering was applied to the dataset to identify the IMC layer specific hardness relative to the surrounding nugget zone matrix. The modulus of elasticity values versus hardness values for all 10,000 data points presented in Figure 49(a–c) were plotted as the y-axis and x-axis in Figure 49(d).

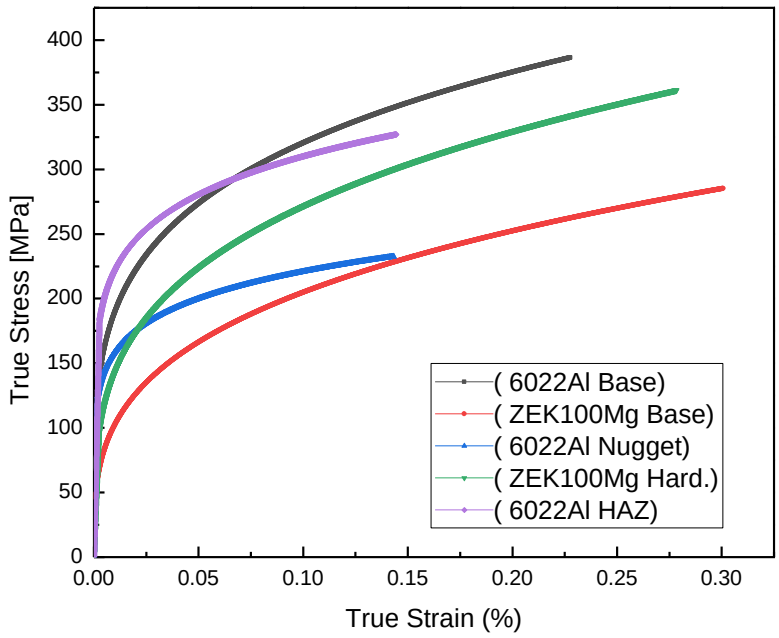

Figure 48 True Stress-Strain curves from nanoindentation testing.

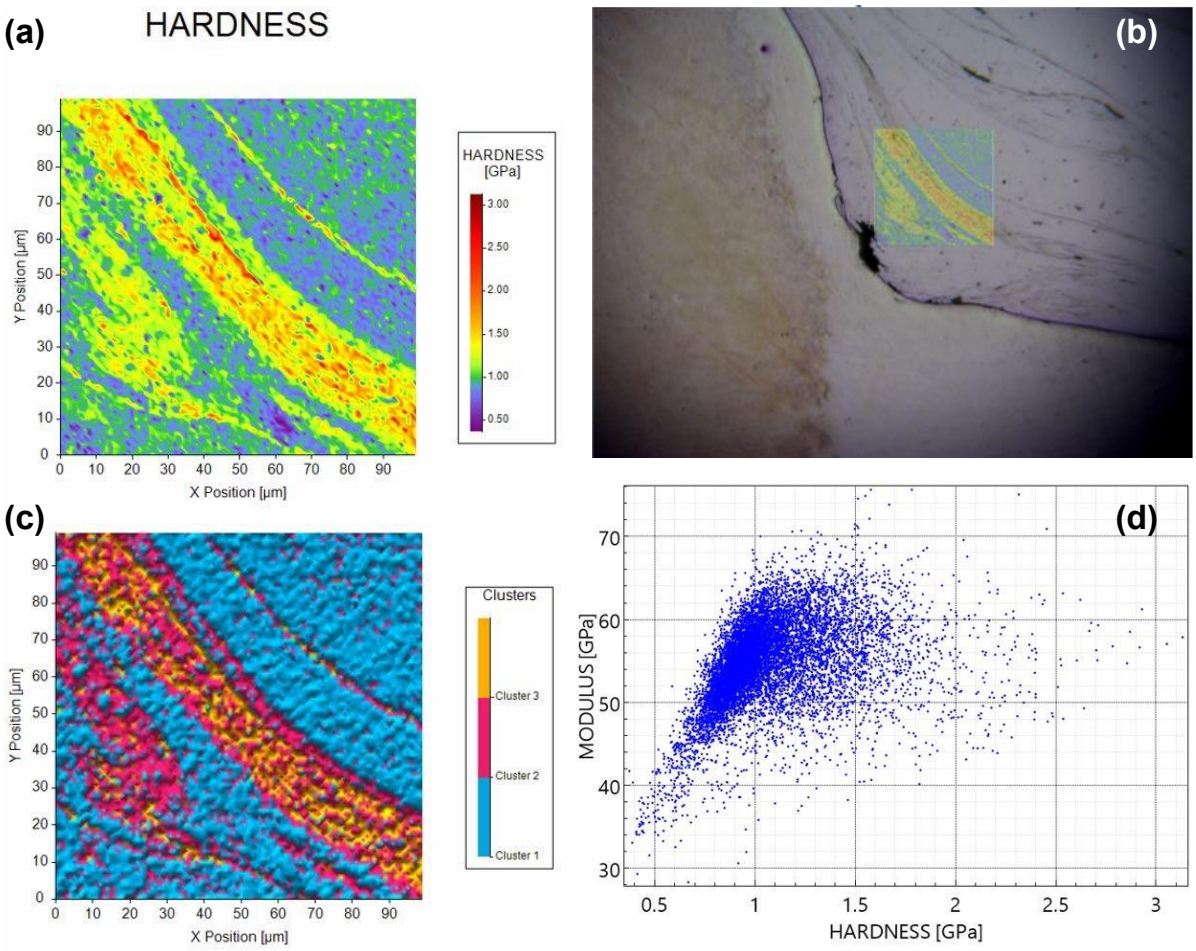

Figure 49 (a) Nanomechanical property map or contour plot wherein the range of values obtained are visually depicted using a color-coded legend for hardness values. (b) Imposition of (a) onto the region tested to obtain (a,c,d). (c) K-means clustering analyzed and replotted form of (a), wherein three centroids were assumed. (d) Modulus vs. hardness for each of the 10,000 data points underwriting the nanomechanical mapping-based analysis presented.

5. Adhesive-FSW Hybrid Joints

5.1 Adhesive-FSW Specimen Preparation

PNNL team created and evaluated lap joints using friction stir welding (FSW) between Mg and Al, with and without adhesive layers. As shown in **Figure 50**, the adhesive-FSW hybrid specimen

were conducted by applying the adhesive surrounding the welding area without affecting the welding properties. When the lap shear testing was conducted, there is no noteworthy variations were found between the FSW joints created with and without the adhesive layers, as illustrated in **Figure 51**.

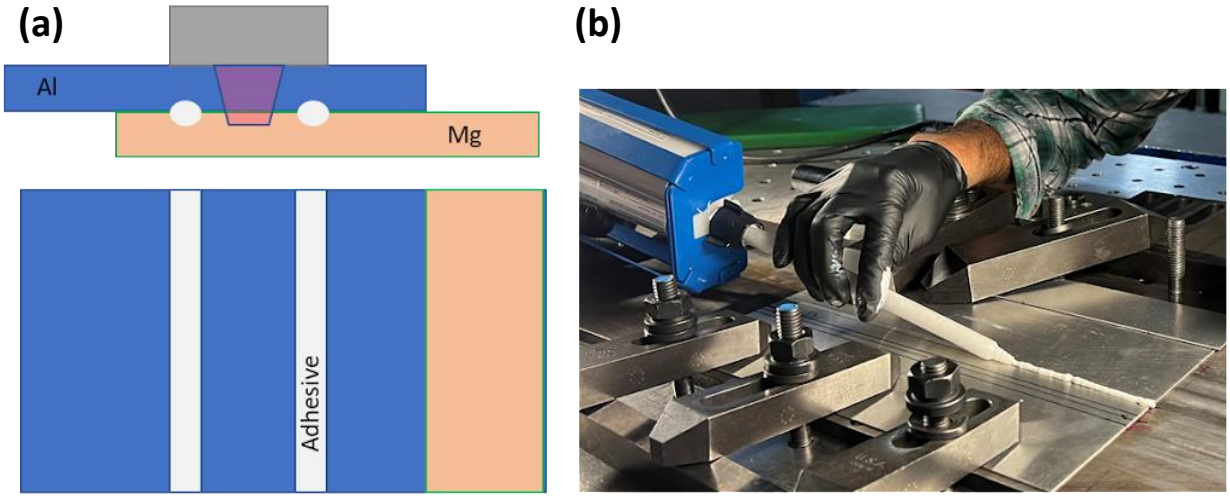

*Figure 50 Adhesive application in FSW panels: **(a)** Pictograph illustrating application of adhesives at Al-Mg interface prior to FSW; **(b)** adhesive bead being applied.*

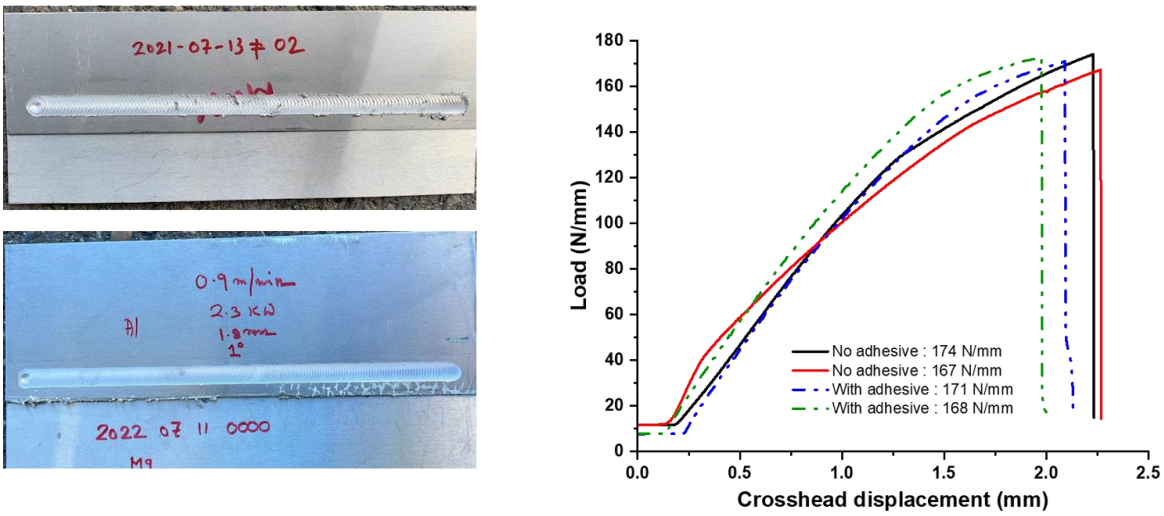

Figure 51 Lap shear test results with and without adhesives from FSW cut samples.

However, even the lap-shear strength does not indicate too much difference between FSW and Adhesive-FSW hybrid welds, it is still noticeable that the adhesives layer between top 6022 Al and bottom ZEK100 Mg is not perfectly continuous. There are gaps between the transition zone with (**Figure 52**) or without (**Figure 53**) polish treatment under optical microscope. These gaps may not significantly affect the lap-shear strength, but might be harmful on lowering corrosion resistance, which will be discussed in the corrosion section.

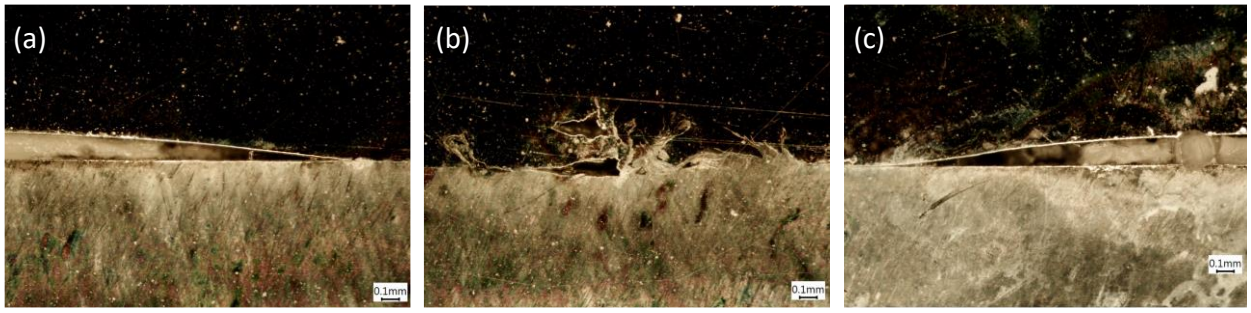

Figure 52 Optical microscopic images show discontinuously adhesive bonding between the transition region after polishing. ***(a)*** *advancing side (AS);* ***(b)*** *weld zone (WZ);* ***(c)*** *retreating side (RS).*

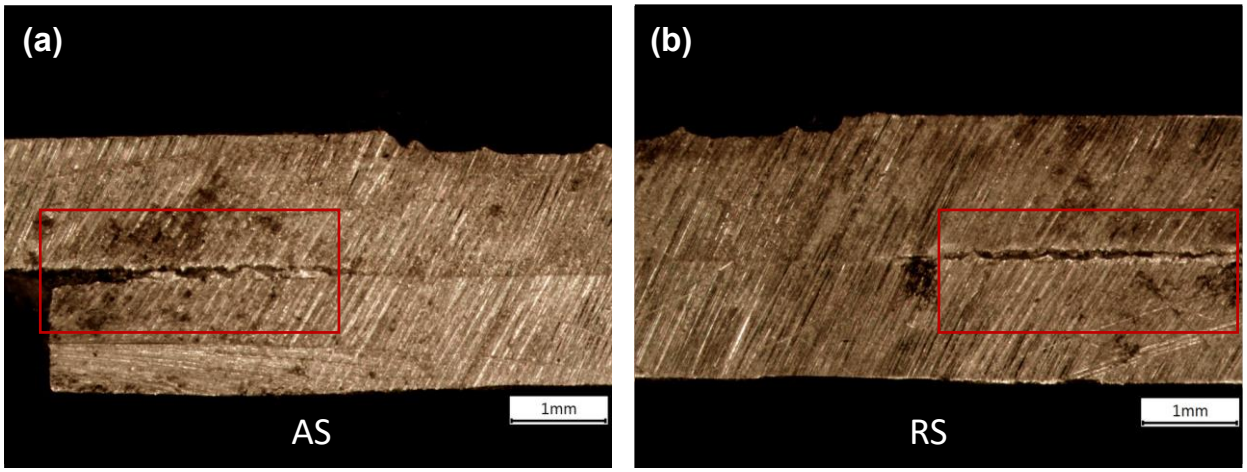

Figure 53 More optical microscopic images show discontinuously adhesive bonding between the transition region before polishing. ***(a)*** *advancing side (AS);* ***(b)*** *retreating side (RS).*

5.2 Fatigue Testing

5.2.1 Statistical analysis on fatigue testing

Figure 54 illustrated the fatigue testing results of FSW joints and Adhesive-FSW hybrid joints where the y axis stands for the applied load per width and x axis is the lifetime at which the material fractures. The red box in the area indicates that the data points have exceeded the maximum testing duration or load capacity, commonly referred to as "run-out" data. Based on the comparison shown here, it is evident that the fatigue performance of FSW joints with adhesive is superior to those without. At equivalent stress levels, most of the FSW joint with adhesive datapoints exhibit slightly longer lifetime, except for 40 N/mm. This observation suggests that the presence of adhesives provides additional bonding force that can assist in withstanding tension forces during fatigue testing. Further data points will be included to bolster this conclusion.

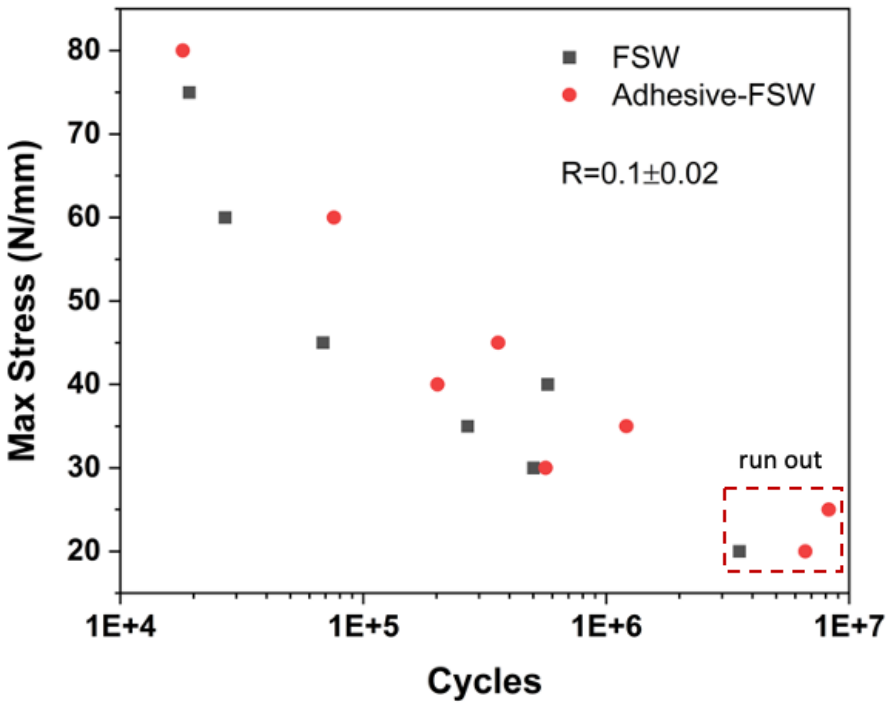

Figure 54 Fatigue testing results.

Figure 55 lists the statistical analysis on both (a) FSW and (b) Adhesive-FSW hybrid joints separately, where from right to left it illustrated that the possibility for the specimen to fail. Red and blue is 99% and 95% respectively, means extremely likely for the joints to get fractured at such conditions. Purple and yellow curve represents 5% and 1% correspondingly, which states that specimen could be able to survive at these regions. The averaged S-N curve (middle green line) shows that FSW joints with adhesive have a longer lifetime under identical testing conditions, likely due to the ability of the adhesives to absorb some of the plastic deformation. This difference is evident from the curve, which indicates that adhesives are effective in prolonging the fatigue life of FSW joints.

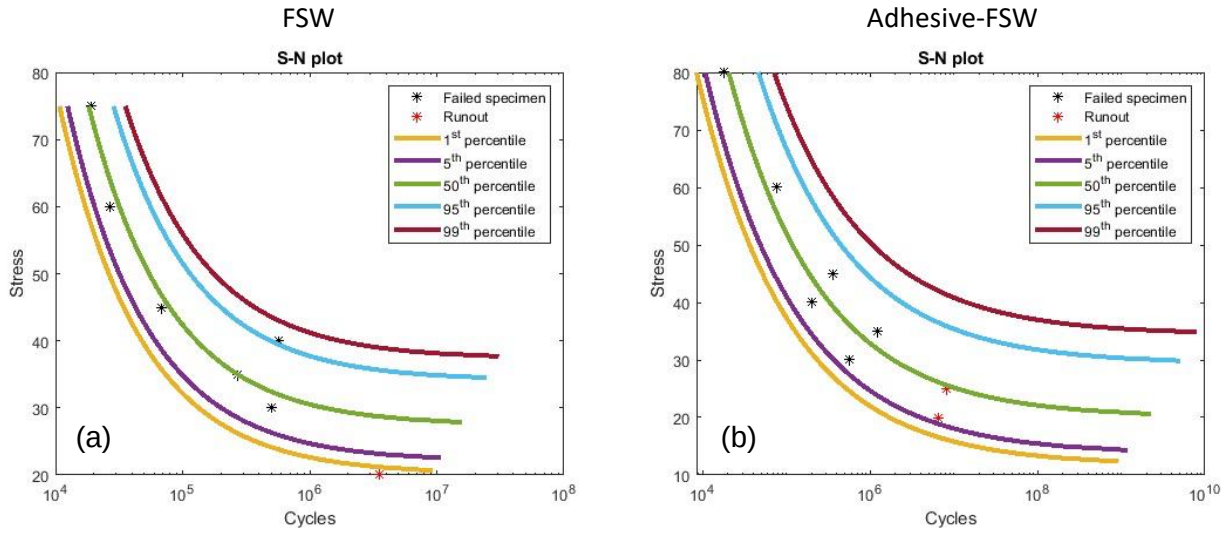

Figure 55 Statistical analysis on (a) FSW and (b) Adhesive-FSW hybrid joints.

5.2.2 Surface characterizations after fatigue testing

It should be clarified that there are two types of failure happened on these fatigue tests: break at the welding region and fracture on Mg side. For FSW specimen, most joints failed at the weld zone, as revealed in **Figure 56**. However, for Adhesive-FSW hybrid joints, most specimens are having cracks on Mg side which makes the failure happened on ZEK100 Mg, picture can be found in **Figure 57**.

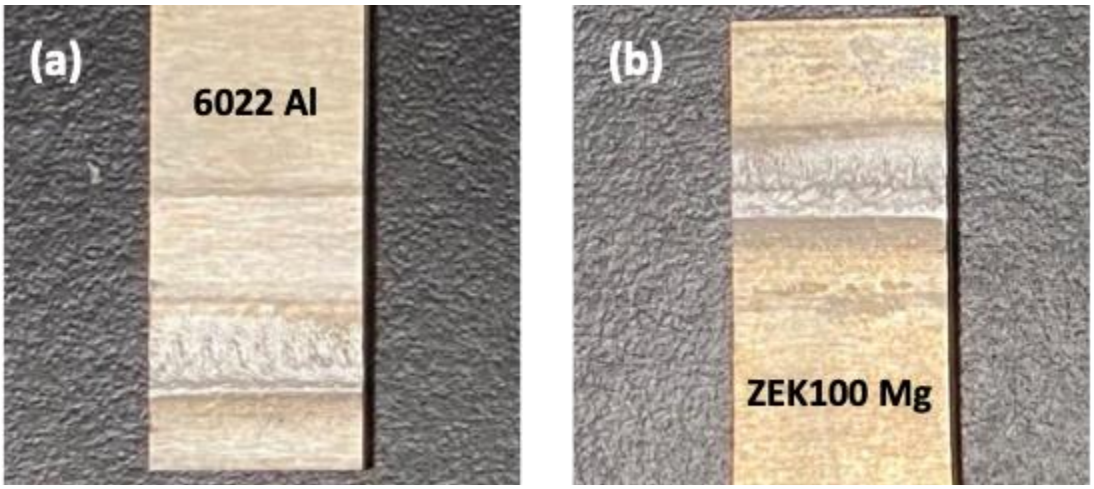

Figure 56 FSW weld failed after fatigue. ***(a)*** *Top 6022 Al;* ***(b)*** *Bottom ZEK100 Mg.*

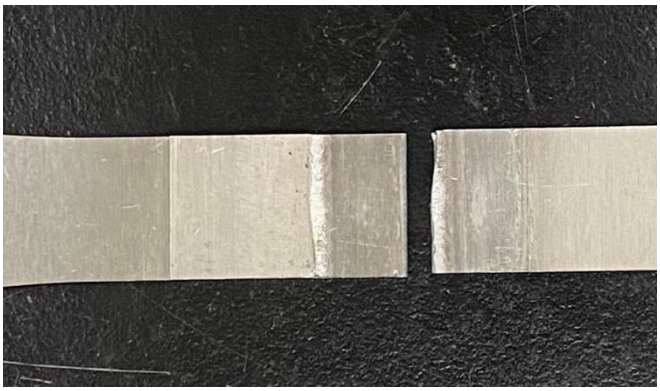

Figure 57 Adhesive-FSW joint failed on ZEK100 Mg after fatigue.

Another finding from the fatigue testing is that the typical indication for a fatigue failure that was called 'beach mark' was found in the retreating side in **Figure 58(c-d)**, which is not clearly shown in the advancing side **Figure 58(a-b)**. To compare the fatigue tests with 'fresh welded' samples, another lap-shear test (Cycle: 1) was conducted and the characterizations under optical microscope were shown in **Figure 59** where no obvious 'beach mark' was observed on both 6022 Al and ZEK100 Mg.

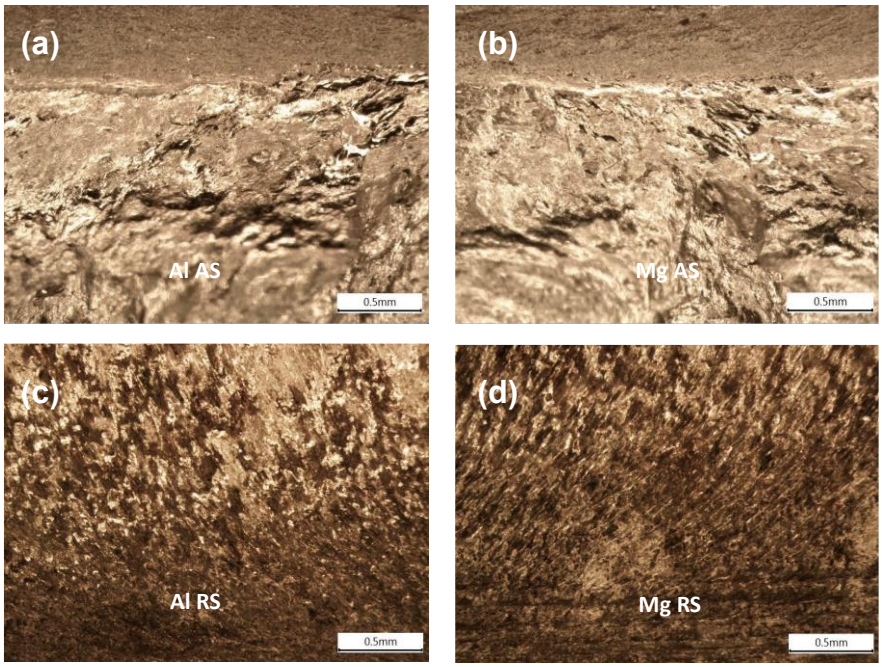

Figure 58 Fatigue Optical Microscopic pictures on FSW after fatigue (a) AS of lap-sheared 6022 Al; (b) AS of lap-sheared ZEK100 Mg; (c) RS of fatigue 6022 Al; (d) RS of fatigue ZEK100 Mg.

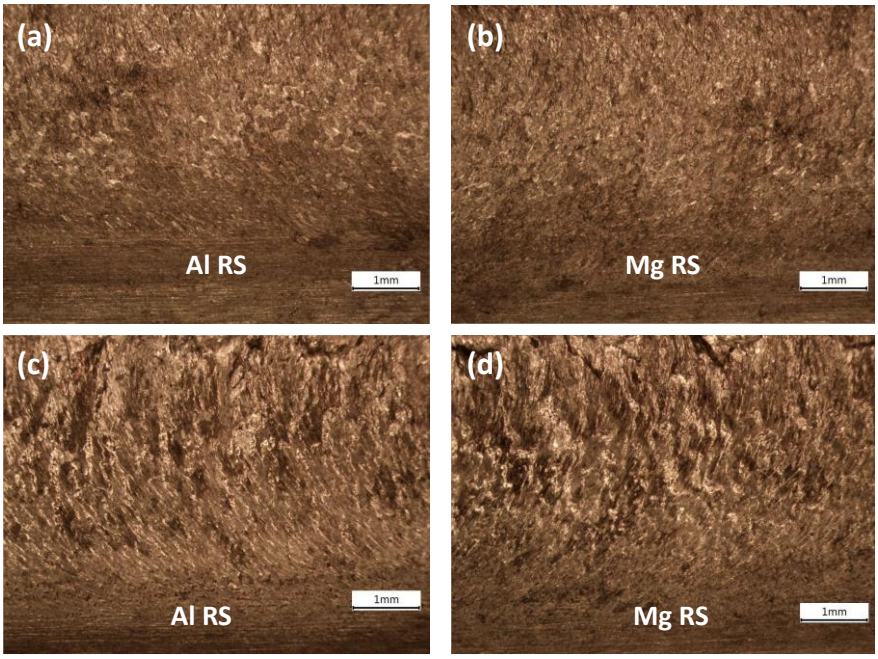

*Figure 59 FSW joint failed on weld zone after lap shear: **(a)** 6022 Al RS; **(b)** ZEK100 Mg RS. FSW joint failed on weld zone after fatigue: **(a)** 6022 Al RS; **(b)** ZEK100 Mg RS.*

As previously noted, many of the friction stir welded (FSW) joints failed at the overlapping welding area, particularly at the retreating side, where visible "beach marks" were observed. Upon closer examination using scanning electron microscopy (SEM), as illustrated in in **Figure 60**, both aluminum (Al) and magnesium (Mg) regions exhibited numerous tiny pits that could serve as sites of fatigue initiation. Adhesive-FSW, on the other hand, mostly failed on Mg base metal indicates that the crack initiated on Mg side earlier than the welding area as it exhibited in **Figure 61(a)** and **(c)**, where obvious cracks can be traced.

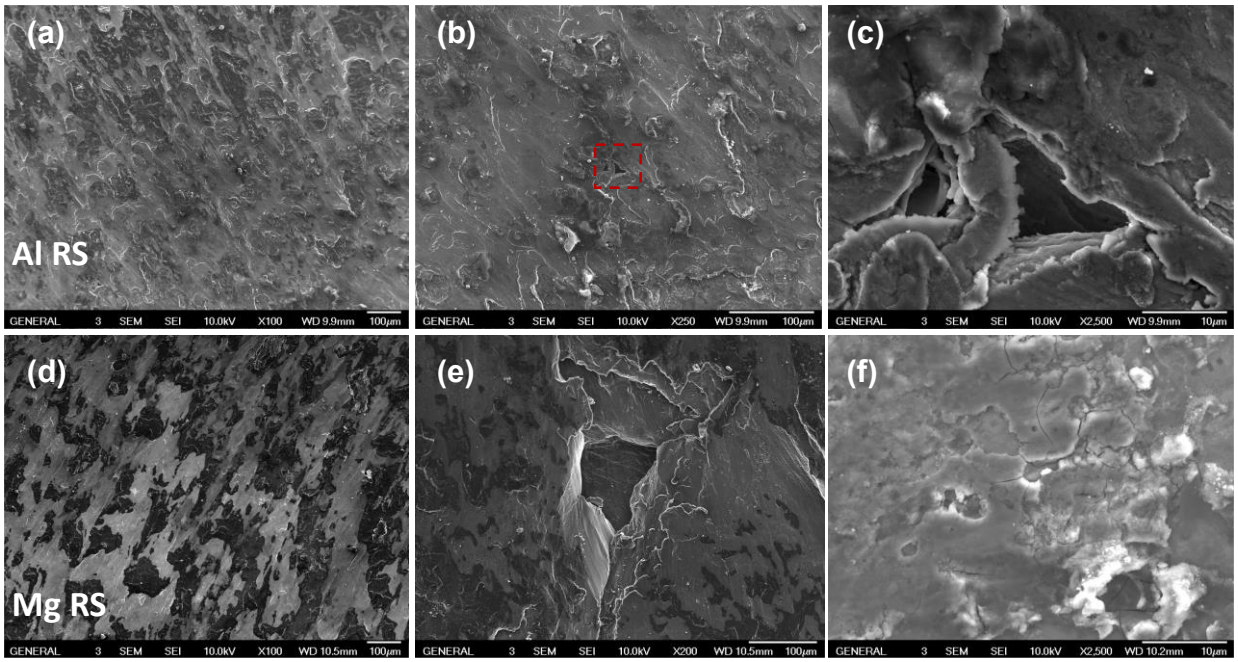

Figure 60 SEM images on (a) FSW 6022 Al RS; (b) Potential fatigue cracking initiation site on FSW 6022 Al; (c) Higher magnification of (b); (d) FSW ZEK100 Mg RS; (e) Fatigue cracking initiation site on ZEK100 Mg; (f) Higher magnification of the Mg fractured surface.

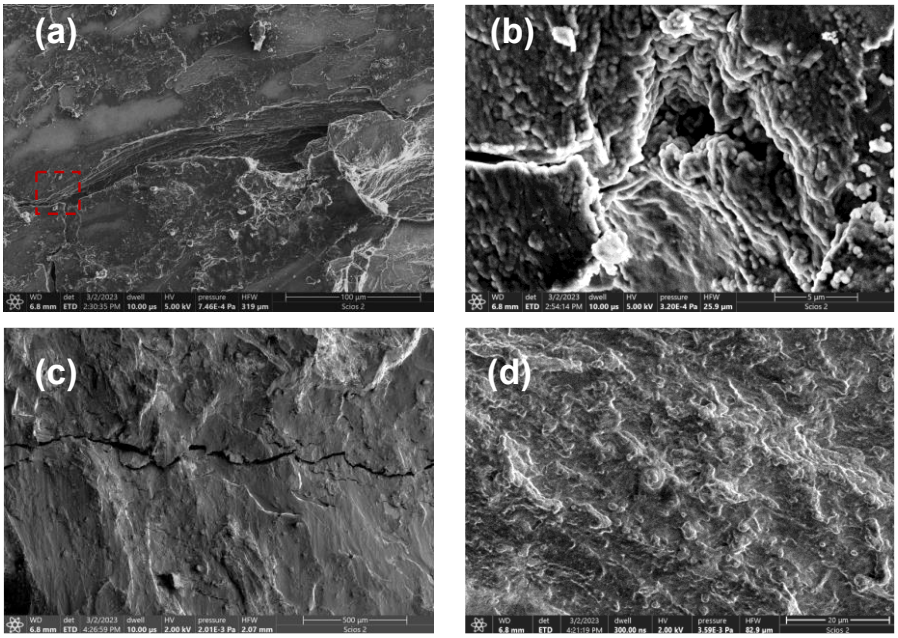

Figure 61 SEM images on Adhesive-FSW hybrid joints. (a) Fatigue cracking initiation site on 6022 Al; (b) Higher magnification of (a); (c) Crack propagated from ZEK100 Mg edge; (d) Higher magnification of the fractured surface on ZEK100 Mg RS.

5.3 Corrosion behavior of Adhesive-FSW hybrid joints

Cyclic corrosion testing is also conducted on Adhesive-FSW welds in order to compare with FSW joints to investigate the corrosion property after being applied with adhesive. **Figure 62(a)** contains the testing results showing that at early stage, 2 weeks and 4 weeks, joints with adhesive (S-2, S-8, S-3, S-5) are having clearly higher corrosion rate than pure FSW (S-6, S-9). 6 weeks and 8 weeks did not show much difference between FSW and adhesive-FSW on corrosion aspect. **Figure 62(b)** took the averaged corrosion rate value from the total 8 weeks and it can be found that welding joints with adhesive corroded faster than joints without adhesive.

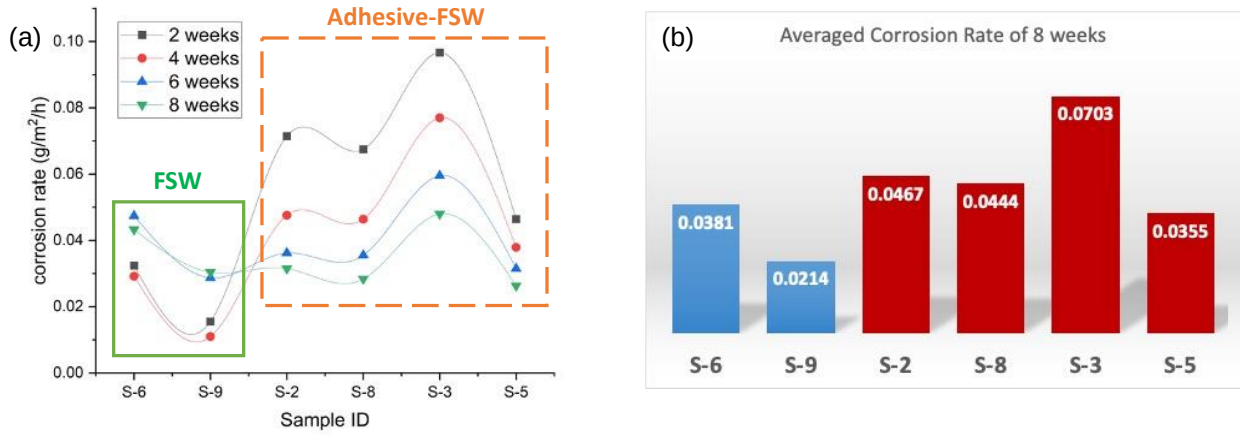

Figure 62 Corrosion rate calculated by weight loss on (a) FSW (S-6, S-9), Adhesive-FSW (S-2, S-8, S-3, S-5); (b) Averaged corrosion rate after 8 weeks of CCT.

To investigate the corrosion behavior of the Adhesive-FSW hybird joints, a polished specimen was prepared and subsequently immersed in a 3.5% NaCl solution for a period of one hour. Scanning electron microscopy (SEM) was employed to examine the results, revealing conspicuous signs of severe corrosion on the magnesium (Mg) side in the discontinuous bonding region, as seen in both advancing and retreating sides (AS and RS) in **Figure 63**.

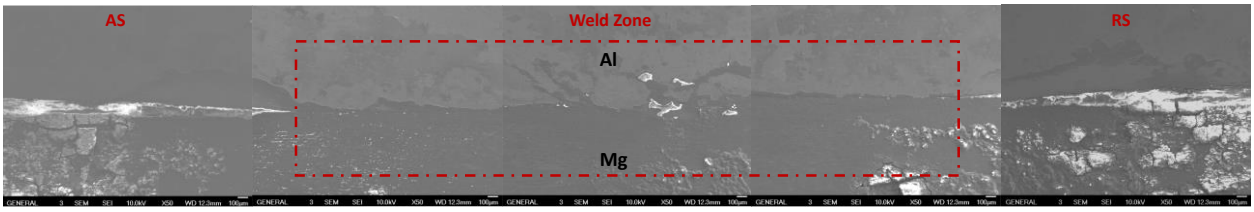

Figure 63 SEM picture of the post-CCT testing on the Adhesive-FSW specimen showing corrosion happened severely on the discontinuoues bonding region, both on AS and RS.

Surprisingly, the results indicate that the adhesive layer does not effectively mitigate galvanic corrosion by isolating the two dissimilar alloys. On the contrary, due to the presence of a discontinuous adhesive bonding between aluminum (Al) and magnesium (Mg), as revealed in **Figure 52** and **Figure 53**, the galvanic corrosion process is accelerated owing to the smaller anode-to-cathode area ratio.

Chapter 4: Future Work Suggestions

1. Investigation of micro galvanic corrosion

Current results mainly focus on the property of the two base alloys as well as the whole welding areas. However, the corrosion property of the welding center individually includes nugget zone, HAZ, TMAZ has not been fully studied, so does the corrosion mechanisms. In the future, it is suggested that the corrosion behavior of different zones as well as the intermetallic layers, secondary phase particles should be investigated under the micro level by Scanning Vibrating Electrode Technique (SVET) to provide the current density mapping in order to observe if there could be any potential difference between the individual area.

Bastos et al. [70] provided a great and straightforward example on the application of studying galvanic corrosion behavior of a mild steel corroded in 0.05M NaCl through SVET. As shown in **Figure 64**, where blue color means negative (cathodic) currents which associated with the reduction of dissolved $O_{2,}$ and red color means positive (anodic) currents, which are related to the iron oxidation. Similarly, SVET could also be applied on studying the current density distribution on tracking the corrosion behavior of FSW Al-Mg specimen. It could be clearly to indicate the potential heterogeneity on different zones as well as tracking the corrosion property of thinner intermetallic layers.

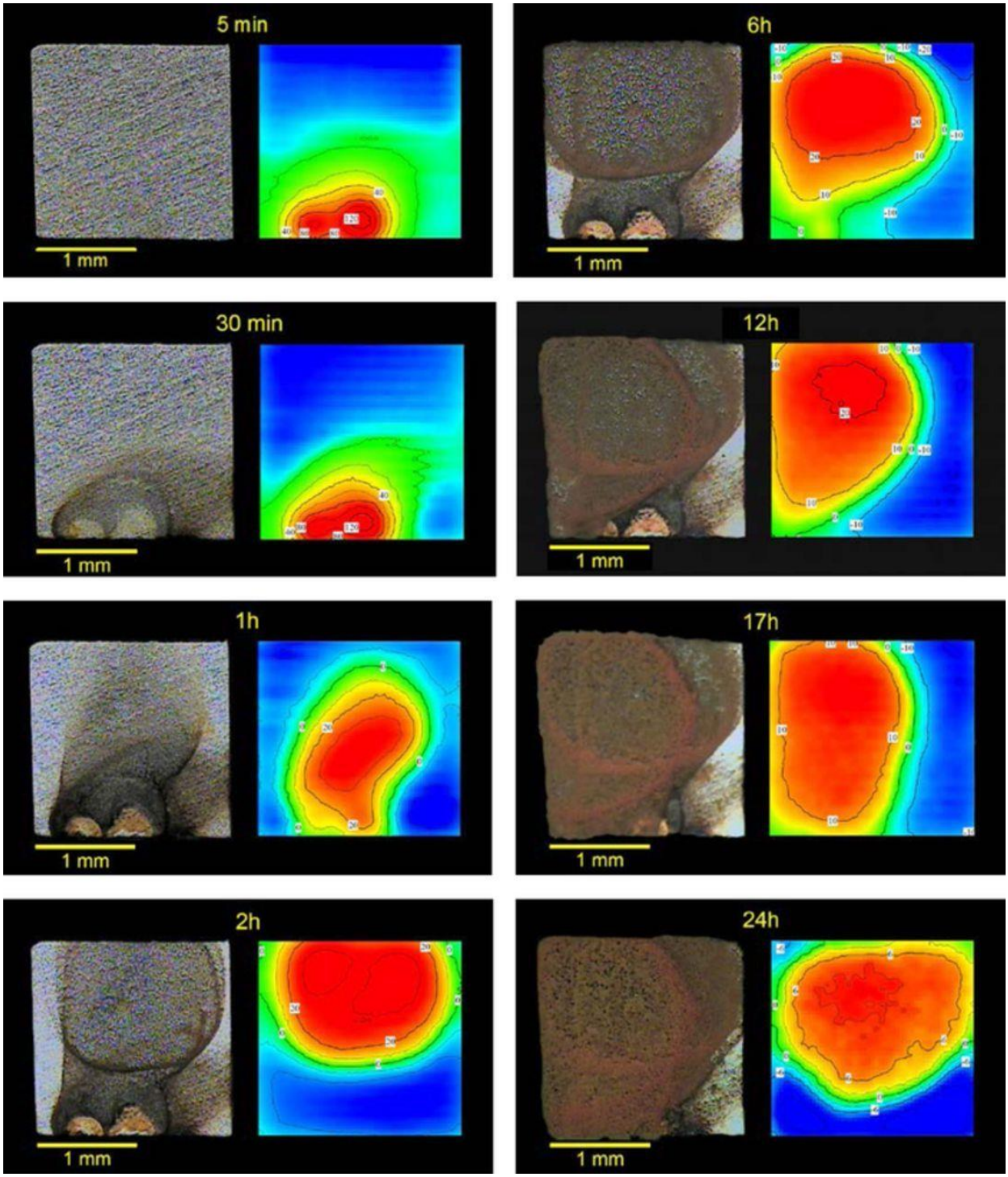

Figure 64 Stages of corrosion of a mild steel during the first 24 hours of immersion in 0.05 M NaCl. (Current density in μA/cm^2)

Cano et al [71] reported that Scanning vibrating electrode technique (SVET) measurements showed the filament-like corrosion on AM30B Mg alloy (**Figure 65**) consisted of an intensely anodic propagation front supported by a cathodically-activated filament behind, which was detected by TEM with focused-ion-beam (FIB) milling indicated that the cathodic activity was likely a combined result of the formation of MgO film and Al-Mn intermetallic particles to catalyze the cathodic H_2 gas evolution reaction.

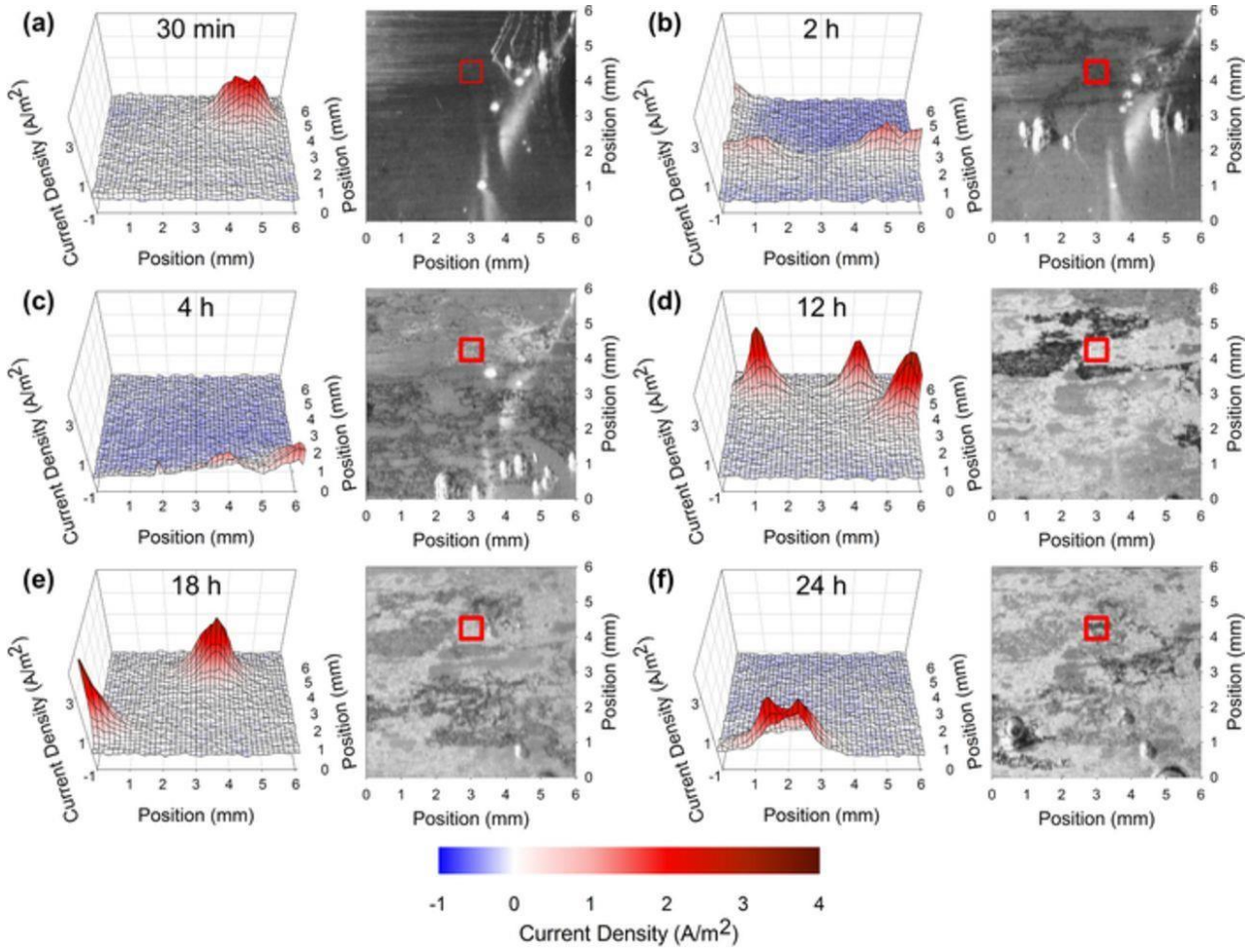

Figure 65 SVET plots and scan area images of the working surface taken at various times after immersion at the OCP in 0.05 M NaCl.

An immersion corrosion experiment was conducted in Oak Ridge National Lab which could aid future studies on the mechanism of ZEK100 Mg surface failure. **Figure 66(a)** depicts a SEM image of a FSW Mg-Al joint after 1hr immersion in 0.1M NaCl salt solution, with the half right side covered by tape for comparison purposes. **Figure 66(b)** illustrates that the corrosion product morphology varies across the interface from ZEK100 to the 6022 materials, possibly indicating a gradient in elemental composition, grain size, or a combination of both. **Figure 66(c)** is the atomic number contrast image of the Mg corrosion product at the interface, which suggests that the corrosion product has a lower average atomic number in the filamentous regions, possibly due to higher oxygen content. **Figure 66(d)** reveals that the filamentous corrosion is thicker than the surrounding conformal corrosion film that resides between the filaments. **Figure 66(e)** displays cracks present in the filaments, along with a lower average atomic number.

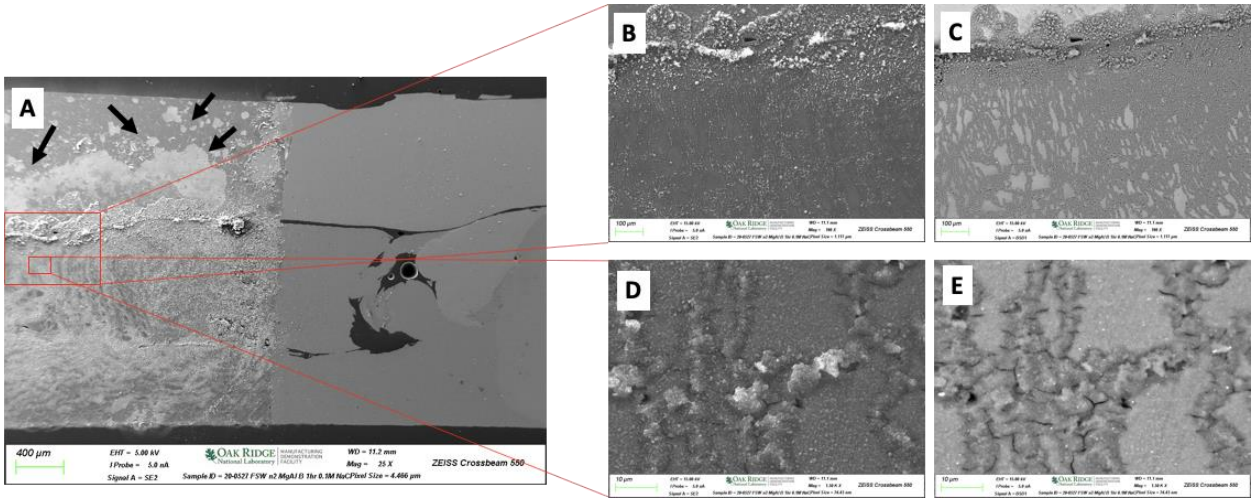

Figure 66 (a) SEM micrographs of FSW Mg-Al joint after 1hr immersion in 0.1M NaCl (left). (b) Topography of the Mg corrosion product at the interface. (c) Atomic number contrast of the Mg corrosion product at the interface. (d) Filamentous corrosion is thicker than the surrounding conformal corrosion film that resides between the filaments. (e) Cracks present in the filaments as well as a lower average atomic number.

Based on the current findings from Oak Ridge, in order to comprehensively understand the occurrence of filament failure, as well as other types of corrosion such as large pits and cracks,

further experiments combining SVET are necessary. These experiments will focus on different regions of ZEK100 Mg, ranging from the interface to 6022 Al, to gain a better understanding of the various types of corrosion that occur.

Furthermore, Jayaraj et al. [72] reported the corrosion property of the weld zone between 6061 and AZ31B joint by potentiodynamic polarization curves in NaCl solution. It is found that the corrosion rate in stir zone increases with higher acidities and Cl^- concentrations, the corrosion rate will decrease with the immersion time processes. Sunil et al. [73] concluded that the mixing stir zone suffered severe corrosion compared to base Al alloy and Mg alloy. This might be due to the galvanic coupling effect between base material and stir zone which behaves as a new material and has different corrosion potential compared to the two base alloys, this result also backed up the findings in this report. Ralston et al. [74] provided the relationship of grain size and corrosion rate. Grain boundary is usually considered having different properties than bulk material in terms of atomic coordination, reactivity, and diffusion rates. Material with higher grain boundary densities could have different electrochemical behavior with coarser grains which have lower grain boundary densities. In the future work, it is suggested that the relationship between corrosion rate and grain size can be investigated by immersing specimen into salt solution and provide 3D images before and after corrosion.

To summarize, investigating micro-galvanic corrosion through techniques such as SVET, as well as examining factors like grain size and grain boundaries, can provide insights into the behavior of Al-Mg FSW bimetallic joints. These future research directions can lead to a better understanding of the joints, facilitating the development of better materials and joining techniques for lightweight industries.

2. Corrosion and Mechanical Simulations

Friction Stir Welding has emerged as a popular solid-state welding technique in recent years. Despite its experimental success, there is still a need for a deeper understanding of the complex physical phenomena occurring during the FSW process. One approach to gain a deeper insight into the underlying mechanisms is through computational modeling. Phase field modeling has emerged as a powerful tool to study the microstructure evolution during the FSW process. For example, the formation of the intermetallic layers between 6022 Al and ZEK100 Mg during diffusion bonding process as shown in **Figure 67**. This approach allows researchers to investigate the interaction between multiple physical phenomena, such as heat transfer, material flow, and phase transformation, that occur at the microscale level. Phase field modeling can provide a detailed understanding of the microstructure evolution and its impact on the mechanical properties of the welded joints. In this way, this approach has the potential to contribute to the optimization of FSW processes, improving the quality and reliability of welded joints.

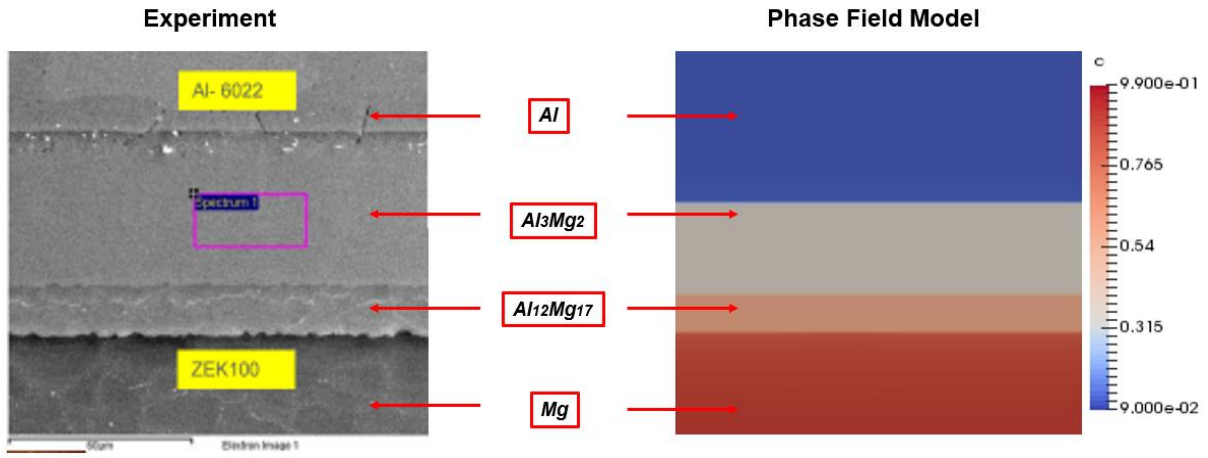

Figure 67 Comparison of SEM micrograph of the diffusion bond layer between 6022 Al and ZEK 100 Mg (left) and phase field model of pure Al-Mg interdiffusion right).

Phase field modeling can be used to study the corrosion behavior of FSW Al-Mg by simulating the electrochemical reactions that occur at the interface between the Al-Mg alloy and the

environment (electrolyte) in which it is exposed. The findings depicted in **Figure 68** indicate that under conditions of high dissolved oxygen concentration in the electrolyte, a passivation layer of $Mg(OH)_2$ grows. Furthermore, the domain exhibited a lower electric potential on the magnesium side and a higher potential on the aluminum side, which suggests that the aluminum is being galvanically protected, as expected.

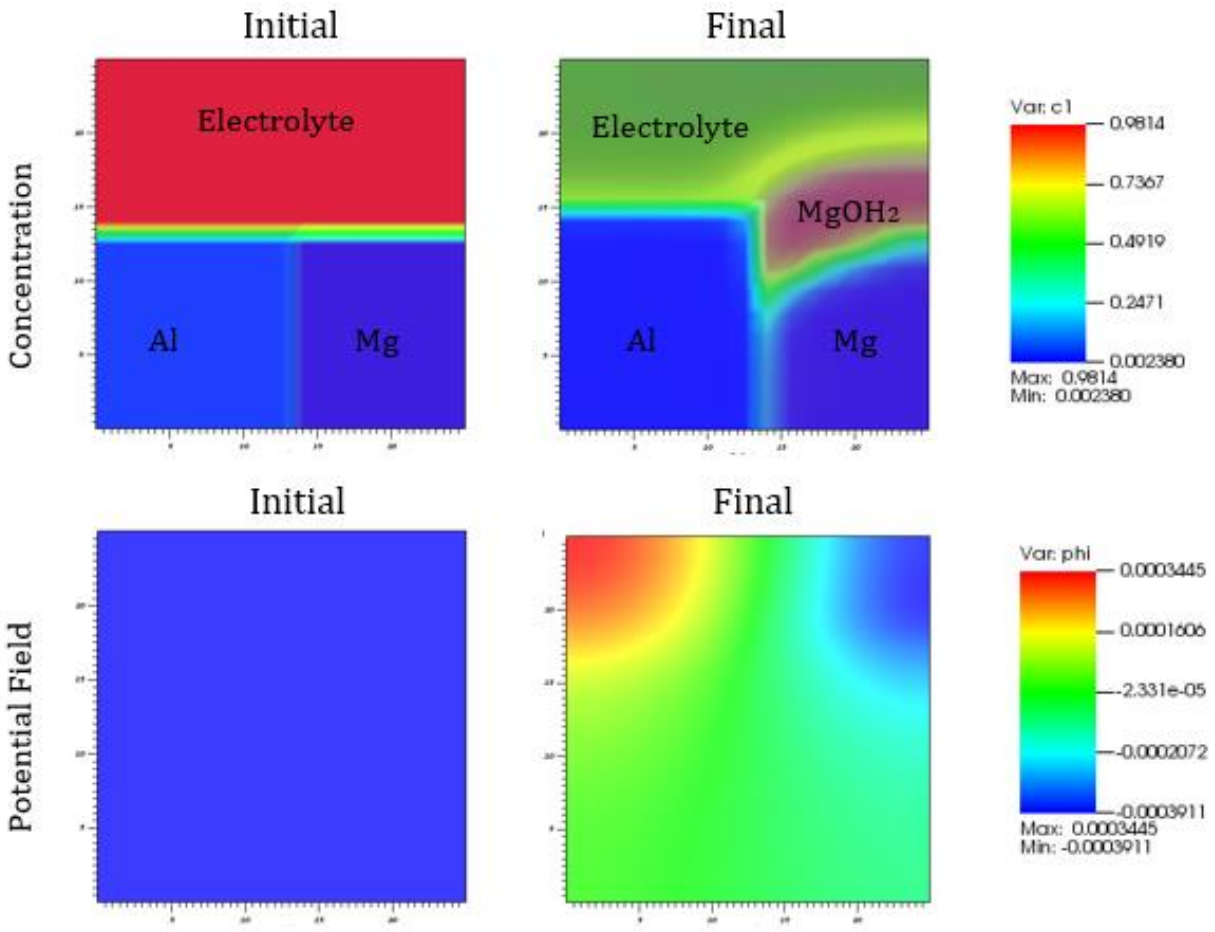

Figure 68 Output of the model with initial conditions representing galvanic corrosion: initial (left) and final (right) plots of composition (top) and electric potential (bottom).

Finite element modeling (FEM) is a powerful tool that has been increasingly utilized to study and optimize the process of friction stir welding. FEM has been successfully applied to a wide range of FSW applications, it involves dividing the joint into small, interconnected elements and using

mathematical equations to calculate the stresses and strains within each element. By applying FEM to FSW Al-Mg joints, it will be easier to analyze the stress distribution at the interface and identify potential areas of high stress that may lead to failure or corrosion. This information can then be used to optimize the welding process and joint design, leading to improved performance and durability.

For mechanical simulation, finite element modeling is widely being used to simulate and analyze the stress distribution at the interface of FSW Al-Mg joints, as displayed in **Figure 69**, which represents the evolution of stress distribution over the weld area of uncorroded 6022 Al - ZEK100 Mg joints with time, and the deformed geometry of the weld at the peak load. The load-displacement predictions obtained from the uncorroded and corroded samples were compared to the experimental measurements, and a high level of agreement was observed for the peak load and maximum extension, as demonstrated in **Figure 70**.

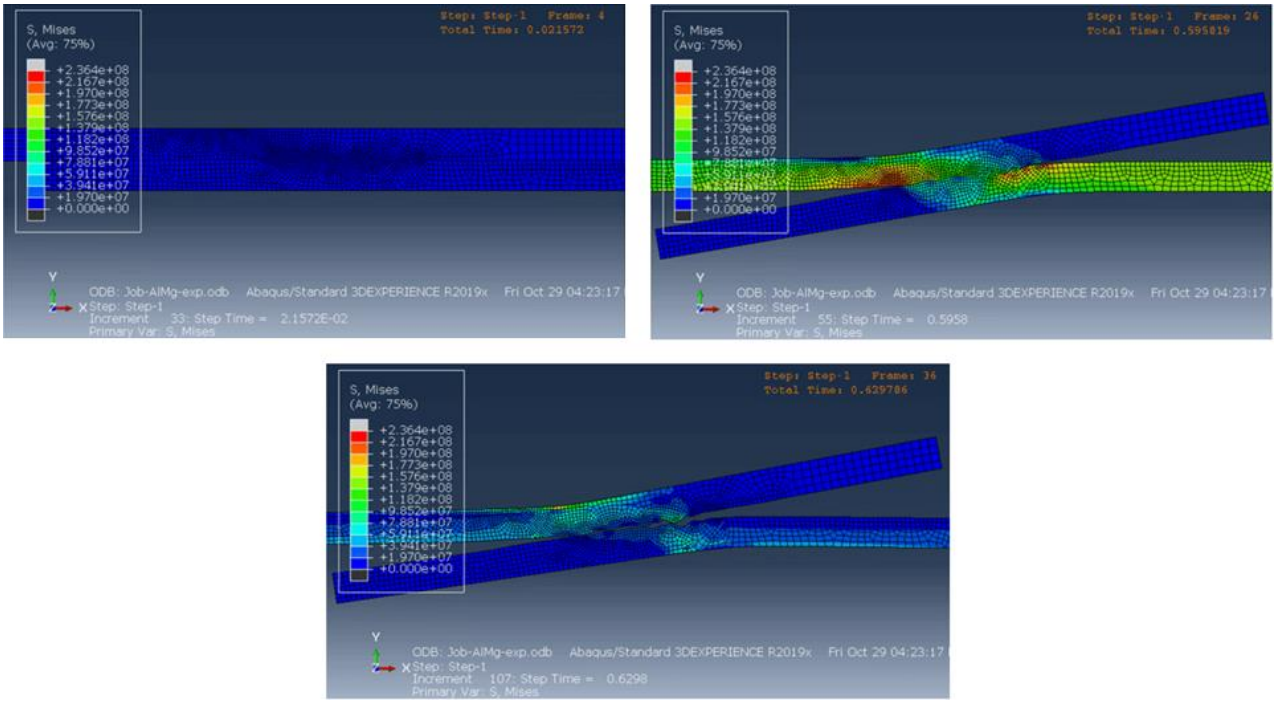

Figure 69 Stress distribution over the weld area of 6022 Al - ZEK 100 joints, and the deformed geometry of the weld at the peak load.

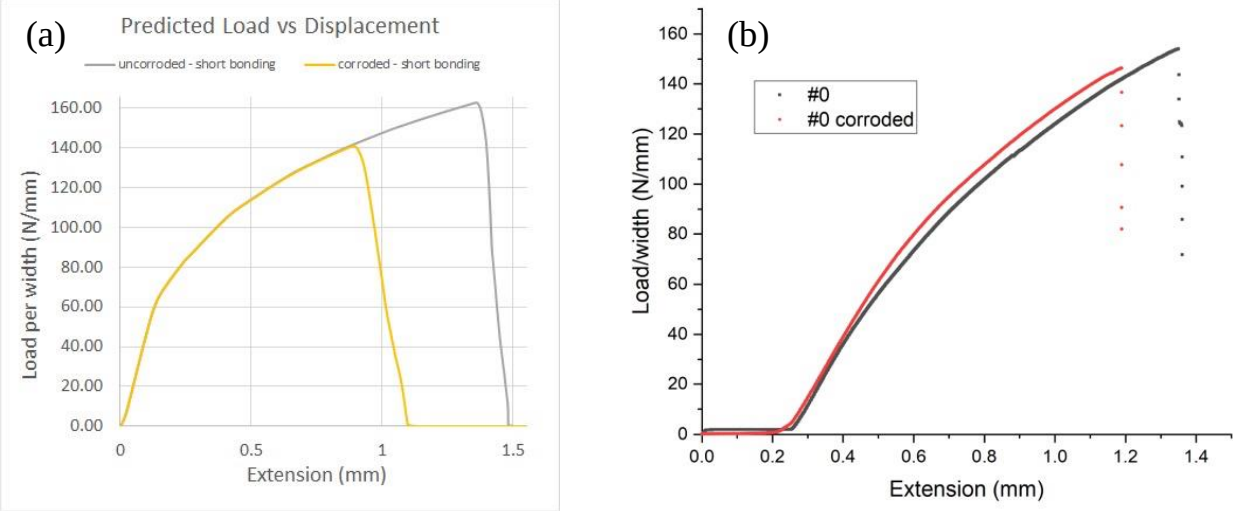

Figure 70 Load- Displacement Curves: (a) Modeling predicted; (b) Experimental result.

To summarize, the following are the suggested components for future research:

1) The use of SVET in FSW studies allows for the characterization of micro-galvanic corrosion on different area of the welding zone and its effects on joint performance.

2) Study on the mechanisms of grain size, grain structure effect on FSW could also be important for understanding the fundamental mechanisms of corrosion in Al-Mg FSW joints and developing effective corrosion mitigation strategies in the future.

3) Phase field modeling is a powerful tool for investigating complex physical phenomena, including corrosion, at the micro- and nanoscale. In the context of friction stir welding (FSW) of Al-Mg alloys, phase field modeling has been used to simulate the formation and evolution of corrosion pits and cracks, and to study the effect of microstructure, grain size, and other material parameters on corrosion behavior. By providing detailed insights into the underlying mechanisms of corrosion, phase field modeling can aid in the design and development of more corrosion-resistant alloys and coatings for FSW applications for future applications.

4) The use of FEM in FSW Al-Mg research has increased in recent years due to its ability to provide insight into the complex interactions between the tool, workpiece, and process parameters. For future researchers, by simulating the welding process, FEM can help to optimize process parameters such as tool geometry, rotational speed, and traverse speed, to achieve desired weld quality and mechanical properties. It can also be used to study the effect of defects and microstructural features on the mechanical behavior of FSW joints, enabling the development of high-performance lightweight materials for aerospace and automotive applications.

Chapter 5: Summary

The final aim of this project is to develop and validate a predictive model for the corrosion and mechanical failure of friction stir welded (FSW) aluminum-magnesium (Al-Mg) alloy joints, with the goal of creating lightweight materials for vehicle door hems that can enhance fuel efficiency and promote sustainability. Therefore, this study focuses primarily on investigating the microstructural, corrosion, and mechanical properties of FSW Al-Mg bimetallic joints experimentally, without any form of protection to provide valid experimental data as well as parameters for the industrial and modeling research. The current findings suggest that:

The electrochemical results reveal that the corrosion behavior of the joint is strongly affected by the galvanic corrosion effect. Both electrochemical tests and SEM observations confirm that Mg has a significantly higher corrosion rate than Al, and thus acts as the anode during galvanic corrosion due to its lower corrosion potential. For the intermixing welding area where can be interpreted as the thin intermetallic formed, it surprisingly behaves differently with both base Al and base Mg. The corrosion potential of the WZ materials sits very adjacent to ZEK100 Mg, while the current density which represents the corrosion rate is higher than both base Al and base Mg which has been confirmed by potentiodynamic scan as well as EIS fitted data as corrosion resistance.

Cyclic corrosion testing provides the biweekly corrosion rate through weight loss measurement; it is showing that the corrosion rate reduces with time, could be the effect of passivation. And a larger cathode can lower the corrosion resistance to some extent, which can be advised on designing the welding parts. For the CCT experiment on FSW and Adhesive-FSW joints, it is surprisingly showing that specimens with adhesive layers are having higher corrosion rate which indicates that the adhesive layer could not be able to isolate the two alloys perfectly, on the contrary, the porous and discontinuous layer provided extra ‘bridges’ to connect the two alloys and accelerate the galvanic corrosion in the CCT chamber. It is suggested for using glass beads while

applying for the adhesive layer to make sure the alloys will not be moved during the friction stir process and have a much uniform distribution between the two alloys for the future researchers.

For the investigation of mechanical properties, lap shear strength measurements were conducted before and after corrosion tests. The results indicate that there were no significant change in the lap shear strength, indicating good resistance of the bonding hook against corrosion as a bulk specimen in the corrosion chamber. Lap shear testing was also conducted on FSW and Adhesive-FSW joints each individually and the results suggest that adding the plastic adhesive layer could not help to improve the peak load under a lap shear measurement.

Microindentation and nanoindentation tests were conducted to analyze the hardness and true stress strain curves of the cross-sectional FSW Al-Mg weld. It was noticed that top 6022 Al exhibited the lowest hardness and true stress value in the nugget zone, which is because of the heat generated through the friction process which enabled materials to experience the dynamic recrystallization process and made the hardened particles dissolved. Whereas the bottom ZEK100 Mg has the highest hardness and true stress value in the center weld zone due to the finest grain size that can be understood by Hall-Petch equation.

However, despite the fact that the adhesive layer does not appear to enhance the corrosion resistance or lap shear strength of the joint, it is capable of absorbing some of the fatigue loading during low cycle fatigue testing. This suggests that the adhesive layer provides additional bonding force and helps to withstand the tension forces during fatigue experiments, resulting in a longer lifetime for the joint. The adhesive layer appears to play a significant role in improving the fatigue properties of the joint, despite its lack of impact on other performance measures.

Chapter 6: Related Publications and Conferences

1. **Ding Q**, Das H, Upadhyay P, Sousa BC, Karayagiz K, Powell A, Mishra B. Microstructural, Corrosion, and Mechanical Characterization of Friction Stir Welded Al 6022-to-ZEK100 Mg Joints. Corrosion and Materials Degradation. 2023; 4(1):142-157.
2. TMS 2023: Investigation of Corrosion Mechanisms and Fatigue Property of Friction-Stir Welded Joints between 6022 Al and ZEK100 Mg Alloy.
3. TMS 2022: Corrosion and mechanical characterization of friction-stir welded joints between aluminum and magnesium alloys.
4. TMS 2021: Cyclic corrosion testing of Al-Mg friction stir welding bi-metallic joints.
5. TMS 2020: Cyclic corrosion testing of bi-metallic joints between Al and Mg alloys.

References

[1] W. Zhang, J. Xu, Advanced lightweight materials for Automobiles: A review, Materials & Design, DOI (2022) 110994.

[2] M. Lee, S.-H. Jung, Trends of advanced multi-material technology for light materials based on aluminum, Journal of Welding and Joining, 34 (2016) 19-25.

[3] T. Wang, D.R. Tamayo, X. Jiang, P. Kitsopoulos, P. Upadhyay, Effect of interfacial characteristics on magnesium to steel joint obtained using FAST, Materials & Design, 192 (2020) 108697.

[4] S.K. Raval, K. Judal, Recent advances in dissimilar friction stir welding of aluminum to magnesium alloys, Materials Today: Proceedings, 22 (2020) 2665-2675.

[5] H. Rao, B. Ghaffari, W. Yuan, J. Jordon, H. Badarinarayan, Effect of process parameters on microstructure and mechanical behaviors of friction stir linear welded aluminum to magnesium, Materials Science and Engineering: A, 651 (2016) 27-36.

[6] M.A. Karim, Y.-D. Park, A review on welding of dissimilar metals in car body manufacturing, Journal of Welding and Joining, 38 (2020) 8-23.

[7] R.S. Mishra, H. Sidhar, Friction stir welding of 2xxx aluminum alloys including Al-Li alloys, Butterworth-Heinemann2016.

[8] A. Arici, T. Sinmazçelýk, Effects of double passes of the tool on friction stir welding of polyethylene, Journal of materials science, 40 (2005) 3313-3316.

[9] Y.S. Sato, H. Kokawa, M. Enomoto, S. Jogan, Microstructural evolution of 6063 aluminum during friction-stir welding, Metallurgical and Materials Transactions A, 30 (1999) 2429-2437.

[10] C. Dawes, An introduction to friction stir welding and its development, DOI (1995).

[11] A. Heidarzadeh, S. Mironov, R. Kaibyshev, G. Çam, A. Simar, A. Gerlich, F. Khodabakhshi, A. Mostafaei, D.P. Field, J.D. Robson, Friction stir welding/processing of metals and alloys: a comprehensive review on microstructural evolution, Progress in Materials Science, 117 (2021) 100752.

[12] R.S. Mishra, Z. Ma, Friction stir welding and processing, Materials science and engineering: R: reports, 50 (2005) 1-78.

[13] A. Luo, T. Lee, J. Carter, Self-pierce riveting of magnesium to aluminum alloys, SAE International Journal of Materials and Manufacturing, 4 (2011) 158-165.
[14] J. Yang, Z. Yu, Y. Li, H. Zhang, N. Zhou, Laser welding/brazing of 5182 aluminium alloy to ZEK100 magnesium alloy using a nickel interlayer, Science and Technology of Welding and Joining, 23 (2018) 543-550.
[15] Z. Shen, X. Liu, D. Li, Y. Ding, W. Hou, H. Chen, W. Li, A.P. Gerlich, Interfacial Bonding and Mechanical Properties of Al/Mg Dissimilar Refill Friction Stir Spot Welds Using a Grooved Tool, Crystals, 11 (2021) 429.
[16] H. Das, P. Upadhyay, S.S. Kulkarni, W. Choi, Dissimilar joining of ZEK100 and AA6022 for automotive application, Friction Stir Welding and Processing XI, Springer International Publishing, 2021, pp. 115-124.
[17] J. Mohammadi, Y. Behnamian, A. Mostafaei, A. Gerlich, Tool geometry, rotation and travel speeds effects on the properties of dissimilar magnesium/aluminum friction stir welded lap joints, Materials & Design, 75 (2015) 95-112.
[18] V. Firouzdor, S. Kou, Al-to-Mg friction stir welding: effect of material position, travel speed, and rotation speed, Metallurgical and Materials Transactions A, 41 (2010) 2914-2935.
[19] A. Kostka, R. Coelho, J. Dos Santos, A. Pyzalla, Microstructure of friction stir welding of aluminium alloy to magnesium alloy, Scripta Materialia, 60 (2009) 953-956.
[20] J. Yan, Z. Xu, Z. Li, L. Li, S. Yang, Microstructure characteristics and performance of dissimilar welds between magnesium alloy and aluminum formed by friction stirring, Scripta Materialia, 53 (2005) 585-589.
[21] C. Liu, D. Chen, S. Bhole, X. Cao, M. Jahazi, Polishing-assisted galvanic corrosion in the dissimilar friction stir welded joint of AZ31 magnesium alloy to 2024 aluminum alloy, Materials Characterization, 60 (2009) 370-376.
[22] M.A. Mofid, E. Loryaei, Investigating microstructural evolution at the interface of friction stir weld and diffusion bond of Al and Mg alloys, Journal of Materials Research and Technology, 8 (2019) 3872-3877.
[23] P. Dong, D. Sun, B. Wang, Y. Zhang, H. Li, Microstructure, microhardness and corrosion susceptibility of friction stir welded AlMgSiCu alloy, Materials & Design (1980-2015), 54 (2014) 760-765.

[24] R. Nandan, T. DebRoy, H. Bhadeshia, Recent advances in friction-stir welding–process, weldment structure and properties, Progress in materials science, 53 (2008) 980-1023.
[25] Ø. Grong, D. Grong, Metallurgical modelling of welding, Institute of materials London1997.
[26] R. Beygi, I. Galvão, A. Akhavan-Safar, H. Pouraliakbar, V. Fallah, L.F. da Silva, Effect of Alloying Elements on Intermetallic Formation during Friction Stir Welding of Dissimilar Metals: A Critical Review on Aluminum/Steel, Metals, 13 (2023) 768.
[27] M. Montemor, Corrosion issues in joining lightweight materials: A review of the latest achievements, Physical Sciences Reviews, 1 (2016).
[28] Y.-J. Lin, C.-S. Lin, Galvanic corrosion behavior of friction stir welded AZ31B magnesium alloy and 6N01 aluminum alloy dissimilar joints, Corrosion Science, 180 (2021) 109203.
[29] J. Mohammadi, Y. Behnamian, A. Mostafaei, H. Izadi, T. Saeid, A. Kokabi, A. Gerlich, Friction stir welding joint of dissimilar materials between AZ31B magnesium and 6061 aluminum alloys: Microstructure studies and mechanical characterizations, Materials Characterization, 101 (2015) 189-207.
[30] H. Li, J. Gao, Q. Li, Fatigue of friction stir welded aluminum alloy joints: a review, Applied Sciences, 8 (2018) 2626.
[31] L. Wang, L. Hui, S. Zhou, L. Xu, B. He, Effect of corrosive environment on fatigue property and crack propagation behavior of Al 2024 friction stir weld, Transactions of Nonferrous Metals Society of China, 26 (2016) 2830-2837.
[32] M. Czechowski, Low-cycle fatigue of friction stir welded Al–Mg alloys, Journal of Materials Processing Technology, 164 (2005) 1001-1006.
[33] X. Meng, Z. Lin, F. Wang, Investigation on corrosion fatigue crack growth rate in 7075 aluminum alloy, Materials & Design, 51 (2013) 683-687.
[34] F. Mokdad, D. Chen, Strain-controlled low cycle fatigue properties of a rare-earth containing ZEK100 magnesium alloy, Materials & Design, 67 (2015) 436-447.
[35] S. Tan, F. Zheng, J. Chen, J. Han, Y. Wu, L. Peng, Effects of process parameters on microstructure and mechanical properties of friction stir lap linear welded 6061 aluminum alloy to NZ30K magnesium alloy, Journal of Magnesium and Alloys, 5 (2017) 56-63.
[36] A. Albannai, Review the common defects in friction stir welding, Int. J. Sci. Technol. Res, 9 (2020) 318-329.

[37] Y.S. Sato, S.H.C. Park, M. Michiuchi, H. Kokawa, Constitutional liquation during dissimilar friction stir welding of Al and Mg alloys, Scripta Materialia, 50 (2004) 1233-1236.
[38] A. Somasekharan, L. Murr, Microstructures in friction-stir welded dissimilar magnesium alloys and magnesium alloys to 6061-T6 aluminum alloy, Materials Characterization, 52 (2004) 49-64.
[39] S.-I. Pyun, S.-M. Moon, Corrosion mechanism of pure aluminium in aqueous alkaline solution, Journal of Solid State Electrochemistry, 4 (2000) 267-272.
[40] S. Choudhary, A. Garg, K. Mondal, Relation Between Open Circuit Potential and Polarization Resistance with Rust and Corrosion Monitoring of Mild Steel, Journal of Materials Engineering and Performance, 25 (2016) 2969-2976.
[41] K. Bonhoeffer, W. Jena, The electrolytic and chemical passivation and activation of iron, Journal of Elektrochem, 59 (1951) 151.
[42] M. Stern, A.L. Geary, Electrochemical polarization: I. A theoretical analysis of the shape of polarization curves, Journal of the electrochemical society, 104 (1957) 56.
[43] F. Mansfeld, The polarization resistance technique for measuring corrosion currents, Advances in Corrosion Science and Technology: Volume 6, DOI (1976) 163-262.
[44] G. Song, Recent progress in corrosion and protection of magnesium alloys, Advanced engineering materials, 7 (2005) 563-586.
[45] S.S. Jamali, S.E. Moulton, D.E. Tallman, M. Forsyth, J. Weber, G.G. Wallace, Evaluating the corrosion behaviour of Magnesium alloy in simulated biological fluid by using SECM to detect hydrogen evolution, Electrochimica Acta, 152 (2015) 294-301.
[46] X. Zhang, Z.H. Jiang, Z.P. Yao, Y. Song, Z.D. Wu, Effects of scan rate on the potentiodynamic polarization curve obtained to determine the Tafel slopes and corrosion current density, Corrosion science, 51 (2009) 581-587.
[47] F. Mansfeld, Tafel slopes and corrosion rates obtained in the pre-Tafel region of polarization curves, Corrosion Science, 47 (2005) 3178-3186.
[48] S. Esmailzadeh, M. Aliofkhazraei, H. Sarlak, Interpretation of Cyclic Potentiodynamic Polarization Test Results for Study of Corrosion Behavior of Metals: A Review, Protection of Metals and Physical Chemistry of Surfaces, 54 (2018) 976-989.

[49] J.N. Murray, Electrochemical test methods for evaluating organic coatings on metals: an update. Part III: Multiple test parameter measurements, Progress in Organic coatings, 31 (1997) 375-391.
[50] H.H. Hernández, A.M.R. Reynoso, J.C.T. González, C.O.G. Morán, J.G.M. Hernández, A.M. Ruiz, J.M. Hernández, R.O. Cruz, Electrochemical impedance spectroscopy (EIS): A review study of basic aspects of the corrosion mechanism applied to steels, Electrochemical Impedance Spectroscopy, DOI (2020) 137-144.
[51] H. Cesiulis, N. Tsyntsaru, A. Ramanavicius, G. Ragoisha, The study of thin films by electrochemical impedance spectroscopy, Nanostructures and thin films for multifunctional applications: technology, properties and devices, DOI (2016) 3-42.
[52] X. Liu, J. Xiong, Y. Lv, Y. Zuo, Study on corrosion electrochemical behavior of several different coating systems by EIS, Progress in Organic Coatings, 64 (2009) 497-503.
[53] M. Jamesh, S. Kumar, T.S. Narayanan, Corrosion behavior of commercially pure Mg and ZM21 Mg alloy in Ringer's solution–Long term evaluation by EIS, Corrosion Science, 53 (2011) 645-654.
[54] E. Cano, D. Lafuente, D.M. Bastidas, Use of EIS for the evaluation of the protective properties of coatings for metallic cultural heritage: a review, Journal of Solid State Electrochemistry, 14 (2010) 381-391.
[55] F. Mansfeld, Use of electrochemical impedance spectroscopy for the study of corrosion protection by polymer coatings, Journal of applied electrochemistry, 25 (1995) 187-202.
[56] M. Esmaily, J. Svensson, S. Fajardo, N. Birbilis, G. Frankel, S. Virtanen, R. Arrabal, S. Thomas, L. Johansson, Fundamentals and advances in magnesium alloy corrosion, Progress in Materials Science, 89 (2017) 92-193.
[57] L. Xu, E. Zhang, D. Yin, S. Zeng, K. Yang, In vitro corrosion behaviour of Mg alloys in a phosphate buffered solution for bone implant application, Journal of Materials Science: Materials in Medicine, 19 (2008) 1017-1025.
[58] F.W. Lutze, K.A. Smith, R. Mason, D. Nymberg, L.S. Thompson, C. Meade, L. McQuiston, R. Singleton, C. Handsy, Update on the Developments of the SAE J2334 Laboratory Cyclic Corrosion Test, SAE transactions, DOI (2003) 1209-1214.
[59] A. G71, Standard guide for conducting and evaluating galvanic corrosion tests in electrolytes, DOI (2009).

[60] D.A. Jones, Denny-a-Jones-Principles-and-Prevention-of-Corrosion, Environments, 334 357.
[61] J. Hay, Instrumented indentation apparatus having indenter punch with flat end surface and instrumented indentation method using the same, Google Patents, 2019.
[62] Z.-M. Su, P.-C. Lin, W.-J. Lai, J. Pan, G.-J. Cheng, H.-W. Yen, Fatigue analyses and life predictions of laser-welded lap-shear specimens made of low carbon and high strength low alloy steels, International Journal of Fatigue, 140 (2020) 105849.
[63] S. Feliu Jr, Electrochemical impedance spectroscopy for the measurement of the corrosion rate of magnesium alloys: Brief review and challenges, Metals, 10 (2020) 775.
[64] G.L. Song, A. Atrens, Corrosion mechanisms of magnesium alloys, Advanced engineering materials, 1 (1999) 11-33.
[65] R.-c. Zeng, J. Zhang, W.-j. Huang, W. Dietzel, K. Kainer, C. Blawert, K. Wei, Review of studies on corrosion of magnesium alloys, Transactions of Nonferrous Metals Society of China, 16 (2006) s763-s771.
[66] J.M. Kolotyrkin, Effects of anions on the dissolution kinetics of metals, Journal of the Electrochemical Society, 108 (1961) 209.
[67] R. Tunold, H. Holtan, M.-B. Berge, A. Lasson, R. Steen-Hansen, The corrosion of magnesium in aqueous solution containing chloride ions, Corrosion Science, 17 (1977) 353-365.
[68] Q. Guan, J. Sun, W.Y. Wang, J. Gao, C. Zou, J. Wang, B. Tang, H. Kou, H. Wang, J. Hou, Pitting corrosion of natural aged Al–Mg–Si extrusion profile, Materials, 12 (2019) 1081.
[69] C. Vargel, Corrosion of aluminium, Elsevier2020.
[70] A. Bastos, M. Quevedo, O. Karavai, M. Ferreira, On the application of the scanning vibrating electrode technique (SVET) to corrosion research, Journal of The Electrochemical Society, 164 (2017) C973.
[71] Z. Cano, J. McDermid, J. Kish, Cathodic activity of corrosion filaments formed on Mg alloy AM30, Journal of The Electrochemical Society, 162 (2015) C732.
[72] R.K. Jayaraj, S. Malarvizhi, V. Balasubramanian, Electrochemical corrosion behaviour of stir zone of friction stir welded dissimilar joints of AA6061 aluminium–AZ31B magnesium alloys, Transactions of Nonferrous Metals Society of China, 27 (2017) 2181-2192.
[73] B. Ratna Sunil, G. Pradeep Kumar Reddy, Corrosion behavior of friction stir welded AZ31B Mg alloy-Al6063 alloy joint, Cogent Engineering, 3 (2016) 1145565.

[74] K. Ralston, N. Birbilis, C. Davies, Revealing the relationship between grain size and corrosion rate of metals, Scripta Materialia, 63 (2010) 1201-1204.